

ACOUSTIC WAVE PROPAGATION IN TTF-TCNQ

by

J. THOMAS TIEDJE

B.A.Sc., University of Toronto, 1973
M.Sc., University of British Columbia, 1975

A THESIS SUBMITTED IN PARTIAL FULFILLMENT
OF THE REQUIREMENTS FOR THE DEGREE OF
DOCTOR OF PHILOSOPHY

THE FACULTY OF GRADUATE STUDIES
in the Department
of
Physics

We accept this thesis as conforming
to the required standard

THE UNIVERSITY OF BRITISH COLUMBIA
July, 1977

© J. Thomas Tiedje

In presenting this thesis in partial fulfilment of the requirements for an advanced degree at the University of British Columbia, I agree that the Library shall make it freely available for reference and study.

I further agree that permission for extensive copying of this thesis for scholarly purposes may be granted by the Head of my Department or by his representatives. It is understood that copying or publication of this thesis for financial gain shall not be allowed without my written permission.

Department of Physics

The University of British Columbia
2075 Wesbrook Place
Vancouver, Canada
V6T 1W5

Date Sept. 7/77

ABSTRACT

Detailed measurements have been made of the temperature dependence of the velocity of three different modes of sound propagation in TTF-TCNQ crystals, in the range 7-300K. Values for the a and b axis Young's moduli and the shear modulus c_{66} are inferred from the sound velocities. TTF-TCNQ is found to be stiffer perpendicular to the conducting direction than parallel to it. The elastic anisotropy is typical of crystalline solids even though the anisotropy of the electrical conductivity is unusually large. A small (1.5%) increase in the velocity of extensional waves below the metal-insulator transition is interpreted as being due to the disappearance of the conduction electrons. A quantitative theory of the low temperature velocity anomaly leads to an accurate estimate of the $q \rightarrow 0$ electron-phonon coupling constant.

The sound velocity measurements were made using an acoustic resonance technique. Resonant modes of vibration of single crystals of TTF-TCNQ were excited electrostatically and detected capacitively using a UHF carrier signal. The detection scheme is shown to be more sensitive than conventional d.c. biased capacitive pickups.

A theoretical study of the electronic contribution to the attenuation of sound in one and two dimensional metals and semiconductors is presented. The attenuation in one dimensional metals is shown to be anomalously small. In both one and two dimensional metals, in the quantum limit the attenuation depends strongly on the direction of propagation of the wave. A transport equation solution to the problem

of calculating the amplification of sound waves in a solid in the presence of a d.c. electric field is described. The treatment is much less complex than any that is currently available.

TABLE OF CONTENTS

	Page
ABSTRACT	ii
TABLE OF CONTENTS	iv
LIST OF FIGURES	vii
LIST OF TABLES	x
ACKNOWLEDGEMENTS	xi
INTRODUCTION	
1. The Organic Conductor TTF-TCNQ	1
2. Organization of the Thesis	7
PART A: Electronic Contribution to Attenuation and Amplification of Acoustic Waves	9
I ATTENUATION IN METALS	10
1.1 Introduction	10
1.2 Transport Equation Approach to Ultrasonic Attenuation	12
1.3 The Quantum Limit	22
1.4 Metals	27
(i) Three Dimensional Metals	27
(ii) Two Dimensional Metals	31
(iii) One Dimensional Metals	36
1.5 Anisotropy of Attenuation	44
(i) One Dimensional Metals	45
(ii) Two Dimensional Metals	50
1.6 Summary	55
II ATTENUATION IN SEMICONDUCTORS	57
2.1 Quantum Limit	57
2.2 Transport Equation Approach	59
2.3 Metal Semiconductor Transition	64
III AMPLIFICATION	71
3.1 Introduction	71
3.2 Transport Equation	72
3.3 Energy Transfer	79
3.4 Conclusion	85

	Page
PART B: Measurements on TTF-TCNQ	87
I EXPERIMENTAL METHOD	88
1.1 Capacitive Measurement Technique	88
(i) Electronics	90
(ii) Sample Support	100
1.2 Sensitivity of the Measurement Technique	104
(i) Minimum Detectable Length Change	104
(ii) A.C. Method	106
(iii) D.C. Method	109
II THE MODES OF VIBRATION OF TTF-TCNQ CRYSTALS..	114
2.1 Low Frequency Modes of an Elongated Plate	114
(i) Flexural Modes	115
(ii) Torsional Modes	119
(iii) Comments on a Short Plate	121
(iv) Elongational Modes	123
(v) Crystallographic Symmetry	125
2.2 Interpretation of Experimental Mode	
Spectrum	130
(i) Vibrating Reed Support	132
(ii) Central Pin Support	139
(iii) Mode Coupling	143
(iv) Support Modes	145
2.3 Vibration Damping	145
(i) Q Measurement	145
(ii) Thermoelastic Damping	147
(iii) Elongational Modes	152
(iv) Effect of Air on Resonance Fre-	
quency and Q	155
III INTERPRETATION OF TEMPERATURE DEPENDENCE OF	
SOUND VELOCITY	162
3.1 Overall Temperature Dependence	162
3.2 Low Temperature Anomaly	178
(i) Quantum Limit	180
(ii) Thermodynamic Limit	191
(iii) Comment on Acoustic Absorption	199
SUMMARY	204
1. The Main Results of this Work	204
2. Suggestions for Further Work	207

APPENDIX	Page
1. Diode Temperature Sensor Calibration	210
2. Circuit Diagrams	211
(i) Diode Detector Circuit	211
(ii) MOSFET Preamplifier	211
(iii) Phase Shifter	212
(iv) Lorentzian Generator	214
(v) Signal Averager Input Amplifier	214
3. Thermal Expansion Correction	215
BIBLIOGRAPHY.....	216

LIST OF FIGURES

Figure	Page
1. TTF and TCNQ Molecules	2
2. TTF-TCNQ Crystal Structure	3
3. TTF-TCNQ b Axis Conductivity	5
4. Temperature Dependence of Electronic Energy Gap	6
5. Crossection of the Fermi Sphere Showing the Inter- action Surface	25
6. Acoustic Attenuation as a Function of $q\ell$ for 2 and 3D Metals	35
7. Fermi Surface and Interaction Surface in a 1D Metal..	37
8. Angular Dependence of Attenuation in a 1D Metal in the Quantum Limit	46
9. Angular Dependence of Attenuation in 1D Metal for $\Lambda = 8$	49
10. Angular Dependence of Attenuation in a 2D Metal in the Quantum Limit	52
11. Angular Dependence of Attenuation in a 2D Metal for $\Lambda = 8$	53
12. Interaction Surfaces - Metallic Band	66
13. Interaction Surfaces - Semiconductor Band	67
14. Attenuation Near a Metal-Semiconductor Transition in a 1D Metal in the Quantum Limit	68
15. Drive and Detector Circuit	89
16. Drive and Bridge Detector Circuit	89
17. Block Diagram of Electronic Equipment	93
18. Sample Mounting Configurations	95
19. Photographs of Mounted Samples	96
20. Cut-Away View of Sample Box	97

Figure	Page
21. Photograph of the Outside of the Sample Holder	98
22. Photograph of the Inside of the Sample Holder	99
23. Shielded Electrode	101
24. Special Notched Electrode	101
25. Cryostat for Low Temperature Measurements	102
26. Capacitive Vibration Detector - A.C. Method	106
27. Capacitive Vibration Detector - D.C. Method	109
28. Noise Equivalent Circuit	110
29. Contour Map of Sensitivity of D.C. Method	112
30. Flexural Mode Shapes	117
31. Modes of a Square Cantilever Plate	122
32. Modes of a Rectangular Free Plate	122
33. Arrangement of TTF and TCNQ Molecules in the a c Plane	124
34. Experimental Flexural Mode Spectrum	131
35. Low Frequency Flexural and Torsional Mode Dispersion Diagram	133
36. Effect of D.C. Bias Voltage on Flexural Resonance Frequency	135
37. Longitudinal Mode Dispersion Diagram	138
38. Flexural and Torsional Mode Crossing	142
39. Interference with F_{ac} Flexural Mode	144
40. Wiggles	147
41. Flexural Mode Damping	149
42. Longitudinal Mode Damping	151

Figure	Page
43. Sound Velocity and Attenuation Near the Metal-Semiconductor Transition	153
44. Air Entrained by a Flexural Mode	156
45. Air Entrained by a Torsional Mode	157
46. Temperature Dependence of b Axis Elongational and Torsional Mode Velocities	163
47. Temperature Dependence of b Axis Flexural Mode Velocity	164
48. Temperature Dependence of a Axis Flexural and Torsional Mode Velocities	165
49. Low Temperature Anomaly in the Young's Modulus Velocity	177
50. Excitation Spectrum for a Non-Interacting 1D Tight-Binding Band	179
51. Dyson's Equation	182
52. Electron Gas Polarization Diagram	183
53. Hartree Polarizability for a 1D Tight-Binding Band...	184
54. Acoustic Phonon Dispersion for Experimental Electron-Phonon Coupling Constant	187
55. Acoustic Phonon Dispersion for an Electron-Phonon Coupling Constant which gives $T_c = 54K$	188
56. Band Structure of TTF-TCNQ	192
57. Strain Dependence of the Density of Occupied States..	193
58. Low Temperature Longitudinal Mode Damping	201

LIST OF TABLES

Table		Page
I	TTF-TCNQ Material Parameters	47
II	Attenuation for 1, 2, 3D Metals in a D.C. Electric Field	81
III	Flexural Mode Parameters	116
IV	Flexural Mode Elastic Constants	128
V	Room Temperature Sound Velocities for TTF-TCNQ	141
VI	Effect of Air on Flexural and Torsional Mode Frequencies	158
VII	Young's Moduli for Various Materials	162
VIII	Grüneisen Constant for Various Materials	174
IX	Pressure Derivative of Bulk Modulus for Various Materials	176
X	Summary of the Experimental Results	206

ACKNOWLEDGEMENTS

I am grateful to my supervisor Rudi Haering for the considerable amount of time and effort he has spent helping me with this project. His physical intuition and common sense were invaluable, to say the least.

The capacitive measurement technique was suggested by Walter Hardy, and his help was essential in making it work. The quantum approach to the interpretation of the low temperature velocity anomaly was suggested by E. Tosatti. All aspects of the interpretation of the temperature dependence of the sound velocities were worked out in collaboration with Manfred Jericho. I benefited from many useful discussions with B. Bergersen and W. I. Friesen.

I would like to thank L. Weiler for supplying me with TTF-TCNQ samples and for explanations of various chemistry problems. The TTF-TCNQ crystals used in the experiment were synthesized and grown by Y. Hoyano.

It is a pleasure to thank Susan Haering for taking, developing and printing the photographs in this thesis.

Lore Hoffmann simplified the final production process with her efficient typing and thoughtful approach to the organization of the thesis.

I am grateful to the National Research Council for financial support in the form of a Science Scholarship.

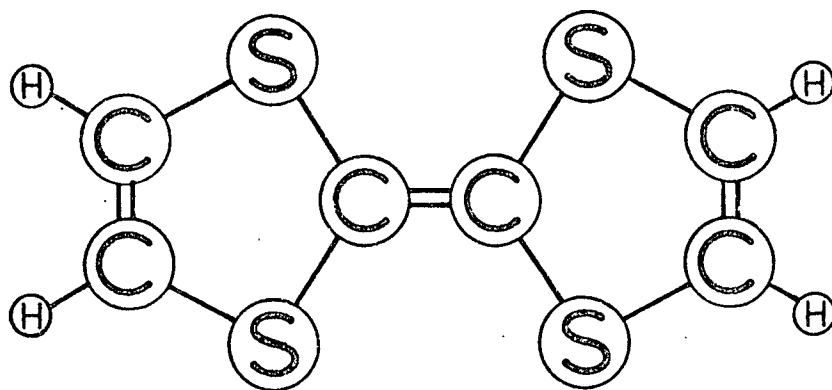
INTRODUCTION

1. The Organic Conductor TTF-TCNQ

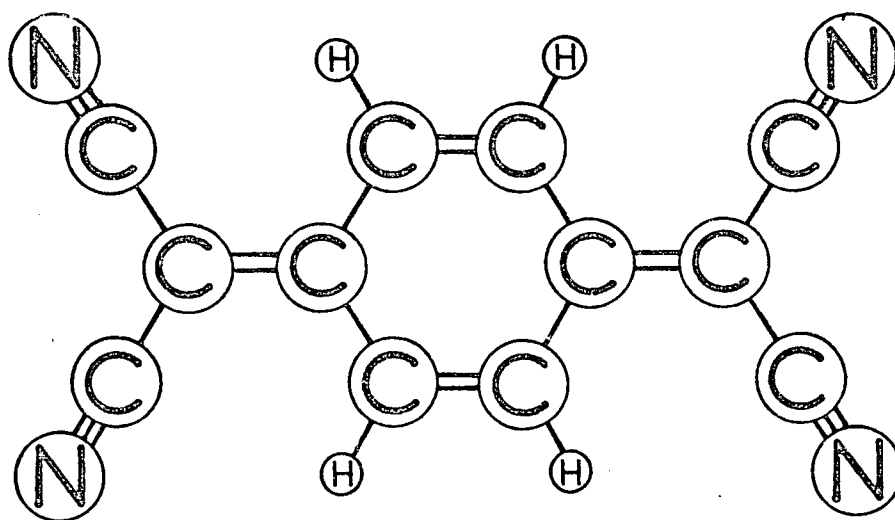
Tetrathiofulvalinium (TTF) tetracyanoquinodimethanide (TCNQ) is an electrically conducting organic solid composed of the TTF and TCNQ molecules shown in Fig. 1. The material has several unusual properties. First it is a better conductor than almost any other organic material known. In fact, at 60K its conductivity ($10^4 (\Omega\text{-cm})^{-1}$) is comparable with mercury at room temperature. The availability of good organic conductors opens up the possibility of making materials with desirable electronic properties by chemical modification of the constituent molecules. Potential applications include new or improved electronic devices and higher temperature superconductors.

A second unusual feature of TTF-TCNQ is that its conductivity is very anisotropic. The anisotropy arises from the nature of the crystal structure; as shown in Fig. 2, the large flat TTF and TCNQ molecules are arranged in segregated stacks. The molecular orbitals for neighbouring molecules on the same stack overlap much more strongly than the molecular orbitals for molecules on different stacks. The result is that electrons are able to move more freely along the chains than perpendicular to the chains. The corresponding anisotropy in the conductivity is large enough that the material may be regarded as a nearly one dimensional metal.

Theory predicts a number of unique properties for one dimensional conductors. One of these characteristics, namely the Peierls insta-



TTF



TCNQ

Fig. 1 - TTF and TCNQ Molecules



Fig. 2 - Photograph of a model of the TTF-TCNQ crystal structure

bility, causes a structural phase transition in which the one dimensional metal changes into a semiconductor. Electrical conductivity measurements reveal that TTF-TCNQ does undergo a phase transition of this type at low temperatures (see Fig. 3). X-ray and neutron scattering experiments seem to confirm that the phase transition is a Peierls transition. However, below the metal-semiconductor transition there is at least one and possibly as many as three (Djurek et al 1977) additional phase transitions. The two most prominent phase transitions, near 38K and 54K, are best illustrated by the temperature dependence of the electronic energy gap in the semiconducting phase as shown in Fig. 4 (Tiedje 1975). The phase transitions are reflected in sharp increases in the electronic energy gap 2Δ , as a function of temperature. The nature of these phase transitions is not well understood.

Most of the initial work on TTF-TCNQ was stimulated by the observation in a few samples of TTF-TCNQ of an anomalously high conductivity peak (Coleman et al 1973) just above the metal-insulator transition. The anomalous conductivity was interpreted at the time as due to superconducting fluctuations enhanced by the onset of the Peierls distortion. No one has succeeded in duplicating these measurements, although there have been many attempts. For reviews of recent work on TTF-TCNQ and related materials see Bulaevskii (1975), André et al (1976) and Keller (1977).

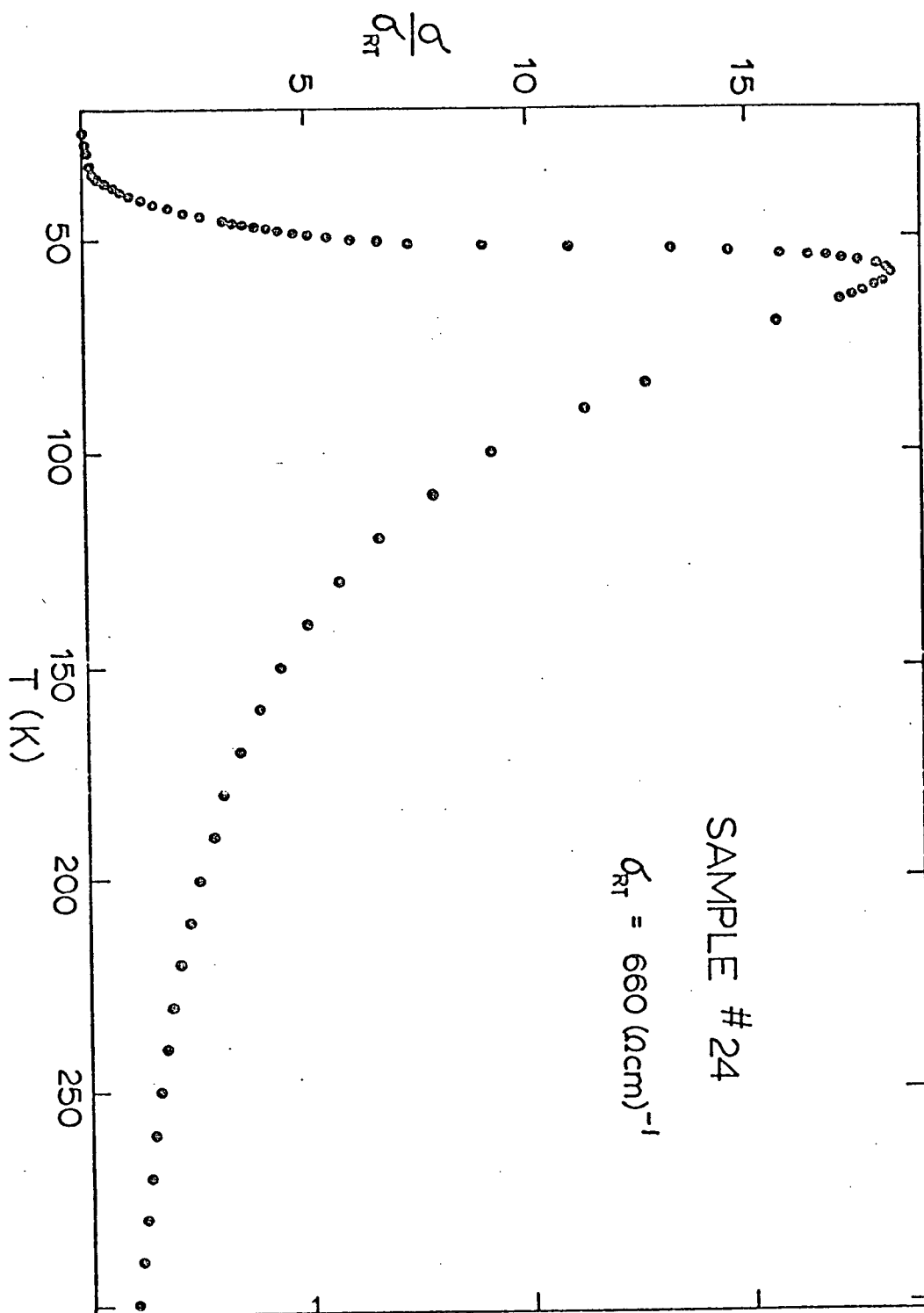


Fig. 3 - Temperature dependence of the TTF-TCNQ b axis conductivity. Sample #24 came from the same batch as many of the samples on which acoustic measurements were made.

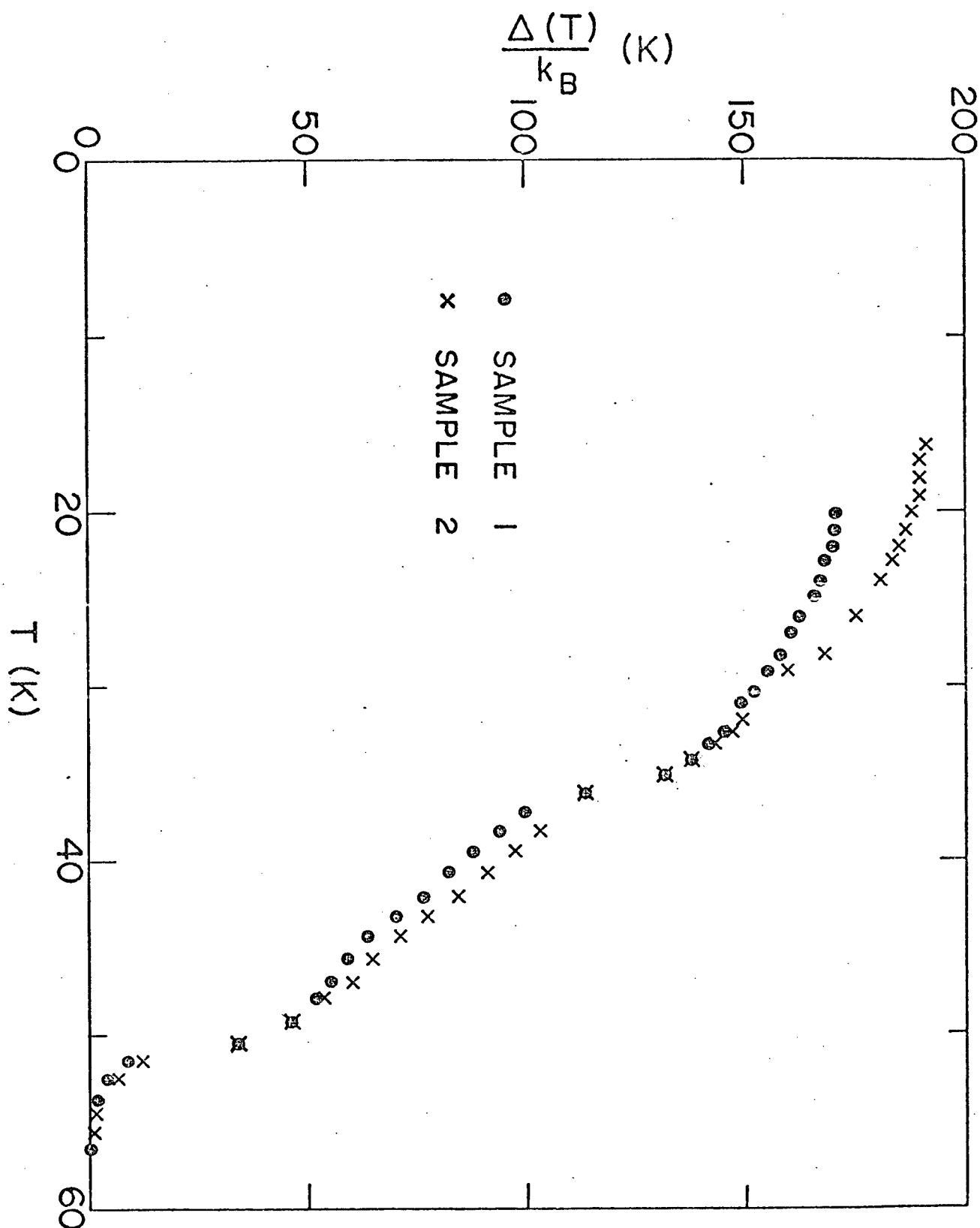


Fig. 4 - Temperature dependence of the electronic energy gap (2Δ) in the insulating phase of TTF-TCNQ. Notice the change in slope near 52K and 38K.

2. Organization of the Thesis

The remainder of this thesis is divided into two parts. In Part A we investigate the effect of the dimensionality of the electron gas on the electronic contribution to the attenuation of sound in metals and semiconductors. Both electromagnetic and deformation potential coupling between the electrons and the sound wave are considered. The dependence of the attenuation of high frequency acoustic waves on the direction of propagation of the wave is calculated for one and two dimensional metals. An improved transport theory of the amplification of sound in the presence of a d.c. electric field is also presented.

In Part B we discuss some experimental measurements on the propagation of sound in crystals of TTF-TCNQ. The large anisotropy in the electrical properties of TTF-TCNQ are illustrated by electrical conductivity measurements (Hardy et al 1976) dielectric constant measurements (Cohen et al 1976) and molecular orbital calculations (Berlinsky et al 1974). Similarly the temperature dependence of the lattice constants (Blessing and Coppens 1974) and the nature of the bonding in the crystal suggest that the lattice may be elastically highly anisotropic as well. In order to measure the anisotropy in the elastic properties and to help clarify the nature of the low temperature phase transitions detailed measurements have been made of the temperature dependence of the velocity and attenuation of sound in TTF-TCNQ.

Part B is divided into three chapters. In the first chapter the capacitive technique that was used to excite and detect acoustic resonances in single crystals of TTF-TCNQ is described in detail. An analysis of the sensitivity of capacitive displacement detectors is included. The second chapter explains how the vibration spectrum can be used to determine a number of different elastic constants for TTF-TCNQ. The principal damping mechanisms for samples vibrating in air and in a vacuum are discussed.

The final chapter contains an interpretation of the temperature dependence of the velocity of sound. A small low temperature anomaly in the velocity is interpreted as being due to an electronic contribution to the elastic moduli. A possible explanation for an increase in damping of some of the acoustic modes at low temperatures is proposed.

P A R T A

ELECTRONIC CONTRIBUTION TO ATTENUATION AND AMPLIFICATION OF
ACOUSTIC WAVES

CHAPTER I

A t t e n u a t i o n

1.1 Introduction

The electronic contribution to ultrasonic attenuation has been studied extensively in three dimensional metals (Pippard 1955, Cohen et al 1960, Rice and Sham 1970). The recent discovery of highly anisotropic quasi one and two dimensional metals has stimulated interest in the properties of electronic systems of reduced dimensionality (Gläser 1974, Wilson et al 1975). In this chapter we extend the theory of ultrasonic attenuation so that it applies to such systems. We present general expressions for the attenuation constant of longitudinal and transverse waves, and we obtain limiting expressions valid in the hydrodynamical and in the quantum mechanical limits. We show that the ultrasonic attenuation in one and two dimensional systems differs significantly from the attenuation in three dimensional structures. The difference is particularly significant in the case of one dimensional systems where energy and momentum selection rules are difficult to satisfy.

It is well known that the absorption of sound in metals depends on the relation between the mean free path of an electron at the Fermi surface, ℓ , and the wave length of the sound wave, $\lambda = \frac{2\pi}{q}$. In this chapter, the Boltzmann transport equation is used to calculate the attenuation as a function of frequency for arbitrary values of $q\ell$. Quantum mechanical perturbation theory is also used to derive the attenuation in the quantum limit.

Although other contributions to the attenuation will be present in real metals, only the electronic contribution will be considered here. With this limitation the ultrasonic attenuation problem is formulated for a three dimensional electron gas using the Boltzmann equation in the relaxation time approximation. The electrons are assumed to interact with the lattice through "collisions", self-consistent electromagnetic fields, and a scalar deformation potential. Then with the deformation potential interaction alone, the high frequency ($q\ell \gg 1$) limit is rederived using quantum mechanical perturbation theory. The two approaches mentioned above are then specialized to the three, two, and one dimensional electronic systems. In each case the attenuation is calculated explicitly for free electrons. In all cases the electrons are assumed to be contained in a three dimensional crystal lattice.

1.2 Transport Equation Approach to Ultrasonic Attenuation

The Boltzmann equation, in the relaxation time approximation, is given by (see e.g. Ziman 1972)

$$[1] \quad \frac{\partial f}{\partial t} + \underline{v} \cdot \underline{\nabla}_r f - e \underline{E} \cdot \underline{\nabla}_k f = -\left(\frac{f - \bar{f}}{\tau}\right)$$

where \underline{E} is the self-consistent electric field generated by the sound wave, and f is the electron distribution function. Deformation potential coupling is included at a later stage. The electrons tend to relax towards the local equilibrium distribution function \bar{f} , through scattering. Following Holstein (1959) we assume that the electrons relax to an equilibrium distribution function centered at the local lattice velocity. Also, since the scattering processes are local, the electron density is not affected. For this reason the local equilibrium chemical potential must be determined self-consistently from the as yet unknown local electron density. The velocity of an electron in an arbitrary band structure is, $\underline{v} = \frac{1}{\hbar} \underline{\nabla}_k \epsilon(k)$. Hence the energy of an electron in a frame of reference moving with the local lattice velocity \underline{u} is given by

$$\epsilon'(k) = \epsilon(k) - \hbar \underline{k} \cdot \underline{u}$$

Adding the term $\hbar \underline{k} \cdot \underline{u}$ to the electron energy corresponds to tilting the band structure in \underline{k} space. To first order this corresponds to a Fermi surface shifted in \underline{k} space by $\frac{m\underline{u}}{\hbar}$. Thus, the local equilibrium distribution function is

$$\bar{f}(\underline{k}, \underline{x}, t) = f_0(\epsilon'(\underline{k}); \mu(\underline{x}, t)) \approx f_0 - \frac{\partial f_0}{\partial \epsilon} \left(\hbar \underline{k} \cdot \underline{u} + \frac{\partial \mu}{\partial n} n_1 \right)$$

where $\mu(\underline{x}, t)$ is the self-consistent chemical potential mentioned above, f_0 is the equilibrium electron distribution in the absence of a sound wave, and n_1 is the oscillating component of the electron number density.

The Boltzmann equation may now be solved to first order by linearizing. Let $f = f_0 + f_1$ where $f_1 \propto e^{i(qx - \omega t)}$ is the oscillating component of the distribution function that is induced by the sound wave. Equation [1] can now be written

$$\begin{aligned} -i\omega f_1 + \frac{1}{\hbar} \nabla_{\underline{k}} \epsilon(\underline{k}) \cdot \underline{q} f_1 &= e \frac{\underline{E}}{\hbar} \cdot \nabla_{\underline{k}} \epsilon(\underline{k}) \frac{\partial f_0}{\partial \epsilon} \\ &= -\frac{f_1}{\tau} - \frac{1}{\tau} \frac{\partial f_0}{\partial \epsilon} \left\{ \hbar \underline{k} \cdot \underline{u} + \frac{\partial \mu}{\partial n} n_1 \right\} \end{aligned}$$

This solution to first order in E , n_1 , u , and f_1 , all of which are proportional to the amplitude of the sound wave, is

$$[2] \quad f_1 = \frac{\tau e \underline{v} \cdot \underline{E} - \hbar \underline{k} \cdot \underline{u} - \frac{\partial \mu}{\partial n} n_1}{1 - i\omega\tau + i \underline{q} \cdot \underline{v}\tau} \left(- \frac{\partial f_0}{\partial \epsilon} \right)$$

The electronic current density is defined by

$$[3] \quad \underline{J}_e = - \frac{2e}{(2\pi)^3} \int d^3k \quad \underline{v} f_1$$

$$= \underline{g} \cdot \underline{E} - \underline{\Sigma} \cdot \frac{m \underline{u}}{e\tau} - n_1 e S \underline{R}$$

where $S = \frac{\omega}{q}$ is the phase velocity of the sound wave, and

$$[4a] \quad \underline{g} = \frac{2e^2\tau}{(2\pi)^3} \int d^3k \quad \frac{\underline{v} \underline{v}}{1 - i\omega\tau + i \underline{q} \cdot \underline{v}\tau} \left(- \frac{\partial f_0}{\partial \epsilon} \right)$$

$$[4b] \quad \underline{\Sigma} = \frac{2e^2\tau}{(2\pi)^3} \frac{\hbar}{m} \int d^3k \quad \frac{\underline{v} \underline{k}}{1 - i\omega\tau + i \underline{q} \cdot \underline{v}\tau} \left(- \frac{\partial f_0}{\partial \epsilon} \right)$$

$$[4c] \quad \underline{R} = \frac{\partial \mu}{\partial n} \frac{1}{S} \frac{2}{(2\pi)^3} \int d^3k \quad \frac{\underline{v}}{1 - i\omega\tau + i \underline{q} \cdot \underline{v}\tau} \left(- \frac{\partial f_0}{\partial \epsilon} \right)$$

The total current associated with the sound wave consists of the sum of the ion current and the electronic current which is induced

by the self-consistent electric field. The total current density is

$$\underline{J} = \underline{J}_e + n e \underline{u}.$$

If we restrict our attention to monovalent metals, the electron number density n will equal the ion number density. The continuity equation for electrons is

$$\omega n_1 e + \underline{q} \cdot \underline{J}_e = 0$$

or

$$[5] \quad J_{e\parallel} = -n_1 e S$$

where $J_{e\parallel}$ is the component of \underline{J}_e parallel to \underline{q} . The self-consistent electric field is determined from the total current density by the Maxwell equations (Kittel 1963). The result is

$$[6a] \quad E_{\parallel} = -\frac{4\pi i}{\omega} \left(J_{e\parallel} + n e u_{\parallel} \right)$$

and

$$[6b] \quad E_{\perp} = \frac{4\pi i}{\omega} \frac{\left(\frac{S}{c}\right)^2}{1 - \left(\frac{S}{c}\right)^2} \left(J_{e\perp} + n e u_{\perp} \right)$$

$$\approx \frac{4\pi i}{\omega} \left(\frac{S}{c}\right)^2 \left(J_{e\perp} + n e u_{\perp} \right).$$

The next step is to obtain expressions for the self-consistent electric field and current in terms of the lattice velocity. The problem can be simplified by assuming that the sound wavevector \underline{q} is in the direction of a principal axis of the electron constant energy surfaces. In this case the conductivity tensors are all diagonal, and the components can be treated separately.

In the case of longitudinal waves ($\underline{q} \parallel \underline{u}$), [5] can be used to eliminate n_1 from [3] to give

$$[7] \quad J_{ex} = \sigma'_{xx} E_x - \Sigma'_{xx} \frac{m u_x}{e \tau}$$

where $\sigma'_{xx} = \frac{\sigma_{xx}}{1 - R_x}$, $\Sigma'_{xx} = \frac{\Sigma_{xx}}{1 - R_x}$, and the wavevector \underline{q} is in the x direction. For longitudinal waves, only the x components of \underline{J}_e , \underline{E} and \underline{u} are non-zero. Now if [6a] is substituted for E_x , then

$$[8] \quad J_{ex} = -n e u_x \left\{ \frac{\frac{\Sigma'_{xx}}{\sigma_0} + \frac{4\pi i \sigma'_{xx}}{\omega}}{1 + \frac{4\pi i \sigma'_{xx}}{\omega}} \right\}$$

where $\sigma_0 = \frac{n e^2 \tau}{m}$. Notice that $J_{ex} = -n e u_x$ when $\omega \ll \sigma'_{xx} \sim \Sigma'_{xx}$.

In this (perfect screening) limit the ion current is exactly matched by the electron current. An expression for E_x is obtained by sub-

stituting [8] into [7]:

$$[9] \quad E_x = - \frac{n e u_x}{\sigma'_{xx}} \left\{ \frac{\frac{\Sigma'_{xx}}{\sigma_o} + \frac{4\pi i \sigma'_{xx}}{\omega}}{1 + \frac{4\pi i \sigma'_{xx}}{\omega}} - \frac{\Sigma'_{xx}}{\sigma_o} \right\}$$

In the transverse wave case ($\underline{q} \perp \underline{u}$), there is no electron density oscillation hence.

$$[10] \quad J_{ey} = \sigma_{yy} E_y - \Sigma_{yy} \frac{m u_y}{e \tau}$$

where \underline{q} is in the x-direction, and the lattice wave is polarized in the y direction. Substitute [6b] into [10] then

$$J_{ey} = - n e u_y \left[\frac{\frac{\Sigma_{yy}}{\sigma_o} - \frac{4\pi i}{\omega} \left(\frac{S}{c}\right)^2 \sigma_{yy}}{1 - \frac{4\pi i}{\omega} \left(\frac{S}{c}\right)^2 \sigma_{yy}} \right]$$

and

$$E_y = - \frac{n e u}{\sigma_{yy}} \left\{ \frac{\frac{\Sigma_{yy}}{\sigma_o} - \frac{4\pi i}{\omega} \left(\frac{S}{c}\right)^2 \sigma_{yy}}{1 - \frac{4\pi i}{\omega} \left(\frac{S}{c}\right)^2 \sigma_{yy}} - \frac{\Sigma_{yy}}{\sigma_o} \right\}.$$

The screening of the transverse waves is less efficient than the screening of the longitudinal wave because the charge carriers inter-

act through magnetic forces rather than through the stronger electric forces. The factors of $\left(\frac{S}{c}\right)^2$ reflect this difference. The expressions may be written more compactly by observing that the contribution of the conduction electrons to the dielectric constant of a metal with conductivity $\underline{\sigma}$ is

$$\underline{\epsilon}(\underline{q}, \omega) = \underline{1} + \frac{4\pi i}{\omega} \underline{\sigma}(\underline{q}, \omega)$$

Thus, for longitudinal waves

$$[11] \quad E_x = \frac{n e u_x}{\epsilon'_{xx}} \frac{4\pi i}{\omega} \left[\frac{\Sigma'_{xx}}{\sigma_0} - 1 \right]$$

and

$$[12] \quad J_{ex} = -n e u_x \left[1 + \frac{\Sigma'_{xx} - \sigma_0}{\epsilon'_{xx} \sigma_0} \right]$$

where $\epsilon'_{xx} = 1 + \frac{4\pi i}{\omega} \sigma'_{xx}$. Also for transverse waves

$$[13] \quad E_y = - \frac{n e u_y}{\epsilon^t_{yy}} \frac{4\pi i}{\omega} \left(\frac{S}{c}\right)^2 \left[\frac{\Sigma_{yy}}{\sigma_0} - 1 \right]$$

and

$$[14] \quad J_{ey} = -n e u_y \left[1 + \frac{\Sigma_{yy} - \sigma_0}{\epsilon^t_{yy} \sigma_0} \right]$$

where $\epsilon_{yy}^t = 1 - \frac{4\pi i}{\omega} \left(\frac{S}{c}\right)^2 \sigma_{yy}$.

The work done on the electrons per unit time by the sound wave is (Blount 1959)

$$[15] \quad P = \frac{1}{2} \operatorname{Re} \left[\underline{J}_e^* \cdot \underline{E} + \frac{m \underline{u}^*}{e \tau} \cdot \left(\underline{J}_e + n e \underline{u} \right) \right]$$

where the electronic energy band has been assumed to be parabolic. The first term in [15] is the ohmic loss due to the presence of the self-consistent field. The second term is a viscous drag effect, which results from the electron-lattice collisions whereby the electrons reach local equilibrium with the lattice. This effect does not depend on the charge of the electrons, and is present even in the absence of the self-consistent field. However, since internal electric fields force the electrons to follow the lattice wave closely, the inclusion of a self-consistent field greatly reduces the collision drag term. As a result the first term in [15] dominates, except at very high frequencies. The attenuation of the sound wave is found by dividing the power absorbed per unit volume, P , by the energy flux $\frac{1}{2} \rho |\underline{u}|^2 S$ where ρ is the density of the lattice. Thus

$$\alpha = \frac{P}{\frac{1}{2} \rho |\underline{u}|^2 S} .$$

The attenuation of longitudinal and transverse waves is found by substituting [11], [12] and [13], [14] respectively, into [15].

For longitudinal waves we find

$$[16a] \quad \alpha_L = \frac{nm}{\rho S \tau} \operatorname{Re} \left\{ \frac{\epsilon_o}{\epsilon_{xx}^l} \left(1 - \frac{\sigma_{xx}^l}{\sigma_o} \right) \right\}$$

whereas for transverse waves

$$[16b] \quad \alpha_t = \frac{nm}{\rho S \tau} \operatorname{Re} \left\{ \frac{\epsilon_o^t}{\epsilon_{yy}^t} \left(1 - \frac{\sigma_{yy}^t}{\sigma_o} \right) \right\}$$

where $\epsilon_o = 1 + \frac{4\pi i}{\omega} \sigma_o$ and $\epsilon_o^t = 1 - \frac{4\pi i}{\omega} \left(\frac{S}{c} \right)^2 \sigma_o$.

The last two results are new expressions for ultrasonic attenuation.

So far, the coupling between the sound wave and the electrons has been assumed to be due to collisions and to a self-consistent electromagnetic field. A deformation potential tensor can also couple the electrons to the wave. If the deformation potential is a scalar, it affects only the interaction of electrons with longitudinal waves, and does not change the interaction with transverse waves. If a scalar deformation potential, C , is introduced into the Boltzmann equation (see Harrison 1960, or Tucker and Rampton 1972), and the expression for the power dissipation is suitably modified, it can be shown that the attenuation of acoustic waves is given by

$$[17] \quad \alpha_L = \frac{nm}{\rho S \tau} \operatorname{Re} \left\{ \frac{\epsilon_o}{\epsilon'_{xx}} \left[1 - \frac{\sigma'_{xx}}{\sigma_o} \right] + 2 D \frac{\epsilon_o - 1}{\epsilon'_{xx}} \left(1 - \frac{\sigma'_{xx}}{\sigma_o} \right) + D^2 \frac{\epsilon_o - 1}{\epsilon'_{xx}} \right\}$$

$$\text{where } D = \frac{C}{\frac{4\pi n e^2}{q^2}}$$

determines the relative importance of electromagnetic and deformation potential coupling. For example, if $C \gg \frac{4\pi n e^2}{q^2}$, the deformation potential will dominate. The three terms in [17] may be interpreted as follows. The first term is due to the self-consistent field plus the screened collision coupling. The last term is the screened deformation potential alone, and the second term is a cross term which includes contributions from all three mechanisms.

We now develop an alternative method which is valid in the quantum limit, and includes only the deformation potential interaction.

1.3 The Quantum Limit

If the energy $\hbar\omega$ of the externally impressed phonon is larger than the uncertainty in the electronic energy $\frac{\hbar}{\tau}$ due to the collisions, then one is said to be working in the quantum limit. In this limit quantum mechanical perturbation theory can be used to evaluate the attenuation of a sound wave. The following additional assumptions are made:

1. The electrons are free, except for dimensionality constraints.
2. The phonon dispersion is linear.
3. The phonon energy $\hbar\omega$ is much smaller than the Fermi energy.
4. The electron-phonon interaction is adequately described by the standard interaction Hamiltonian

$$H_{\text{int}} = C \sum_{\substack{\underline{k}, \underline{q} \\ \sigma}} \left(\frac{\hbar}{2\rho\omega} \right)^{\frac{1}{2}} |\underline{q}| \left(a_{\underline{q}}^+ - a_{-\underline{q}} \right) c_{\underline{k}-\underline{q}, \sigma}^+ c_{\underline{k}, \sigma}$$

where C is a scalar deformation potential, $a_{\underline{q}}^+$ is a phonon creation operator, and $c_{\underline{k}, \sigma}^+$ is an operator which creates an electron with wavevector \underline{k} and spin σ .

Most of the remainder of this section is material which has been described in detail elsewhere (Kittel 1963, Tucker & Rampton 1972). It is included here to provide a framework for dealing with the one and two dimensional systems. The probability per unit time that a

phonon of wavevector \underline{q} is absorbed by an electron is

$$W_{(-)} = \frac{2\pi}{\hbar} \sum_{\underline{k}} c^2 \left(\frac{\hbar}{2\rho\omega} \right) q^2 n(\underline{q}) f_0(\underline{k}) \left(1 - f_0(\underline{k}+\underline{q}) \right) \delta \left(\epsilon(\underline{k}) + \hbar\omega - \epsilon(\underline{k}+\underline{q}) \right)$$

and the probability that a phonon \underline{q} is emitted is

$$W_{(+)} = \frac{2\pi}{\hbar} \sum_{\underline{k}} c^2 \left(\frac{\hbar}{2\rho\omega} \right) q^2 \left(n(\underline{q}) + 1 \right) f_0(\underline{k}) \left(1 - f_0(\underline{k}-\underline{q}) \right) \delta \left(\epsilon(\underline{k}) - \hbar\omega - \epsilon(\underline{k}-\underline{q}) \right)$$

where the rates are normalized to unit volume, and $f_0(\underline{k})$, $n(\underline{q})$ are the equilibrium electron and phonon distribution functions respectively.

Acoustic attenuation can be defined as the net rate of absorption of phonons in the mode \underline{q} divided by the phonon flux $n(\underline{q})S$. Thus

$$\alpha = \frac{W_{(-)} - W_{(+)}}{n(\underline{q})S}$$

or

$$\alpha = \frac{2\pi}{\hbar} \frac{c^2 q^2}{S} \sum_{\underline{k}} \left(\frac{\hbar}{2\rho\omega} \right) \left(f_0(\underline{k}) - f_0(\underline{k}+\underline{q}) \right) \delta \left(\epsilon(\underline{k}) + \hbar\omega - \epsilon(\underline{k}+\underline{q}) \right)$$

where we have assumed that $kT \gg \hbar\omega$. This expression may be evaluated by converting the summation to an integral. Then

$$[18] \quad \alpha = \frac{1}{4\pi^2} \frac{C_m^2}{\rho S^2 \hbar^2} \int d^3k \left(f_0(\underline{k}) - f_0(\underline{k}+\underline{q}) \right) \delta \left(\epsilon(\underline{k}) + \hbar\omega - \epsilon(\underline{k} + \underline{q}) \right)$$

It is of interest to investigate which electronic states contribute to the attenuation.

Wavevector ('momentum') must be conserved in any phonon emission or absorption process, otherwise the matrix element of the electron-phonon interaction is zero. In an absorption process, for example, $\underline{k}' = \underline{k} + \underline{q}$. Furthermore, in the golden rule approximation used here, the transition rate is zero unless energy is also conserved. Thus

$$\epsilon(\underline{k}') = \epsilon(\underline{k}) + \hbar S q$$

For free electrons the energy conservation requirement reduces to

$$\frac{\hbar^2 \underline{k} \cdot \underline{q}}{m} = \hbar S q - \frac{\hbar^2 q^2}{2m} .$$

The energy and momentum conservation requirements define a set of electronic states which can interact with the sound wave. These states lie in the vicinity of a surface in \underline{k} space, across which an electron scatters in any phonon absorption or emission process (Pippard 1963). A cross-section of this interaction surface is shown in Fig. 5, for a three dimensional Fermi sphere. Clearly the major

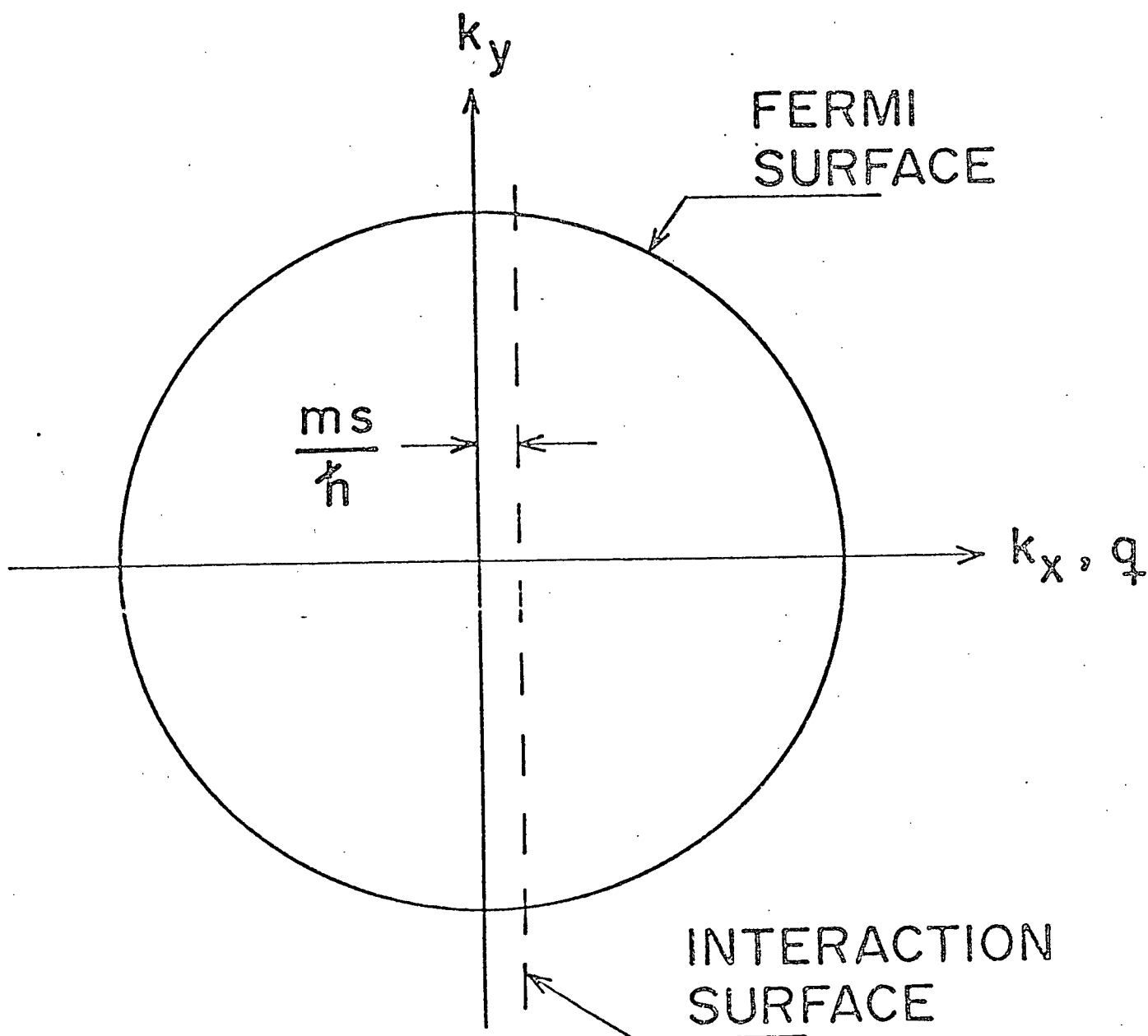


Fig. 5 - Cross-section of the Fermi sphere showing the interaction surface

contribution to the scattering rate will come from the neighbourhood of the Fermi surface where there are empty electronic states for the electrons to scatter into. As will be shown in a later section, this situation is drastically altered in one dimensional metals.

1.4 Metals

(i) Three Dimensional Metals

Acoustic attenuation in three dimensional metals has been studied extensively. The results will be presented here for comparison with the one and two dimensional cases. The transport equation method will be used first. For free electrons, and $kT \ll \epsilon_F$, the conductivity tensor $\underline{\sigma} = \underline{\Sigma}$ is given by

$$\begin{aligned} \sigma_{xx} &= \frac{\sigma_0}{1-i\omega\tau} \frac{3}{a^3} \left\{ a - \frac{1}{2} \left[\tan^{-1} (\Lambda - \omega\tau) + \tan^{-1} (\Lambda + \omega\tau) \right] \right. \\ &\quad \left. + \frac{1}{4} \log \left(\frac{1 + (\Lambda - \omega\tau)^2}{1 + (\Lambda + \omega\tau)^2} \right) \right\} \\ \sigma_{yy} &= \sigma_{zz} = \frac{\sigma_0}{1-i\omega\tau} \frac{3}{2a^3} \left\{ \left(\frac{a^2+1}{2} \right) \left[\tan^{-1} (\Lambda - \omega\tau) + \tan^{-1} (\Lambda + \omega\tau) \right] \right. \\ &\quad \left. - \frac{1}{2} \log \left[\frac{1 + (\Lambda - \omega\tau)^2}{1 + (\Lambda + \omega\tau)^2} \right] \right\} - a \end{aligned}$$

where $a = \frac{q\ell}{1-i\omega\tau}$, $\Lambda = q\ell$, and $\ell = v_F\tau$ is the mean free path of an electron at the Fermi surface. The other components of the conductivity tensor are zero. The sound wave is assumed to propagate in the x direction. The only non-zero component of \underline{R} is

$$[19] \quad R_x = \frac{\Lambda^2}{i\omega\tau(1-i\omega\tau)} - \frac{\sigma_{xx}}{3\sigma_0}.$$

Furthermore, if $S \ll v_F$, then the conductivity expression reduces to

$$[20a] \quad \sigma_{xx} = \frac{\sigma_0}{1-i\omega\tau} \frac{3}{a^3} \left\{ a - \tan^{-1} \Lambda - i \frac{\Lambda\omega\tau}{1+\Lambda^2} \right\}$$

$$[20b] \quad \sigma_{yy} = \sigma_{zz} = \frac{\sigma_0}{1-i\omega\tau} \frac{3}{2a^3} \left\{ (a^2 + 1) \left(\tan^{-1} \Lambda + \frac{i\Lambda\omega\tau}{1+\Lambda^2} \right) - a \right\}$$

The attenuation of longitudinal and transverse waves is found by substituting [19], [20a] and [20b] into [16a] and [16b]. In the low frequency limit ($\Lambda \ll 1$) where the screening is perfect ($\omega \ll \sigma_0$, σ'_{xx} for longitudinal waves, $\omega \ll \left(\frac{S}{c}\right)^2 \sigma_0$, $\left(\frac{S}{c}\right)^2 \sigma_{yy}$ for transverse waves) the attenuation in the absence of deformation potential coupling is

$$\alpha_L = \frac{4}{15} \frac{nm}{\rho S \tau} \Lambda^2$$

$$\alpha_t = \frac{1}{5} \frac{nm}{\rho S \tau} \Lambda^2$$

for longitudinal and transverse waves respectively. For higher frequencies in which $\Lambda > 1$, but the screening is still perfect, the following more general expressions may be used:

$$[21] \quad \alpha_L = \frac{nm}{\rho S \tau} \left[\frac{\Lambda^2 \tan^{-1} \Lambda}{3 (\Lambda - \tan^{-1} \Lambda)} - 1 \right]$$

$$\alpha_t = \frac{nm}{\rho S \tau} \left[\frac{2\Lambda^3}{3 [(1+\Lambda^2) \tan^{-1} \Lambda - \Lambda]} - 1 \right] .$$

In the high frequency limit ($\Lambda \gg 1$) where the screening is perfect, the attenuation is

$$\alpha_L = \frac{\pi}{6} \frac{nm}{\rho S} q v_F$$

$$\alpha_t = \frac{4}{3\pi} \frac{nm}{\rho S} q v_F$$

For comparison with the result of the quantum calculation, the expression for the attenuation, which includes the deformation potential may also be evaluated in the quantum limit. In this limit the relaxation time is allowed to become large so that $\Lambda \gg 1$, and $\omega_p^2 \tau \gg \omega$, where ω_p is the plasma frequency. When these conditions are satisfied, the expression [17] for the attenuation in the presence of a deformation potential, reduces to

$$\alpha_L = \frac{nm}{\rho S \tau} \operatorname{Re} \left\{ \frac{\epsilon_o}{\epsilon_{xx}^i} \left(1 + \frac{q^2 C}{4\pi n e^2} \right)^2 \right\}.$$

Substituting the appropriate limit of the conductivity [20a], into the last equation, we obtain

$$[22] \quad \alpha_L = \frac{\pi}{6} \frac{nm}{\rho S} \left(\frac{C + \frac{4\pi n e^2}{q^2}}{\frac{2}{3} \epsilon_F} \right)^2 \frac{q v_F}{(1 + (q R_3)^{-2})^2}$$

where $R_3 = \left(\frac{\epsilon_F}{6\pi n e^2} \right)^{1/2}$ is the three dimensional Fermi-Thomas screening

length. It is interesting to note that $\left(1 + (q R_3)^{-2}\right)$ is the Fermi-Thomas dielectric constant valid for $q \ll \frac{mv_F}{\hbar}$.

In the quantum limit, the attenuation may also be found by integrating [18]. The result is

$$[23] \quad \alpha_L = \frac{\pi}{6} \frac{nm}{\rho S} \left(\frac{C}{\frac{2}{3} \epsilon_F} \right)^2 q v_F .$$

A comparison of the last result with [22] reveals two things. First the quantum calculation does not take into account the screening of the sound wave by the conduction electrons. Secondly, the electromagnetic coupling mechanism is equivalent to a deformation potential of strength $\frac{4\pi ne^2}{q^2}$. This is just the potential arising from a charge density oscillation of the form ne^{iqx} . It follows from [22] that when $qR_3 \ll 1$ the self consistent field coupling is equivalent to a deformation potential of strength $\frac{2}{3} \epsilon_F$. The electromagnetic electron-lattice coupling normally dominates in metals at all reasonable frequencies. To summarize, the quantum approach gives the transport result if an electromagnetic coupling energy of $\frac{4\pi ne^2}{q^2}$ is added to the deformation potential and the entire interaction potential is screened by dividing by the Fermi-Thomas dielectric constant.

(ii) Two Dimensional Metals

By two dimensional metals we mean metals in which the electronic energy depends on k_x and k_y but not on k_z . For example, the Fermi surface of a two dimensional free electron gas is a cylinder, centered on the k_z axis. Associated with the two dimensional nature of the electron gas, there are three modes of sound propagation in addition to the longitudinal and transverse waves propagating in the conducting plane and polarized in the conducting plane. First there is a transverse wave travelling in the conducting plane and polarized perpendicular to the conducting plane. Secondly there are two modes, one longitudinal and one transverse, propagating perpendicular to the conducting plane.

Waves polarized in the non-conducting direction cannot deliver energy to the electrons in the linear approximation considered here. Hence these waves are not attenuated. The remaining special wave is the transverse wave propagating in the non-conducting direction. Referring back to the expression for the conductivity tensor [4a], we see that for this mode $\underline{q} \cdot \underline{v} = 0$, hence $\sigma_{xx} = \sigma_{yy} = \frac{\sigma_0}{1-i\omega\tau}$ and $\sigma_{zz} = 0$. This value for the conductivity substituted into [16b] yields the attenuation

$$[24] \quad \alpha_t = \frac{nm}{\rho S \tau} (\omega\tau)^2 \left\{ 1 + (\omega\tau)^2 \left[1 + \left(\frac{S}{c}\right)^2 \left(\frac{\omega_p}{\omega}\right)^4 \right] \right\}^{-1}$$

which is much smaller than the corresponding three dimensional result in all limits.

In calculating the attenuation of the two modes travelling in the conducting plane and polarized in the conducting plane, we use the same procedure as in the three dimensional case. The non-zero components of the conductivity tensor for a two dimensional free electron system with $kT \ll \epsilon_F$ are given by

$$[25a] \quad \sigma_{xx} = \frac{\sigma_0}{1-i\omega\tau} \frac{2}{a^2} \left\{ 1 - \frac{1}{\sqrt{1+a^2}} \right\}$$

$$[25b] \quad \sigma_{yy} = \frac{\sigma_0}{1-i\omega\tau} \frac{2}{a^2} \left\{ \sqrt{a^2+1} - 1 \right\}$$

where the symbols have the same meaning as in the three dimensional problem. The only non-zero component of \underline{R} is

$$R_x = \frac{\Lambda^2}{i\omega\tau(1-i\omega\tau)} \frac{\sigma_{xx}}{2\sigma_0}$$

which differs only in the factor of 2 from the corresponding three dimensional result.

The attenuation of the longitudinal and transverse modes is found by substituting the last three results into [16a] and [16b] respectively. In the low frequency ($\Lambda \ll 1$) perfect screening limit, the attenuation is

$$\alpha_L = \alpha_t = \frac{1}{4} \frac{nm}{\rho S \tau} \Lambda^2 .$$

For arbitrary Λ , and perfect screening

$$[26] \quad \alpha_L = \alpha_t = \frac{nm}{\rho S \tau} \left[\frac{\Lambda^2}{2(\sqrt{1+\Lambda^2}-1)} - 1 \right] .$$

In the large Λ limit the last result simplifies to

$$\alpha_L = \alpha_t = \frac{1}{2} \frac{nm}{\rho S} q v_F .$$

For purposes of comparison with the result of the quantum calculation, the attenuation of longitudinal waves in the long relaxation time, or quantum limit, is

$$[27] \quad \alpha_L = \frac{1}{2} \frac{nm}{\rho S} \left(\frac{C + \frac{4\pi n e^2}{q}}{\epsilon_F} \right)^2 \frac{q v_F}{(1 + (q R_2)^{-2})^2}$$

where $R_2 = \left(\frac{\epsilon_F}{4\pi n e^2} \right)^{1/2}$ is the two dimensional Fermi-Thomas screening length. The attenuation in this limit may also be found by evaluating [18] for a two dimensional electron gas, which gives

$$[28] \quad \alpha_L = \frac{1}{2} \frac{nm}{\rho S} \left(\frac{C}{\epsilon_F} \right)^2 q v_F .$$

As in the three dimensional case the quantum result [28] is identical

with the Boltzmann equation result [27], except that the latter includes electromagnetic coupling and screening.

A graph of the attenuation of longitudinal acoustic waves in two and three dimensional metals, calculated from eqns. [21] and [26] as a function of Λ ($\equiv q\ell$) is shown in Fig. 6. The similarity of the two curves in Fig. 6 suggests the following interpolation formula for the inverse tangent function:

$$\tan^{-1}x \approx x / \left[1 + \frac{2}{\pi} \left(\sqrt{1 + x^2} - 1 \right) \right].$$

This formula is asymptotically exact for large and small x and deviates from the exact value of $\tan^{-1}x$ by a maximum of about 1.1% for $x \approx 2$.

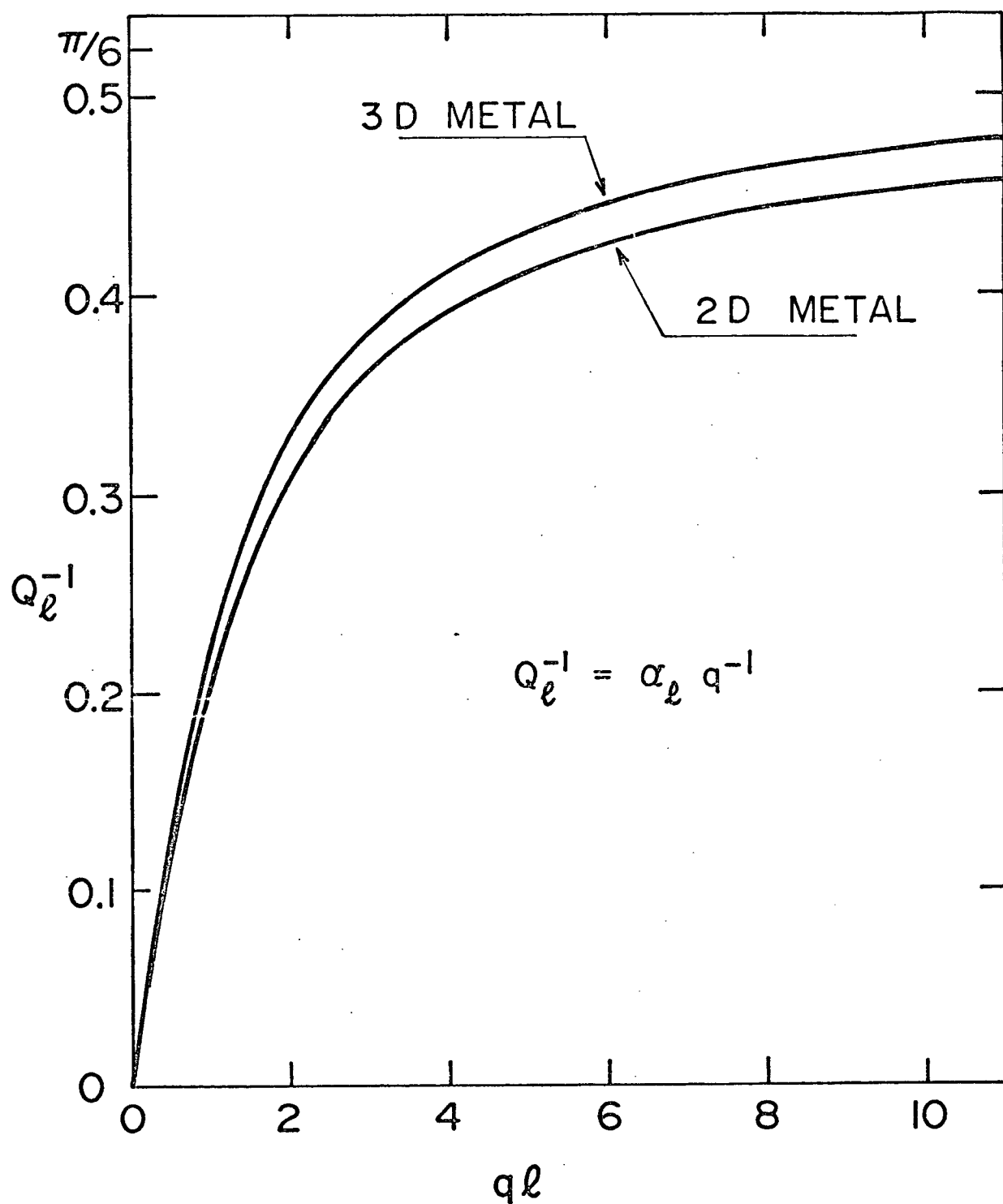


Fig. 6 - Acoustic attenuation as a function of $q\ell$ for 3D and 2D metals in units of $\frac{nmV_F}{\rho S}$ as calculated from [21] and [26]

(iii) One Dimensional Metal

We now investigate acoustic attenuation in one dimensional metals. By one dimensional, we mean that the electronic energy depends only on k_x and not on k_y or k_z . As a result the Fermi surface consists of two parallel planes, perpendicular to the k_x axis.

As in the two dimensional metal, there are five distinct cases depending on the relative orientation of the conducting axis, the sound propagation direction and the polarization vector. Only two of the waves interact with the electrons. One is a transverse wave polarized along the conducting axis, and the other is a longitudinal wave travelling along the conducting axis. The attenuation of the first of these is identical to the attenuation of the similar mode in the two dimensional metal; hence it is also given by [24].

In the case of the longitudinal wave propagating along the conducting axis, it is instructive to consider the quantum limit first. The calculation is similar to the two dimensional problem except that the electronic energy $\epsilon(\underline{k})$ is a function of k_x only. The result, however, is quite different. The reason for the difference is most easily understood by examining the interaction surface. As has been described above, the interaction surface defines the electron \underline{k} states, which are allowed by momentum and energy conservation to

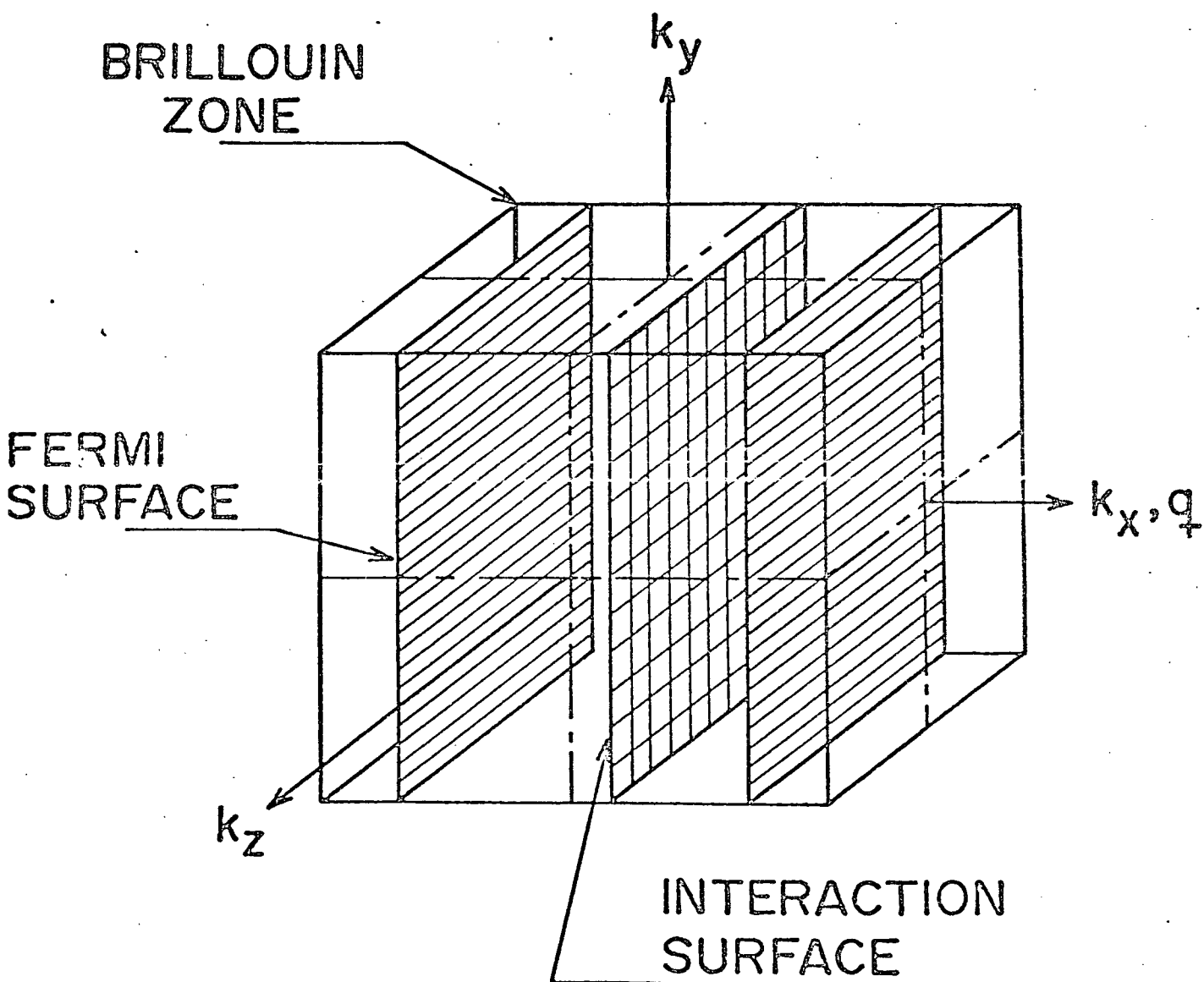


Fig. 7 - Fermi surface and interaction surface in a one dimensional metal

interact with a sound wave of wavevector $q \ll k_F$. Unlike the interaction surface for the two and three dimensional cases, the interaction surface for one dimension does not intersect the Fermi surface (see Fig.7). Although this feature does not restrict electrons from scattering with phonons of wavevector $\sim 2k_F$ in the present case where $q \ll k_F$, we expect a much reduced attenuation, which approaches zero at low temperatures. In fact, this conclusion is borne out by evaluating [18] in the $S \ll v_F$ limit:

$$[29] \quad \alpha_L = 2\pi \frac{nm}{\rho S} \left(\frac{C}{2\epsilon_F} \right)^2 \left(\frac{\epsilon_F}{kT} \right) e^{-\frac{\epsilon_F}{kT}} q v_F .$$

This expression differs from the corresponding two and three dimensional results by the presence of the factor $\left(\frac{\epsilon_F}{kT} \right) e^{-\frac{\epsilon_F}{kT}}$. Clearly α_L approaches zero as T goes to zero.

The quantum limit may also be extracted from the transport integrals. However, the $\Lambda, \omega\tau \rightarrow \infty$ limit must be taken with care. Since the acoustic attenuation expression contains a real part operator, a small real part may be significant even when the imaginary part is much larger. The non-zero part of the conductivity tensor for longitudinal sound waves in a one dimensional metal may be written

$$\sigma_{xx} = -\frac{ne^2}{2v_F} \frac{i}{q} \int \frac{v^2 \left(-\frac{\partial f}{\partial \epsilon} \right) dv}{v - S \left(1 + \frac{i}{\omega\tau} \right)} .$$

This integral may be evaluated in the $\omega\tau \rightarrow \infty$ limit by using the functional relation

$$\lim_{\omega\tau \rightarrow \infty} \frac{1}{v - S \left(1 + \frac{i}{\omega\tau}\right)} = P \frac{1}{v-S} + i\pi \delta(v - S)$$

where P means principal part. The real part of the conductivity (imaginary part of the integral) may now be found exactly, and the imaginary part can be approximated by treating $\left(-\frac{\partial f}{\partial \epsilon}\right)$ as a delta function at $\pm v_F$. The result is

$$\sigma_{xx} = \frac{\sigma_0}{\Lambda} \left\{ 2\pi \left(\frac{S}{v_F}\right)^2 \left(\frac{\epsilon_F}{kT}\right) e^{-\frac{\epsilon_F}{kT}} - i \frac{S}{v_F} \right\}.$$

Once again there is a simple relation between \underline{R} and $\underline{\sigma}$. The only non-zero component of \underline{R} is

$$R_x = \frac{\Lambda^2}{i\omega\tau(1-i\omega\tau)} \frac{\sigma_{xx}}{\sigma_0}.$$

When the last two results are substituted into the attenuation equation, [17], we obtain

$$[30] \quad \alpha_L = 2\pi \frac{nm}{\rho S} \left(\frac{\epsilon_F}{kT}\right) e^{-\frac{\epsilon_F}{kT}} \left(\frac{C + \frac{4\pi ne^2}{q^2}}{2\epsilon_F} \right)^2 \left(\frac{qv_F}{1 + (qR_1)^{-2}} \right)^2$$

where $R_1 = \left(\frac{\epsilon_F}{2\pi ne^2}\right)^{1/2}$ is the one dimensional Fermi-Thomas screening length. The transport method once again gives the same result [30], as the quantum method [29], barring the expected failure of the quantum calculation to include electromagnetic coupling and screening.

The extreme quantum limit that is considered above ($\omega\tau \gg 1$) is unlikely to be attainable in practice. In this limit the delta function in [18] implies strict energy conservation in electron phonon collision processes, and the attenuation arises from the thermal broadening of the Fermi surface. If the condition $\omega\tau \gg 1$ is relaxed to the weaker condition $\Lambda \gg 1$, the finite collision time may be taken into account by replacing the delta function in [18] by the Lorentzian

$$\frac{\hbar}{\pi\tau} \left[\left(\epsilon(k) + \hbar\omega - \epsilon(k+q) \right)^2 + \left(\frac{\hbar}{\tau} \right)^2 \right]^{-1}$$

The ultrasonic attenuation, then arises from the intersection of the Fermi surface with the tail of the Lorentzian and is given by

$$[31] \quad \alpha_{\ell} = \frac{n m}{\rho S \tau} \left(\frac{c}{2\epsilon_F} \right)^2 .$$

Aside from a factor of two, this expression differs from the corresponding two dimensional result [28] by a factor of Λ^{-1} . This factor reflects the non-intersection of the interaction and Fermi surfaces. The attenuation [31] may also be obtained using the transport equation method, by neglecting the self-consistent field and collision drag, in favour of the deformation potential.

As pointed out earlier, the self-consistent field, electron sound wave coupling, is expected to dominate in metals at least in the low frequency limit. We first try to obtain an expression analogous to the two dimensional result [26], using the transport equation method. However, if the same approximations are made as in the two (or three) dimensional cases, the attenuation in a one dimensional electron gas is identically zero. To obtain a non-zero result we relax the zero temperature approximation and calculate the transport tensors to order $\left(\frac{kT}{\epsilon_F}\right)^2$. The transport integrals depend on temperature through the temperature dependence of the Fermi function. As the temperature rises from zero, the unit step in the Fermi function broadens to a width of order kT and the chemical potential increases from the Fermi energy to

$$\mu = \epsilon_F \left(1 + \frac{\pi^2}{12} \left(\frac{kT}{\epsilon_F} \right)^2 \right).$$

Provided that both of these effects are included, the non-zero component of the conductivity tensor is found to be

$$[32] \quad \sigma_{xx} = \frac{\sigma_0}{1 - i\omega\tau} \frac{1}{1 + a^2} \left\{ 1 - \theta \frac{(3 - a^2) a^2}{(1 + a^2)^2} \right\}$$

to first order in θ where $\theta = \frac{\pi^2}{12} \left(\frac{kT}{\epsilon_F} \right)^2 \ll 1$. Similarly

$$[33] \quad R_x = \frac{\Lambda^2}{i\omega\tau(1 - i\omega\tau)} \frac{\sigma_{xx}}{\sigma_0} (1 - \theta).$$

Substituting [32] and [33] into [17] we obtain

$$[34] \quad \alpha_{\ell} = \frac{\pi^2}{3} \frac{n}{\rho S \tau} \left(\frac{kT}{\epsilon_F} \right)^2 \frac{\Lambda^2}{1 + \Lambda^2}$$

for a free electron gas. This expression is valid for arbitrary Λ , provided that the perfect screening limit holds ($\omega \ll \sigma_o, \sigma'_{xx}$) and that Λ is not so large that the extreme quantum limit applies.

The transport equation method, in the relaxation time approximation, may also be used to calculate the ultrasonic attenuation for an arbitrary band structure, although the general expression which results, is much more complicated than [17]. However, in the perfect screening limit the expression for the attenuation is once again quite simple. We then find that the attenuation of longitudinal waves travelling in the x direction is given by

$$[35] \quad \alpha_{\ell} = \frac{n}{\rho S \tau} R_e \left\{ \frac{\sigma_o}{\sigma'_{xx}} - \frac{\Sigma_{xx}}{\sigma_{xx}} \right\}$$

where terms of order $\left(\frac{\omega}{\sigma_o}\right)^2, \left(\frac{\omega}{\sigma'_{xx}}\right)^2$ have been ignored, and the transport tensors $\underline{\sigma}$, $\underline{\Sigma}$ and \underline{R} are given by [4a], [4b] and [4c] respectively.

Similarly $\sigma_o = \frac{ne^2\tau}{m}$ where

$$n = \frac{2}{(2\pi)^3} \int f(k) d^3k$$

is the total number of electrons in the conduction band. Notice that the m dependence of [35] is fictitious since both σ_0 and $\underline{\Sigma}$ are defined to be proportional to m^{-1} .

The one dimensional transport integrals are sufficiently simple that the temperature dependent part of the attenuation may be evaluated for an arbitrary band structure, in the perfect screening limit. If the band structure in the vicinity of the Fermi surface is given by

$$\epsilon(k) = \epsilon_F + \hbar(k - k_F) v_F + \frac{\hbar^2(k - k_F)^2}{2m^*}$$

where $v_F = \left. \frac{1}{\hbar} \frac{\partial \epsilon}{\partial k} \right|_{k = k_F}$ and $(m^*)^{-1} = \left. \frac{1}{\hbar^2} \frac{\partial^2 \epsilon}{\partial k^2} \right|_{k = k_F}$

then the temperature dependence of the Fermi level is

$$\mu = \epsilon_F + \frac{\pi^2}{12} \frac{(kT)^2}{\epsilon_F'}$$

where $\epsilon_F' = \frac{1}{2} m^* v_F^2$. The ultrasonic attenuation is given by

$$[36] \quad \alpha_L = \frac{\pi^2}{6} \frac{nm^*}{\rho S \tau} \left(1 + \frac{\hbar k_F}{m^* v_F} \right) \left(\frac{kT}{\epsilon_F'} \right)^2 \frac{\Lambda^2}{1 + \Lambda^2}$$

where $\Lambda = qv_F \tau$ as before and the total number of carriers in the band is $n = D_F \hbar k_F v_F$ where D_F is the density of states at the Fermi

surface. The last result closely resembles the free electron result [34].

The non-intersection of the Fermi surface with the interaction surface is reflected in the fact that the attenuation [34] becomes frequency independent for $\Lambda \gg 1$, instead of approaching a linear frequency dependence. The same behaviour has already been noted in [31] for deformation potential coupling. On the other hand, the absence of the leading term in the ultrasonic attenuation in the $\Lambda \ll 1$ limit cannot be explained on the basis of the energy and wavenumber selection rules. In fact it is easy to show, using the collision broadened energy conservation requirement that for $\Lambda \ll 1$ electrons at the Fermi surface are just as likely to interact with the sound wave as the electrons on the interaction surface. The reason for the small attenuation in the one dimensional metal for $\Lambda \ll 1$ lies in the absence of the higher order relaxation times τ_j , $j = 2, 3, \dots$, discussed by Bhatia and Moore (1960). Furthermore the expression [34] (or [36]) should be taken only as an order of magnitude estimate of the attenuation since another term of order $\left(\frac{kT}{\epsilon_F}\right)^2$ has been omitted by assuming the sound wave to be isothermal [Akhiezer, Kaganov and Liubarskii (1957)].

1.5 Anisotropy of Attenuation

In one and two dimensional metals it is possible to adjust the position of the interaction surface simply by changing the angle of propagation of the acoustic wave relative to the conducting direction (or plane). In the quantum limit, when the interaction

surface intersects an extremum of the Fermi surface there is a large enhancement in the sound absorption. For this reason the attenuation of acoustic waves will be very anisotropic in one and two dimensional metals, in the quantum limit. In this section we assume for convenience that the acoustic wave is coupled to the electrons only through a deformation potential C .

(i) One Dimensional Metal

The interaction surface has been defined above as the surface in k space for which $\epsilon(\underline{k}+\underline{q}) - \epsilon(\underline{k}) = \hbar q S$ with $q \ll k_F$. In a one dimensional metal the electronic energies depend only on k_x so that the definition of the interaction surface reduces to

$$\epsilon(k_x + q \cos \theta) - \epsilon(k_x) = \hbar q S$$

for a one dimensional metal in which the acoustic wave propagates at an angle θ relative to the conducting direction. Note that changing the direction of \underline{q} relative to the conducting axis is mathematically equivalent to replacing the speed of sound S by $S/\cos \theta$. This direction dependence of the apparent velocity of sound has a drastic effect on the ultrasonic attenuation in the quantum limit.

First we consider the collisionless quantum regime in which $\omega\tau \gg 1$. As was pointed out in the previous section, in this limit the absorption processes arise from the intersection of the exponential tail of the Fermi-Dirac distribution function with the energy conserving δ

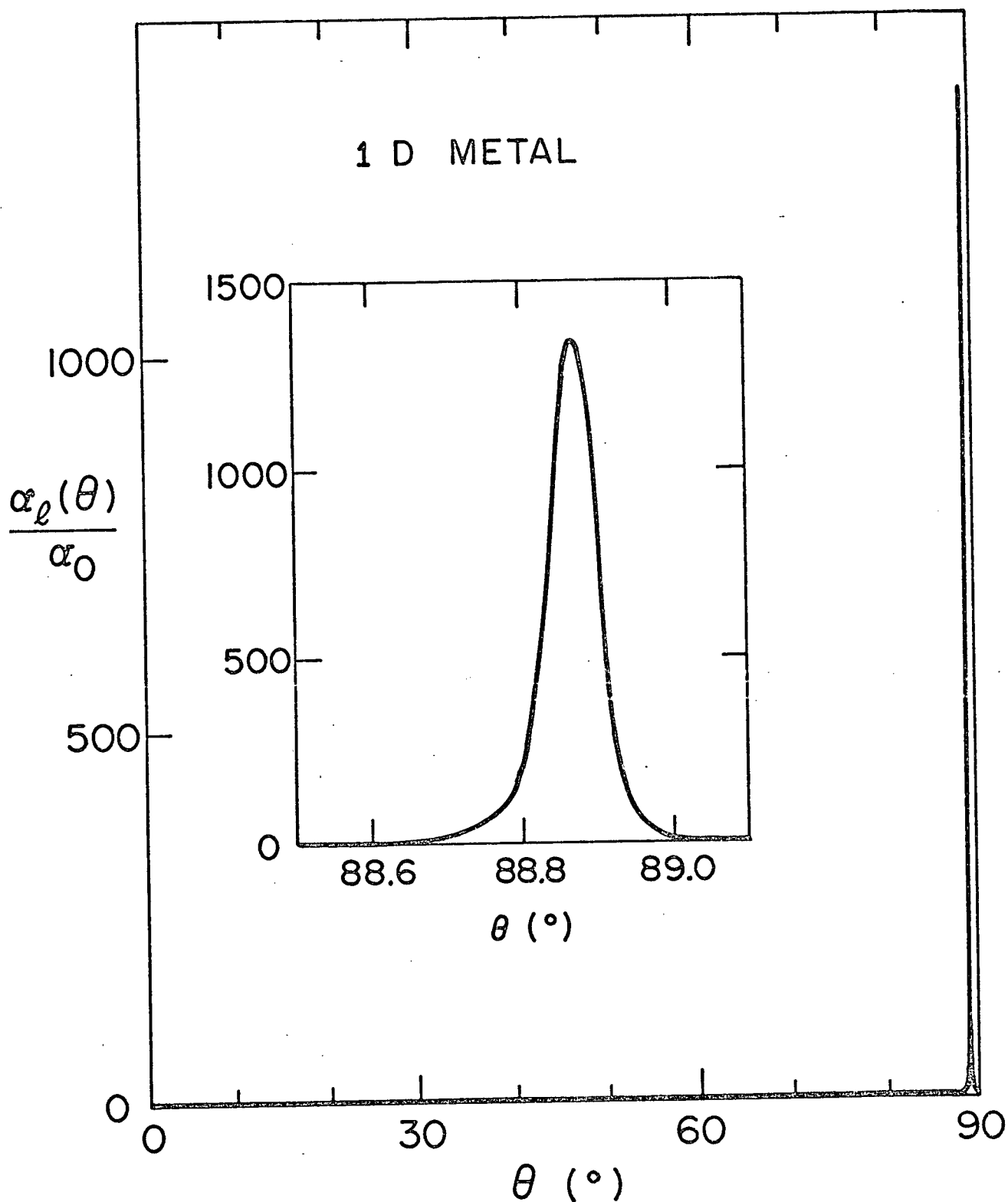


Fig. 8 - Angular dependence of ultrasonic attenuation in 1D metal

calculated from [37] for $T = 300\text{K}$ normalized to $\alpha_0 = \frac{\pi}{2} \frac{nm}{\rho S} \left(\frac{c}{2\epsilon_F} \right)^2 q v_F$.

The inset is an enlargement of the peak attenuation near $\theta = 90^{\circ}$.

function. Evaluating [18] we find

$$[37] \quad \alpha_{\ell}(\theta) = \frac{\pi}{2} \frac{nm}{\rho S} \left(\frac{C}{2\epsilon_F} \right)^2 \frac{\epsilon_F}{kT} \frac{qv_F}{\cos \theta} \operatorname{sech}^2 \left[\left(\frac{mS^2}{2 \cos^2 \theta} - \epsilon_F \right) / kT \right].$$

This result reduces to [29] as $\theta \rightarrow 0$ and goes to zero as $\theta \rightarrow \pi/2$.

At intermediate values of θ the attenuation goes through a large maximum when the interaction surface touches the Fermi surface.

The θ dependence of the absorption is shown in Fig. 8. In this figure, TTF-TCNQ material parameters taken from Table I have been used.

TABLE I

- TTF-TCNQ Material Parameters

n	$2.8 \times 10^{21} \text{ cm}^{-3}$	
ρ	1.62 g/cm^3	
S	$4 \times 10^5 \text{ cm/S}$	
TTF Band [†]		TCNQ Band [†]
m	$8 m_0$	$4 m_0$
v_F	0.5×10^7	10^7 cm/S
ϵ_F	0.5×10^3	10^3 K
b axis scattering time (60K)		$5 \times 10^{-14} \text{ s}$

[†] Berlinsky et al (1974)

The absorption peak occurs at $\theta_{\max} = \cos^{-1} (S/v_F)$ and has an angular width of order S/v_F radians. The peak absorption is

$$\alpha_{\ell\max} = \frac{\pi}{2} \frac{nm}{\rho S} \left(\frac{C}{2\epsilon_F} \right)^2 \frac{\epsilon_F}{kT} \frac{v_F}{S} q v_F$$

for $kT > \hbar\omega$ and

$$\alpha_{\ell\max} = \frac{\pi}{2} \frac{nm}{\rho S} \left(\frac{C}{2\epsilon_F} \right)^2 \frac{\epsilon_F}{\hbar\omega} \frac{v_F}{S} q v_F$$

for $kT < \hbar\omega$. The first result is a factor of order $(\epsilon_F/kT)(v_F/S)$ larger than the corresponding three dimensional result [23] reflecting the fact that in a one dimensional metal the interaction surface can intersect all of one sheet of the Fermi surface at once, rather than just a narrow ring as in a three dimensional metal.

When the condition $\omega\tau \gg 1$ is relaxed to the weaker condition $\Lambda \gg 1$, the attenuation in a one dimensional metal comes from the intersection of the Fermi surface with the tails of the broadened energy conserving " δ " function. If we replace the δ function in [18] by a Lorentzian, as discussed in the preceeding section, then in the low temperature limit where the Fermi surface is sharply defined, a trivial integration leads to

$$[38] \quad \alpha_{\ell}(\theta) = \frac{nm}{\rho S \tau} \left(\frac{C}{2\epsilon_F} \right)^2 \frac{\Lambda^4 \cos^2 \theta}{(1 + \Lambda^2 \cos^2 \theta)^2}$$

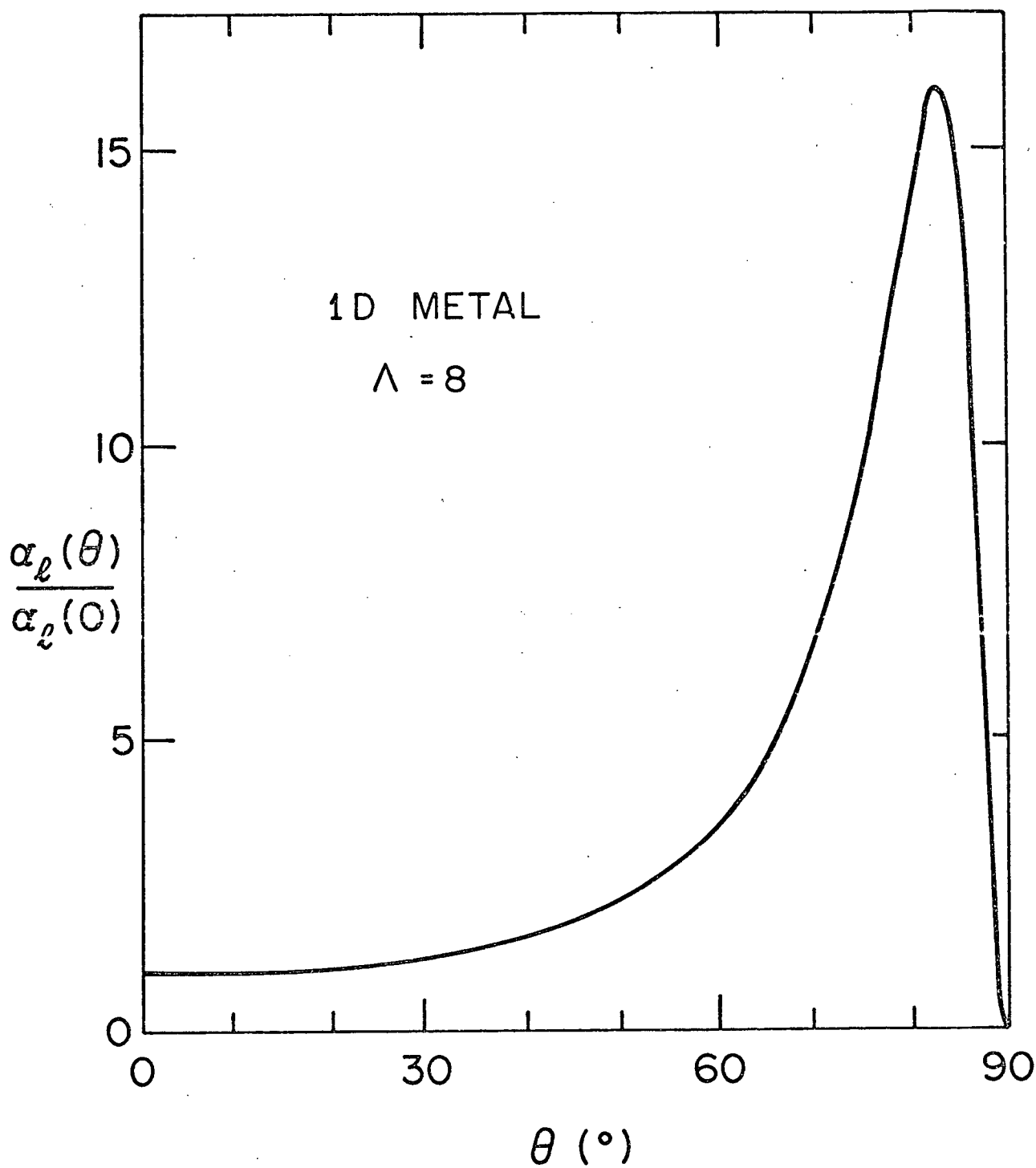


Fig. 9 - Angular dependence of ultrasonic attenuation in a 1D metal calculated from [38] with $\Lambda = 8$.

for the dependence of the attenuation on the propagation direction. This expression reduces to the earlier results at $\theta = 0$ ([31]) and $\pi/2$, and has a peak at $\theta_{\max} = \cos^{-1}(1/\Lambda)$. The peak value of the attenuation is much smaller than in the collisionless ($\omega\tau \gg 1$) regime. The peak attenuation is

$$\alpha_{\ell\max} = \frac{nm}{\rho S \tau} \left(\frac{C}{2\epsilon_F} \right)^2 \frac{\Lambda^2}{4}$$

which is a factor of order Λ larger than the corresponding three dimensional result. A plot of $\alpha_{\ell}(\theta)$ for $\Lambda = 8$ is shown in Fig. 9.

(ii) Two Dimensional Metals

The ultrasonic attenuation in two dimensional metals is also anisotropic in the quantum limit. In two dimensional metals there is a large peak in the attenuation when the interaction surface moves out to touch the surface of the Fermi cylinder tangentially. This peak occurs when the acoustic wave propagation direction is nearly perpendicular to the conducting plane. We now use [17] to calculate the attenuation of an acoustic wave propagating at an angle θ to the conducting plane in a two dimensional metal.

In the extreme quantum limit in which $\omega\tau \gg 1$ and energy is strictly conserved in electron-phonon collision processes

$$\alpha_{\ell}(\theta) = \frac{1}{2} \frac{nm}{\rho S} \left(\frac{C}{\epsilon_F} \right)^2 \frac{\epsilon_F}{\hbar\omega} \left[\left(1 - \frac{S^2}{v_F^2 \cos^2 \theta} + \frac{\hbar\omega}{\epsilon_F} \right)^{\frac{1}{2}} - \left(1 - \frac{S^2}{v_F^2 \cos^2 \theta} - \frac{\hbar\omega}{\epsilon_F} \right)^{\frac{1}{2}} \right] \frac{qv_F}{\cos \theta}$$

for $kT > \hbar\omega$. In this expression when the argument of the square root is negative the result is taken to be zero. With this proviso the attenuation is zero at $\theta = \pi/2$ and matches the previous result [28] at $\theta = 0$. For $\cos\theta > S/v_F$

$$[39] \quad \alpha_{\ell}(\theta) \approx \left(\cos^2\theta - \frac{S^2}{v_F^2} \right)^{-\frac{1}{2}} \alpha_{\ell}(0)$$

where $\alpha_{\ell}(0)$ is given by [28]. For θ near $\theta_{\max} = \cos^{-1}(S/v_F)$ the attenuation reaches a peak of

$$\alpha_{\ell\max} = \frac{v_F}{S} \left(\frac{2\epsilon_F}{\hbar\omega} \right)^{\frac{1}{2}} \alpha_{\ell}(0).$$

A non-zero temperature ($kT > \hbar\omega$) broadens the sharp Fermi surface and reduces the peak attenuation to

$$\alpha_{\ell\max} \sim \frac{v_F}{S} \left(\frac{\epsilon_F}{kT} \right)^{\frac{1}{2}} \alpha_{\ell}(0).$$

When $kT > \hbar\omega$ the attenuation as a function of θ is given by

$$[40] \quad \alpha_{\ell}(\theta) = \frac{1}{\cos\theta} \left(\frac{\epsilon_F}{kT} \right)^{\frac{1}{2}} \alpha_{\ell}(0) \int x^{-\frac{1}{2}} \operatorname{sech}^2(x-e) dx$$

with

$$e = \left(1 - \frac{S^2}{v_F^2 \cos^2\theta} \right) \frac{\epsilon_F}{kT}.$$

The integral in [40] must be done numerically. However, for $\cos\theta > S/v_F$

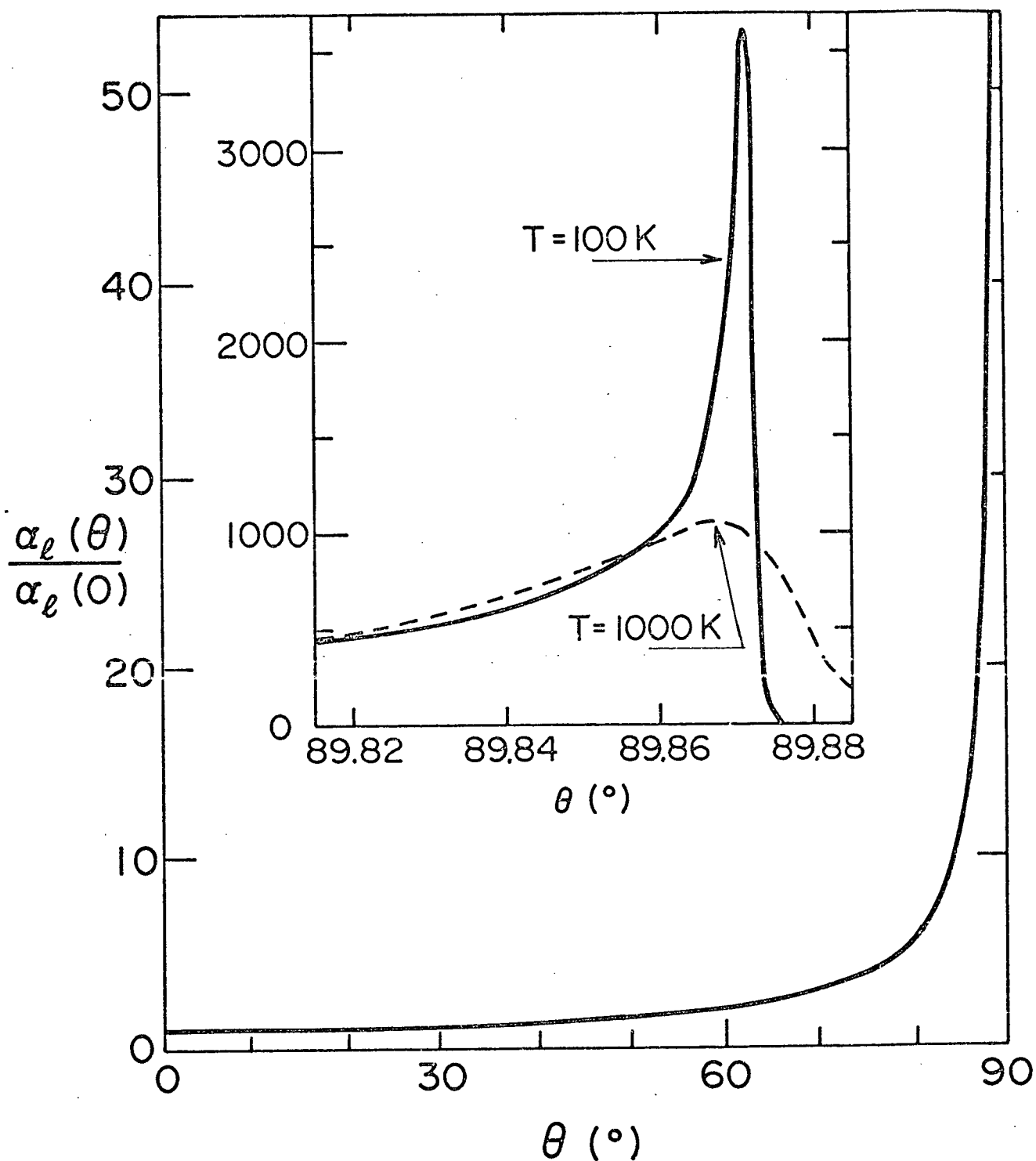


Fig. 10 - Angular dependence of ultrasonic attenuation in a 2D metal calculated from [40]. The inset shows the peak attenuation with an expanded horizontal scale.

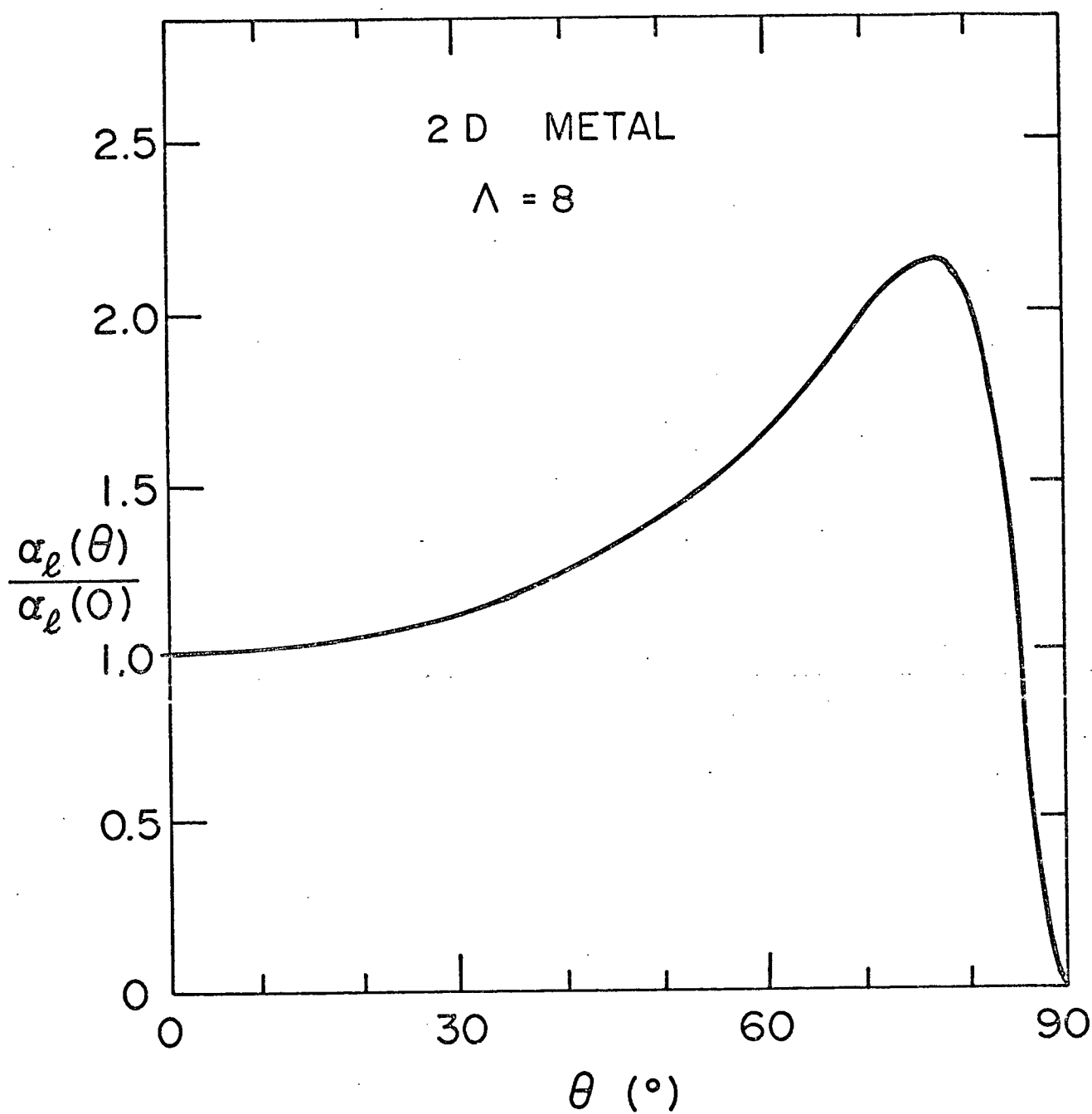


Fig. 11 - Angular dependence of ultrasonic attenuation in a 2D metal calculated from [41] with $\Lambda = 8$.

and at temperatures low compared to the Fermi temperature the last result ([40]) is equal to [39] to a good approximation. A plot of the attenuation as a function of angle is shown in Fig. 10, using $\epsilon_F = 10^4 K$ and $S/v_F = 10^{-3}$.

It is unlikely that the extreme quantum limit ($\omega\tau \gg 1$) can be achieved in practice. If the condition $\omega\tau \gg 1$ is relaxed to the more realistic condition $q\ell \gg 1$ then there is no longer strict energy conservation in electron-phonon scattering processes. In this case the δ function in [18] is replaced by a Lorentzian as described above. In the low temperature limit the two dimensional integration in [18] may be done exactly for arbitrary direction of sound propagation. The result is

$$[41] \quad \alpha_\ell(\theta) = \frac{2}{\pi} \left[\frac{\tan^{-1}(\Lambda \cos \theta)}{\Lambda \cos \theta} - \frac{1}{1 + \Lambda^2 \cos^2 \theta} \right] \Lambda \alpha_\ell(0).$$

This expression reduces to the collisionless result [40] at $\theta = 0, \pi/2$; however, just as in the one dimensional case collisions drastically reduce the acoustic absorption peak near $\theta = \pi/2$. A plot of $\alpha_\ell(\theta)$ as a function of θ is shown in Fig. 11 for $\Lambda = 8$. The peak attenuation is

$$\alpha_{\ell_{\max}} = 0.226 \Lambda \alpha_\ell(0)$$

which occurs at an angle $\theta_{\max} = \cos^{-1}(1.825/\Lambda)$ with respect to the conducting plane. Just as in the one dimensional case the peak

attenuation at $\theta = \theta_{\max}$ in the two dimensional metal is a factor of order Λ larger than the corresponding isotropic attenuation in a three dimensional metal.

1.6 Summary

We have extended the theory of ultrasonic attenuation in metals so that this theory may be applied to metals whose electronic band structures are one or two dimensional. Our results are valid for arbitrary values of Λ and include electron-phonon coupling via a scalar deformation potential as well as coupling via collisions and via the self-consistent electric field which arises from the response of the electrons to the sound wave. We have shown that the ultrasonic attenuation in one and two dimensional systems differ significantly from well-known results for three dimensional systems. In particular the attenuation is shown to be anomalously small and strongly temperature dependent for metallic one dimensional systems. In addition the attenuation is shown to be highly anisotropic in one and two dimensional metals in the quantum limit.

There are other applications of the theory in addition to the application to quasi one and two dimensional metals. For example, it may be applied to the attenuation resulting from an accumulation layer in an MOS junction, or to the attenuation associated with layered metal-insulator heterostructures. The theory also applies to a three dimensional electron gas in a strong magnetic field. In this case, one dimensional behavior results from the quantization of the electronic

motion in the plane perpendicular to the applied field. The Fermi surface for a particular Landau level may be "tuned" to match the interaction surface by varying the magnetic field. In the limit $\Lambda \gg 1$ this results in large peaks in the acoustic attenuation as a function of magnetic field. These "giant quantum oscillations" have been observed in gallium by Shapira and Lax (1965). This magnetic field tuning of the Fermi surface is analogous to changing the position of the interaction surface in a one dimensional metal by varying the direction of propagation of the acoustic wave. The principal experimental obstacle to observing the anisotropy of the attenuation in one and two dimensional metals is in obtaining a long enough electron mean free path and high enough frequency to achieve the $\Lambda > 1$ limit.

CHAPTER II

Attenuation in Semiconductors

2.1 Quantum Limit

In this chapter the techniques that have already been applied to metals will be used to calculate the acoustic attenuation due to electrons in n-type semiconductors. Both deformation potential and electromagnetic coupling will be considered, and an energy independent scattering time is assumed. This assumption was unnecessary in the previous chapter because in metals only the scattering time for Fermi energy electrons is important.

The first step is to use perturbation theory to calculate the net phonon absorption rate in the quantum regime where $\Lambda \gg 1$. The only difference from the metallic approach is in the definition of the electron distribution function $f(\underline{k})$. For metals $f(\underline{k}) = \left(\exp \left[\left(\epsilon(\underline{k}) - \epsilon_F \right) / kT \right] + 1 \right)^{-1}$ whereas for semiconductors $f(\underline{k}) = \exp \left[\left(\mu - \epsilon(\underline{k}) \right) / kT \right]$ where μ is the chemical potential. In the metal case $\epsilon_F \gg kT$ while for semiconductors $\mu < 0$. If we assume the energy bands to be parabolic, the electron energy may be decomposed into a sum of three parts

$$\epsilon(\underline{k}) = \frac{\hbar^2}{2} \left(\frac{k_x^2}{m_1} + \frac{k_y^2}{m_2} + \frac{k_z^2}{m_3} \right)$$

where m_1 , m_2 and m_3 are effective masses. This decomposition makes it possible to write the attenuation

$$\alpha = \frac{\pi c^2 q}{\rho S^2} \sum_{\underline{k}} \left[f(\underline{k}) - f(\underline{k} + \underline{q}) \right] \delta(\epsilon(\underline{k}) + \hbar\omega - \epsilon(\underline{k} + \underline{q}))$$

as a product of sums

$$[1] \quad \alpha = \frac{\pi c^2 q}{\rho S^2} \sum_{k_x} \left[f(k_x) - f(k_x + q) \right] \delta(\epsilon(k_x) + \hbar\omega - \epsilon(k_x + q)) \\ \times \sum_{k_y} \exp \left[-\epsilon(k_y)/kT \right] \sum_{k_z} \exp \left[-\epsilon(k_z)/kT \right]$$

where $\underline{q} \parallel k_x$. This ability to factorize the electron distribution function means that the attenuation along the principal directions is independent of the dimensionality of the electron gas. The dimensionality only affects the form of the expression for the charge carrier density.

The expression in [1] may be evaluated by converting the summations into integrals in the standard way. In two limiting cases the integrations may be performed explicitly. For $S \ll v_{th}$

$$[2] \quad \alpha_{\ell} = \frac{\sqrt{\pi}}{2} \frac{nm}{\rho S} \left(\frac{c}{kT} \right)^2 q v_{th}$$

and for $S \gg v_{th}$

$$[3] \quad \alpha_{\ell} = 2\sqrt{\pi} \frac{nm}{\rho S} \left(\frac{c}{kT} \right)^2 \left(\frac{S}{v_{th}} \right)^4 \exp \left(-\frac{S^2}{v_{th}^2} \right) q v_{th}$$

where $v_{th} = (2kT/m)^{\frac{1}{2}}$ is the thermal velocity of the electrons. This thermal velocity takes the place in semiconductors of the Fermi velocity in metals. Similarly the important mean free path in semiconductors is $\ell = v_{th}\tau$. At room temperature and using the free electron mass $v_{th} \sim 10^7 \text{ cm/S}$, so that $S/v_{th} \sim 30$. In order for the sound velocity to be of the same order as the thermal electron velocity the temperature must be lowered to about 0.3K. In cases in which the thermal velocity of the electrons is comparable to the speed of sound a numerical integration is required to evaluate the attenuation.

2.2 Transport Equation Approach

In the same way as for metals the Boltzmann transport equation can be used to calculate the acoustic attenuation for arbitrary values of $q\ell$. In what follows the sound wave is assumed to propagate along x which is assumed to be a conducting direction for the one and two dimensional semiconductors. The outstanding difference between the semiconductor and metal results is the lack of dependence on dimensionality in the semiconductor case because of the absence of a Fermi surface.

The first step is to evaluate the transport tensors [4a] and [4c] of Chapter I. The frequency dependent conductivity tensor has two distinct non-zero components for two and three dimensional semiconductors. Only one of these components is zero in one dimension. They are

$$[4] \quad \sigma_{xx} = \frac{\sigma_0}{1 - i\omega\tau} \frac{2}{a^3} \left\{ a - \sqrt{\pi} \exp\left(\frac{1}{a^2}\right) \left[1 - \Phi\left(\frac{1}{a}\right)\right] \right\}$$

$$[5] \quad \sigma_{zz} = \sigma_{yy} = \frac{\sigma_0}{1 - i\omega\tau} \frac{\sqrt{\pi}}{a} \exp\left(\frac{1}{a^2}\right) \left[1 - \Phi\left(\frac{1}{a}\right)\right]$$

where $a = \Lambda(1 - i\omega\tau)^{-1}$ and $\Phi(z)$ is the error function defined by $\Phi(z) = \frac{2}{\sqrt{\pi}} \int_0^z \exp(-t^2) dt$. The expressions for the conductivity are valid for $\omega\tau < 1$ only. Also

$$R_x = \frac{\Lambda^2}{i\omega\tau (1 - i\omega\tau)} \frac{\sigma_{xx}}{2\sigma_0}.$$

If the sound wave couples to the electrons primarily through a self-consistent electromagnetic field the attenuation of longitudinal and transverse waves is found by substituting the above transport tensors into [16a] and [16b] of Chapter I. In the low frequency ($\Lambda \ll 1$) perfect screening limit the attenuation is

$$[6] \quad \alpha_{\ell} = \frac{nm}{\rho S \tau} \Lambda^2$$

for longitudinal waves and

$$\alpha_{\ell} = \frac{1}{2} \frac{nm}{\rho S \tau} \Lambda^2$$

for transverse waves.

The transport equation approach may also be applied in the quantum limit in which $\Lambda \gg 1$. Just as for the one dimensional metal the $\Lambda \rightarrow \infty$ limit must be taken with care in order to avoid losing a small real or imaginary part. The integration is most easily done in rectangular coordinates as follows:

$$\sigma_{xx} = - \frac{e^2 i}{4\pi^3} \int d^3k \frac{v_x^2}{q(v_x - S) - i/\tau} \left(- \frac{\partial f}{\partial \epsilon} \right).$$

Since $(-\partial f/\partial \epsilon)$ can be factored the k_y and k_z integrations are straight forward. The k_x integration is done using

$$\lim_{\tau \rightarrow \infty} \frac{1}{q(v_x - S) - i/\tau} = P \frac{1}{q(v_x - S)} + i\pi \delta(v_x - S).$$

The principal part integral can be done analytically in two limits.

For $S \gg v_{th}$

$$\sigma_{xx} = \frac{\sigma_0}{1 - i\omega\tau} \frac{2}{a} \left[\sqrt{\pi} \frac{S^2}{v_{th}^2} \exp \left(- \frac{S^2}{v_{th}^2} \right) + i \frac{v_{th}}{S} \right]$$

and for $S \ll v_{th}$

$$\sigma_{xx} = \frac{\sigma_0}{1 - i\omega\tau} \frac{2}{a} \left[\sqrt{\pi} \frac{S^2}{v_{th}^2} - i \frac{S}{v_{th}} \right].$$

The σ_{yy} component of the conductivity tensor is needed to calculate the attenuation of transverse waves. It is calculated in a similar way.

For $S \ll v_{th}$

$$\sigma_{yy} = \sigma_{zz} = \frac{\sigma_0}{1 - i\omega\tau} \frac{1}{a} \left[\sqrt{\pi} + i \frac{2S}{v_{th}} \right]$$

and for $S \gg v_{th}$

$$\alpha_{yy} = \alpha_{zz} = \frac{\sigma_0}{1 - i\omega\tau} \frac{1}{a} \left[\sqrt{\pi} \exp \left(-\frac{S^2}{v_{th}^2} \right) + i \frac{v_{th}}{S} \right] \quad .$$

These expressions may be substituted directly into [16a] and [16b] in Chapter I, to find the acoustic attenuation. In the perfect screening limit in the absence of a deformation potential, the attenuation for the different cases is given below. For $S \ll v_{th}$

$$[7] \quad \alpha_{\ell} = \frac{\sqrt{\pi}}{2} \frac{nm}{\rho S} q v_{th}$$

$$\alpha_t = \frac{2}{\pi} \alpha_{\ell}$$

and for $S \gg v_{th}$

$$[8] \quad \alpha_{\ell} = 2\sqrt{\pi} \frac{nm}{\rho S} \frac{S^4}{v_{th}^4} \exp \left(-\frac{S^2}{v_{th}^2} \right) q v_{th}$$

$$\alpha_t = \frac{1}{2} \frac{v_{th}^2}{S^2} \alpha_{\ell} \quad .$$

A comparison of these results ([7] and [8]) with [2] and [3] reveals that in the quantum limit, electromagnetic coupling is equivalent to

a deformation potential equal to kT . This relationship is analogous to the equivalence in metals of electromagnetic coupling to a deformation potential equal to the Fermi energy, as discussed in Chapter I.

In semiconductors the carrier density may be small enough that the screening is incomplete and the electromagnetic coupling ($4\pi ne^2/q^2$) is small compared to deformation potential or piezoelectric coupling. When the deformation potential is the dominant coupling mechanism, the attenuation of longitudinal waves is determined by the last term in eqn. [17] of Chapter I. We consider the quantum limit first. Substituting the appropriate transport tensors calculated above we find for $S \ll v_{th}$

$$[9] \quad \alpha_L = \frac{\sqrt{\pi}}{2} \frac{nm}{\rho S} \left(\frac{C}{kT} \right)^2 \left(1 + (qk)^{-2} \right)^{-2} q v_{th}$$

and for $S \gg v_{th}$

$$[10] \quad \alpha_L = \frac{\sqrt{\pi}}{2} \frac{nm}{S} \left(\frac{C}{kT} \right)^2 \left(1 - \frac{\omega_p^2}{\omega^2} \right)^{-2} \exp \left(- \frac{S^2}{v_{th}^2} \right) q v_{th}$$

where $R = (kT/4\pi ne^2)^{\frac{1}{2}}$ is the Debye-Hückel screening length. The results [9] and [10] above are identical to the expressions [2] and [3] obtained using quantum perturbation theory except that the deformation potential C is replaced by a screened deformation potential. The factors $(1 + (qk)^{-2})$ and $(1 - \omega_p^2/\omega^2)$ are dielectric constants for a classical (non-degenerate) electron gas in the low frequency and high

frequency ($S \gg v_{th}$) limits respectively (Kittel 1963). The expression [9] has been obtained by Spector (1966).

The transport equation method can also be used to calculate the attenuation in the low frequency limit ($\Lambda \ll 1$) when the deformation potential is the dominant coupling mechanism. After expanding the conductivity expression [4] to lowest order in Λ and substituting the expansion into the last term in eqn. [17] of Chapter I we find that

$$[11] \quad \alpha_{\ell} = \frac{nm}{S} \left(\frac{C}{kT} \right)^3 \frac{(qk)^4}{(1 + (qk)^2)^2 + (\omega/\omega_p^2\tau)^2} .$$

The results [9] and [11] above will be rederived in Chapter III below in connection with acoustic amplification in the presence of a d.c. electric field. The relationship between the attenuation of longitudinal waves and transverse waves is discussed in that chapter, along with a description of how the deformation potential results are modified if there is a piezoelectric interaction.

2.3 Metal-Semiconductor Transition

We have just shown that the electronic contribution to the attenuation of a sound wave propagating along a conducting direction in a semiconductor is independent of the dimensionality of the semiconductor. On the other hand in Chapter I above, the attenuation of sound in a one dimensional metal was found to be anomalously small. These results suggest that when a one dimensional conductor undergoes a transition

from a metallic to a semiconducting state (TTF-TCNQ for example) the electronic contribution to the ultrasonic attenuation may increase rather than decrease as might be intuitively expected.

In order to treat the problem of a metal-semiconductor transition it is necessary to drop the assumption of free electron energy bands. In its place we assume a one dimensional band structure consisting of a single half-filled tight-binding band given by

$$[12] \quad \epsilon(k) = -\epsilon_F \cos k b$$

where b is the lattice constant along the conducting direction and $2\epsilon_F$ is the bandwidth. The effect of a metal-semiconductor transition is to open a gap in the middle of the band so that in the semiconducting phase the energy band is given by

$$[13] \quad \epsilon(k) = \pm \sqrt{\epsilon_F^2 \cos^2 kb + \Delta^2(T)}$$

where $2\Delta(T)$ is a temperature dependent electronic energy gap. The + sign applies for $|k| > k_F$ and the - sign for $|k| < k_F$.

It is very difficult to calculate the attenuation in this situation for arbitrary values of Λ . The quantum limit on the other hand is more tractable. We will consider this limit only. The deformation potential coupling C is assumed to be a constant, independent of k and the size of the energy gap, even though it is not clear how good this assumption is, particularly for electronic states close to the gap. As discussed

in the previous chapter, in the extreme quantum limit sound wave attenuation results from electron-phonon scattering processes in which both energy and momentum are strictly conserved. The electronic states allowed by energy and momentum conservation to participate in electron-phonon scattering processes define a surface in k space known as the interaction surface. In a one dimensional metal, when the sound wave propagation is in the conducting direction, the interaction surface is well separated from the Fermi surface. As a result the attenuation is anomalously small. In a metallic tight-binding band there are two distinct interaction surfaces reflecting the fact that the band contains both positive and negative curvature portions. One of the interaction surfaces is near the origin in k space and the other is near the zone boundary, as illustrated in Fig. 12.

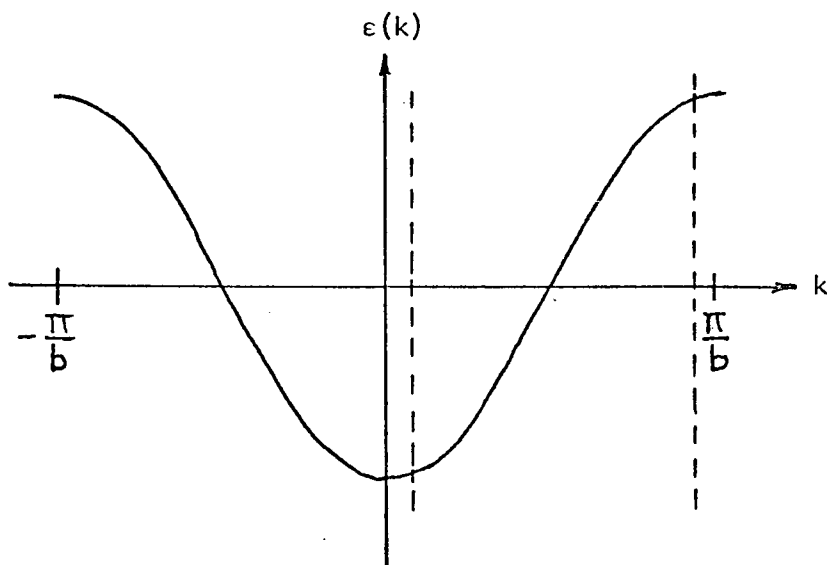


Fig. 12 - Positions of Interaction Surfaces - Metallic Band

If the contribution to the attenuation from both parts of the band are included then

$$[14] \quad \alpha_{\ell} = 2 \frac{nm^*}{\rho S} \left(\frac{C}{\epsilon_F} \right)^2 \frac{\epsilon_F}{kT} \exp \left(- \frac{\epsilon_F}{kT} \right) q v_F$$

according to eqn. [18] of Chapter I. In this expression $m^* = \hbar^2/\epsilon_F b^2$ is the effective mass for an electron near the bottom of the band and $v_F = \epsilon_F b/\hbar$ is the velocity of a Fermi electron. The above expression is similar to the corresponding result [29] given in the previous chapter for a free electron gas.

When an energy gap opens up at the Fermi surface two additional places in the band become available where the energy and momentum selection rules can be satisfied. As illustrated in Fig. 13 these new interaction surfaces are close to the Fermi level (or chemical

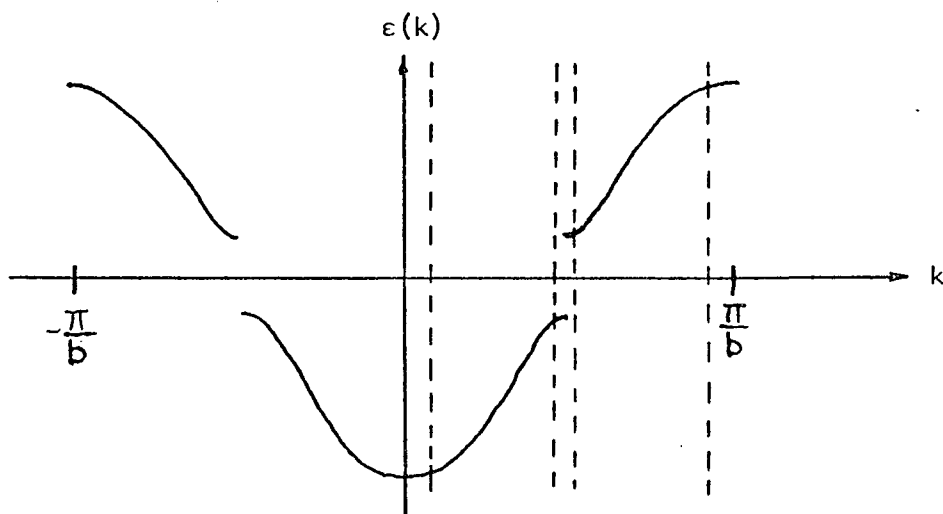


Fig. 13 - Positions of Interaction Surfaces - Semiconducting Band

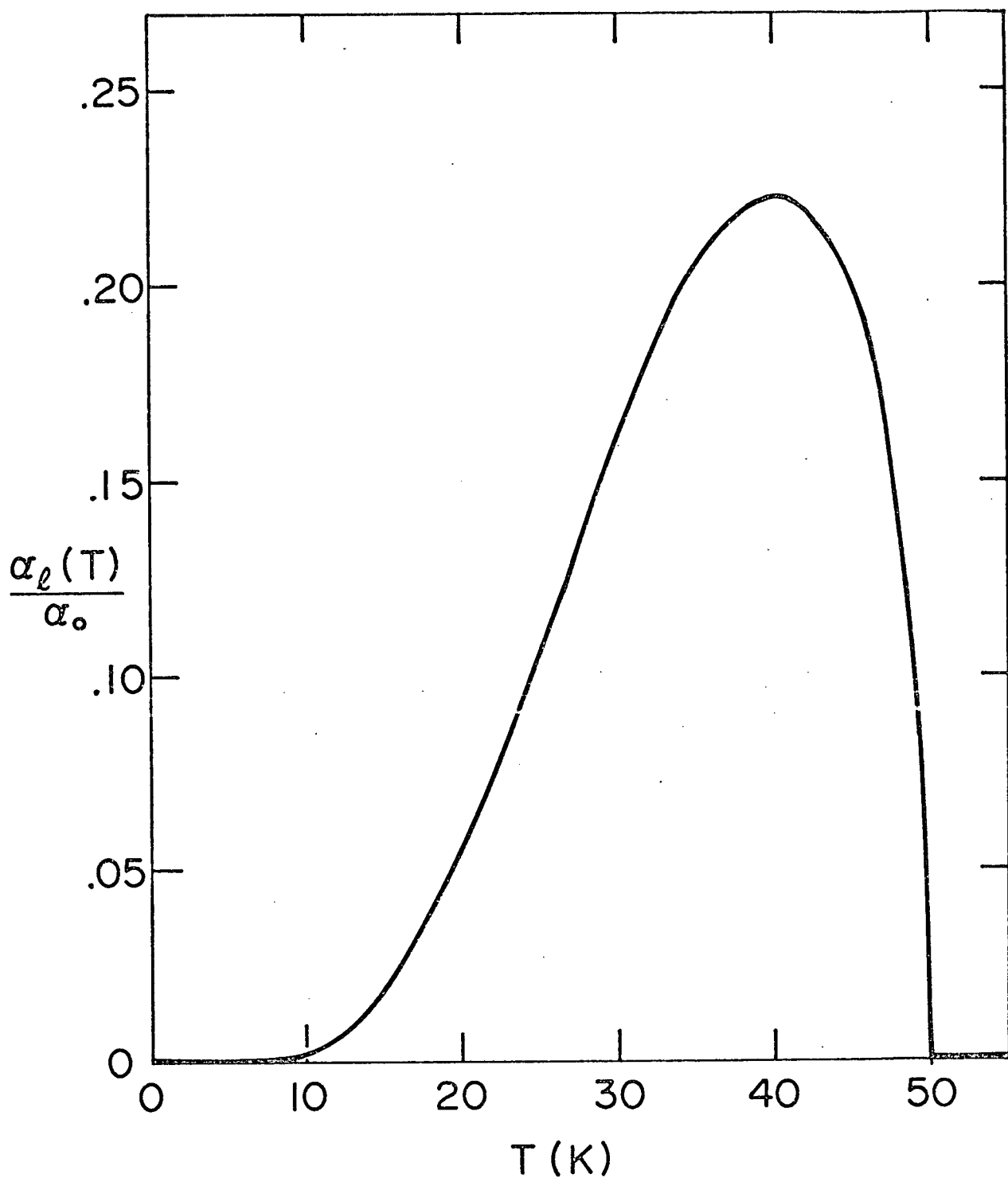


Fig. 14 - Ultrasonic attenuation as a function of temperature near a metal-semiconductor transition in a 1D conductor. The attenuation was calculated from [15] and is normalized to $\alpha_0 = \frac{2nm^*}{\rho S} \left(\frac{c}{\epsilon_F} \right)^2 q v_F$.

potential) if the energy gap is not too large, and hence can provide a significant contribution to the attenuation of sound waves. The attenuation in the semiconducting phase can be calculated by evaluating [18] of Chapter I using [13] for the electronic energy band. The result is

$$[15] \quad \alpha_{\ell}(\Delta) = 2 \frac{nm^*}{\rho S} \left(\frac{C}{\epsilon_F} \right)^2 \left[\frac{\epsilon_F}{kT} \exp \left(- \frac{\epsilon_F}{kT} \right) + \frac{\Delta}{4kT} \operatorname{sech}^2 \left(\frac{\Delta}{kT} \right) \right] q v_F$$

assuming $q \ll k_F$. This time the effective mass $m^* = \hbar^2 \left(1 + \Delta^2 / \epsilon_F^2 \right)^{1/2} / \epsilon_F b^2$. A graph of the temperature dependence of the attenuation predicted by [15] is shown in Fig. 14 for a one dimensional metal which undergoes a metal-semiconductor transition at 50K. The energy gap is assumed to have a BCS-like temperature dependence below the transition temperature.

The attenuation in the metallic phase is extremely small in the collisionless $\omega\tau \gg 1$ limit. If the condition $\omega\tau \gg 1$ is relaxed to $\Lambda \gg 1$, then the attenuation in the metallic phase will be comparable to [31]. Even though the metallic attenuation will now be much larger than in the collisionless regime it will still be small compared to the peak attenuation in the semiconducting phase. On the other hand, the semiconductor phase attenuation is not significantly affected by relaxing the $\omega\tau \gg 1$ condition to $\Lambda \gg 1$, since the interaction surface is already close to the Fermi level, without any collision broadening.

In practice the low frequency $\Lambda \ll 1$ limit is much more likely to be physically realizeable than the quantum limit, particularly in a material such as TTF-TCNQ where the electron mean free path is only a few lattice

constants. From earlier work in Chapter I we expect the electromagnetic coupling mechanism to be far larger than the deformation potential coupling at low frequencies. In this case the metallic attenuation is very low so that one might also expect to see an increase in the low frequency attenuation, to something approaching the three dimensional value, in going from the metal to the semiconductor.

CHAPTER III

A m p l i f i c a t i o n

3.1 Introduction

It is well known that under certain circumstances ultrasonic waves may be amplified in metals or semiconductors if the conduction electrons have a d.c. drift velocity (Hutson, McFee and White 1961, Vrba and Haering 1973). The amplification of sound waves may be regarded as a negative attenuation that can occur in the presence of a d.c. electric field. Accordingly the methods described in Chapter I for calculating the attenuation may be applied to the amplification problem. In general the attenuation and hence the amplification of sound waves by electrons depends on the relation between the electron mean free path ℓ and the sound wavelength $2\pi/q$. The theory of acoustic amplification in the presence of a d.c. electric field has been worked out by Weinreich (1956) and White (1962) for the low frequency ($q\ell \ll 1$) limit and by Pippard (1963) for the high frequency limit ($q\ell \gg 1$). Spector (1962) has used the Boltzmann equation to produce a theory that is valid for arbitrary $q\ell$.

The Spector (1962) theory is very complex for the following reason. When a d.c. electric field is introduced into the transport treatment of ultrasonic attenuation a large number of additional terms of equal order are generated, none of which can be neglected. In this chapter we outline a theory where the d.c. electric field is taken into account by shifting the distribution function in k space. This approach eliminates the need to deal with a large number of new terms arising

from the d.c. field, and vastly simplifies the problem. Using the new approach, we are able to confirm Spector's results which have never been verified previously. In addition our approach is valid for strong d.c. electric fields in the same way that the method of Spector (1968) is valid for strong fields.

In this chapter we calculate the attenuation (amplification) of sound waves in n-type semiconductors and three dimensional nearly-free-electron metals, in the presence of a d.c. electric field. The calculation follows the transport equation approach developed in Chapter I. In both the metal and semiconductor the conduction electrons are modelled by a free electron gas and non-electronic contributions to the attenuation are ignored. In the metal a self-consistent electric field is used to couple the sound wave to the conduction electrons. In the semiconductor a deformation potential tensor is assumed to be the dominant coupling mechanism. First, the problem will be set up for arbitrary electron statistics and both self-consistent field and deformation potential coupling.

3.2 Transport Equation

In the presence of a sound wave described by a local lattice velocity $\underline{u} \propto \exp[i(qx - \omega t)]$, the Boltzmann transport equation for electrons is

$$[1] \quad \frac{\partial f}{\partial t} + \underline{v} \cdot \nabla_r f - \frac{e}{m} \left(\underline{E}_1 + \frac{qq \cdot \underline{C} \cdot \underline{u}}{ei\omega} \right) \cdot \underline{\nabla} f = - \left(\frac{f - \bar{f}}{\tau} \right)$$

where f is the electron distribution function, \underline{E}_1 is a self-consistent electric field and \underline{C} is a deformation potential tensor.

In the relaxation time approximation used here scattering processes cause the electron distribution function to relax to the local equilibrium distribution function \bar{f} . As in Chapter I, Section 1.2, \bar{f} can be approximated by

$$[2] \quad \bar{f}(\underline{v}, \underline{r}, t) = f_0(\underline{v} - \underline{u}; \mu(\underline{r}, t)) \\ \approx f_0 - \frac{\partial f_0}{\partial \epsilon} \left(m \underline{v} \cdot \underline{u} + \frac{2\epsilon_F}{3n} n_1 \right)$$

where f_0 is the equilibrium electron distribution function in the absence of a sound wave, μ is a self-consistent chemical potential, ϵ_F is the electron Fermi energy, n is the equilibrium electron number density and n_1 is a small oscillatory component of the electron density.

A d.c. electric field will be introduced into eqn.[1] by postulating that the sole effect of the field is to shift the equilibrium electron distribution by the average drift velocity $\underline{v}_d = -\frac{e\tau}{m} \underline{E}_0$ where \underline{E}_0 is the d.c. field. This assumption is correct to first order in the electric field. In this approximation, the d.c. field may be introduced by redefining the local equilibrium distribution function \bar{f} by

$$[3] \quad \bar{f}(\underline{v}, \underline{r}, t) \approx f_0^d - \frac{\partial f_0^d}{\partial \epsilon} \left(m(\underline{v} - \underline{v}_d) \cdot \underline{u} + \frac{2}{3} \frac{\epsilon_F}{n} n_1 \right)$$

for a three dimensional metal where

$$f_0^d(\underline{v}) = f_0(\underline{v} - \underline{v}_d)$$

is a doppler shifted equilibrium distribution function.

The Boltzmann equation [1] with \bar{f} defined by [3] may now be solved to first order by substituting

$$f = f_0 + f_1^0 + f_1^1$$

where f_1^0 is the d.c. part of the perturbation from equilibrium, and $f_1^1 \propto \exp[i(qx - \omega t)]$ is the a.c. part of the distribution function.

We find that

$$f_1^0 = f_1^d - f_0$$

and

$$[4] \quad f_1^1 = \frac{\partial f_0^d}{\partial \varepsilon} \left[e\tau \left(\underline{E}_1 + \frac{qq \cdot \underline{C} \cdot \underline{u}}{ei\omega} - \frac{m\underline{u}}{e\tau} \right) \cdot \left(\underline{v} - \underline{v}_d \right) - \frac{2}{3} \frac{\varepsilon_F}{n} n_1 \right] (1 - i\omega\tau + iqv\tau)^{-1}.$$

The electronic contribution to the a.c. current is given by

$$[5] \quad \underline{J}_e = - \frac{2e}{(2\pi)^3} \int \underline{v} f_1^1 d^3k.$$

Now define a doppler shifted a.c. component to the distribution function by

$$f_1^d = \frac{e\tau \left(\underline{E}_1 + \frac{qq \cdot \underline{C} \cdot \underline{u}}{ei\omega} - \frac{m\underline{u}}{e\tau} \right) \cdot \underline{v} - \frac{2}{3} \frac{\varepsilon_F}{n} n_1}{(1 - i(\omega - \omega_d)\tau + iqv\tau)} \frac{\partial f_0}{\partial \varepsilon}$$

where

$$\omega_d = q \cdot \underline{v}_d.$$

Then the current expression [5] may be rewritten as

$$\underline{J}_e = \underline{J}_e^d - n_1 e \underline{v}_d$$

where

$$[6] \quad \underline{J}_e^d = \underline{\sigma}^d \left(\underline{E}_1 + \frac{q \underline{q} \cdot \underline{C} \cdot \underline{u}}{e i \omega} - \frac{m \underline{u}}{e \tau} \right) - n_1 e s^d \underline{R}^d$$

and

$$n_1 = \frac{2}{(2\pi)^3} \int d^3 k f_1^1 = \frac{2}{(2\pi)^3} \int d^3 k f_1^d$$

$$\underline{\sigma}^d = \frac{2e^2 \tau}{(2\pi)^3} \int d^3 k \frac{\underline{v} \underline{v}}{1 - i(\omega - \omega_d) \tau + i q v \tau} \left(- \frac{\partial f_o}{\partial \epsilon} \right)$$

$$\underline{R}^d = \frac{\epsilon_F}{6\pi^3 n s^d} \int d^3 k \frac{\underline{v}}{1 - i(\omega - \omega_d) \tau + i q v \tau} \left(- \frac{\partial f_o}{\partial \epsilon} \right)$$

and $s^d = (\omega - \omega_d)/q$ is the doppler shifted sound phase velocity.

The total a.c. current density due to the sound wave is the sum of the electronic current and the background ion current. Thus

$$[7] \quad \underline{J} = \underline{J}_e + n e \underline{u}$$

where \underline{J} is the total current, and n is the ion number density. In a monovalent metal (n-type semiconductor) the ion (ionized impurity) number density will equal the equilibrium electron number density. In the presence of a sound wave the ion number density will contain a small oscillatory component given by nu/S where u/S is the strain induced by the sound wave. The oscillatory term in the electron

number density may be found by using the continuity equation for electrons

$$\omega n_1 e + \underline{q} \cdot \underline{J}_e = 0.$$

This equation can also be written in terms of the doppler shifted quantities

$$(\omega - \omega_d) n_1 e + \underline{q} \cdot \underline{J}_e^d = 0$$

or

$$[9] \quad n_1 e S^d = - J_{e\parallel}^d$$

where $J_{e\parallel}^d$ is the component of \underline{J}_e^d parallel to \underline{q} . Also the electric field which is consistent with the total current \underline{J} may be found from Maxwell's equations to be

$$[10a] \quad E_{\parallel} = - \frac{4\pi i}{\omega} (J_{e\parallel} + n e u_{\parallel})$$

and

$$[10b] \quad E_{\perp} = \frac{4\pi i}{\omega} \frac{\left(\frac{S}{c}\right)^2}{1 - \left(\frac{S}{c}\right)^2} (J_{e\perp} + n e u_{\perp})$$

$$\approx \frac{4\pi i}{\omega} \left(\frac{S}{c}\right)^2 (J_{e\perp} + n e u_{\perp}).$$

The next step in obtaining the net power flow from the sound wave to the electron gas is to obtain expressions for the self-consistent electric field and current in terms of the local lattice velocity. For a free electron gas, and a sound wavevector \underline{q} in the x direction, the conductivity tensor is diagonal. In this case the vector notation

may be dropped and the components can be treated independently.
For longitudinal waves ($\underline{q} \parallel \underline{u}$) eqn.[9] can be used to eliminate n_1 from [6]. Thus

$$[11] \quad J_{ex}^d = \sigma_x^{1d} \left(E_{1x} + \frac{q^2 C_{xx} u_x}{e i \omega} - \frac{m u_x}{e \tau} \right)$$

where $\sigma_x^{1d} = \sigma_x^d / (1 - R_x^d)$. Only the x components of \underline{E}_1 and \underline{u} are non-zero for longitudinal waves. Substitute [10a] for E_x then

$$[12] \quad J_{ex}^d = - \frac{n e u_x}{\epsilon_x^{1d}} \left[\frac{\sigma_x^{1d}}{\sigma_0} + \frac{4\pi i}{\omega} \sigma_x^{1d} (1 + D_{xx}) \right]$$

where $\epsilon_x^{1d} = 1 + \frac{4\pi i}{\omega \gamma} \sigma_x^{1d}$ is a dielectric constant, $\gamma = 1 - \frac{\underline{q} \cdot \underline{v}_d}{\omega}$,

$\sigma_0 = \frac{n e^2 \tau}{m}$ and $D_{xx} = \frac{q^2 C_{xx}}{4\pi n e^2}$. Also if [12] is substituted into [11] we find the following expression for the total driving field felt by the electrons:

$$[13] \quad E_{1x} + \frac{q^2 C_{xx} u_x}{e i \omega} = - \frac{n e u_x}{\epsilon_x^{1d}} \frac{4\pi i}{\omega} \left[1 + D_{xx} - \frac{\sigma_x^{1d}}{\gamma \sigma_0} \right].$$

The self-consistent electric field and current associated with a transverse sound wave may be found in exactly the same way. When a transverse wave is polarized in the y direction and propagates in the x direction there are electric currents in both the x and y directions. Using the electron continuity equation and [6], we find that the doppler shifted current in the x direction is,

$$[14] \quad J_{ex}^d = \sigma_x^{1d} \left(E_{1x} + \frac{q^2 C_{xy} u_y}{e i \omega} \right).$$

If the current and electric field are required to satisfy the Maxwell equation [10a] which in this case reduces to

$$[15] \quad E_{1x} = - \frac{4\pi i}{\omega} J_{ex}$$

then the total current in the x direction is

$$[16] \quad J_{ex} = \frac{\sigma_x^{1d}}{\epsilon_x^{1d}} \left(\frac{q^2 C_{xy} u_y}{e i \omega \gamma} \right).$$

Similarly, the self-consistent current in the y direction is,

$$[17] \quad J_{ey} = \sigma_y^d \left(E_{1y} - \frac{m u_y}{e \tau} \right) + \frac{v_{dy}}{S} J_{ex}$$

where v_{dy} is the y component of the electron drift velocity \underline{v}_d , and J_{ex} is given by [16]. By using the self-consistency requirement [10b] we find that

$$[18] \quad J_{ey} = \frac{n e u_y}{\epsilon_y^t} \left(\frac{4\pi i}{\omega} \left(\frac{S}{c} \right)^2 \sigma_y^d - \frac{\sigma_y^d}{\sigma_o} \right) + \frac{v_{dy} J_{ex}}{S \epsilon_y^t}$$

where $\epsilon_y^t = 1 - \frac{4\pi i}{\omega} \left(\frac{S}{c} \right)^2 \sigma_y^d$. The electric field is found by substituting [18] back into [17]. Thus

$$[19] \quad E_{1y} = \frac{4\pi i}{\omega \epsilon_y^t} \left(\frac{S}{c} \right)^2 \left[n e u_y \left(1 - \frac{\sigma_y^d}{\sigma_o} \right) + \frac{v_{dy}}{S} J_{ex} \right].$$

We are now ready to evaluate the energy transfer between the sound wave and the electron gas.

3.3 Energy Transfer

The power transferred from the sound wave to the electrons is

$$[20] \quad P = \frac{1}{2} \operatorname{Re} \left[\frac{\underline{J}_e^*}{-e} \cdot \left(\underline{E}_1 + \frac{q \underline{q} \cdot \underline{C} \cdot \underline{u}}{e i \omega} \right) + \frac{m \underline{u}^*}{e \tau} \cdot \left(\frac{\underline{J}}{-e} + n e \underline{u} \right) \right].$$

The first term is the work done per unit time by the self-consistent electric field and deformation potential gradient on the electrons.

The second term in [20] is due to the interaction of the lattice wave with the electrons through collisions (see Chapter 1) and is important only for high frequencies ($\omega \sim \sigma_x^1$). Notice that all d.c. fields and currents have been omitted from [20]. In the linear approximation considered here, d.c. quantities contribute terms in the power expression which either have a zero time average or represent the ohmic losses associated with the drifting electron distribution. The attenuation (amplification) factor for ultrasonic waves is obtained from [20] by dividing by the acoustic energy flux. Thus

$$\alpha = P / \left(\frac{1}{2} \rho |\underline{u}|^2 \right)$$

where α is the attenuation.

Rather than evaluating the attenuation with both self-consistent field and deformation potential coupling, we consider two limiting cases. In the first limit, the deformation potential is assumed to be negligible compared with the comparable electromagnetic coupling energy $\frac{4\pi n e^2}{q^2}$. This assumption is valid up to high frequencies

(~ 10 GHz) in metals. In the second limiting case the deformation potential is assumed to be much greater than $\frac{4\pi ne^2}{q^2}$ and hence is the dominant coupling mechanism. This is a good assumption at high frequency in semiconductors.

First we consider longitudinal waves in metals and neglect the deformation potential. The attenuation of longitudinal waves is found by substituting [10a] and [13] into [20]. If the deformation potential is set equal to zero and $\epsilon_o = 1 + \frac{4\pi i}{\omega} \sigma_o$, then

$$[21] \quad \alpha_{\ell} = \frac{nm}{\rho S \tau} \operatorname{Re} \left[\frac{\epsilon_o}{\epsilon_x^{ld}} \left(1 - \frac{\sigma_x^{ld}}{\gamma \sigma_o} \right) \right].$$

This expression should be compared with [16a] in Section 1.2, the analogous expression in the absence of a d.c. field. The attenuation may be evaluated by substituting the appropriate transport tensors given in Section 1.4, into [21]. For a three dimensional metal to the lowest order in S/v_F , for $\omega \ll \sigma_x^1$ and $\Lambda = q\ell$, the result is

$$[22] \quad \alpha_{\ell} = \frac{nm}{\rho S \tau} \left[\frac{\Lambda^2 \tan^{-1} \Lambda}{3(\Lambda - \tan^{-1} \Lambda)} (1 - \mu) - 1 \right]$$

for arbitrary Λ , where $\mu = \underline{q} \cdot \underline{v}_d / \omega$. For $\Lambda \ll 1$ eqn.[22] reduces to

$$\alpha_{\ell} = \frac{nm}{\rho S \tau} \left[-\mu + \frac{4}{15} \Lambda^2 (1 - \mu) \right]$$

and for $\Lambda \gg 1$

$$\alpha_{\ell} = \frac{nm}{\rho S \tau} \frac{\pi}{6} \Lambda (1 - \mu).$$

Similarly, by substituting the transport tensors for the one and two dimensional metals from Section 1.4 into eqn.[21], one obtains the attenuation for the lower dimensionality metals in a d.c. electric field. The results are summarized in Table II for arbitrary Λ in the $\omega \ll \sigma_x^1$ limit. The three dimensional result [22] is identical with the expressions obtained by Spector (1962), in the appropriate limits.

TABLE II

Attenuation in 1, 2 and 3 Dimensional Metals in a D.C. Electric Field

$\left(\frac{nm}{\rho S \tau} \text{ units} \right)$

1D	2D	3D
$-\mu$	$\frac{\Lambda^2 (1 - \mu)}{2(\sqrt{1 + \Lambda^2} - 1)} - 1$	$\frac{\Lambda^2 \tan^{-1} \Lambda (1 - \mu)}{3(\Lambda - \tan^{-1} \Lambda)} - 1$

In the absence of a deformation potential, the d.c. electric field has no significant effect on the attenuation of transverse waves. To show this, substitute [17] and [18] into [20], then

$$\alpha_t = \frac{nm}{\rho S \tau} \operatorname{Re} \left[\frac{\epsilon_o^t}{\epsilon_y^t} \left(1 - \frac{\sigma_y^d}{\sigma_o} \right) \right]$$

where $\epsilon_o^t = 1 - \frac{4\pi i}{\omega} \left(\frac{S}{c} \right)^2 \sigma_o$. To lowest order in S/v_F the attenuation is the same as in the zero field case discussed in Section 1.4.

In conventional metals μ must be very small compared with one in order to avoid unrealistically large ohmic power dissipation. There-

fore, it follows from [22] that unless $\mu > 1$ can be achieved, acoustic amplification through interaction with a d.c. field is impractical in metals, except possibly at low frequencies ($\Lambda \ll 1$). However, in this case there is an additional complication. In the low frequency limit in the presence of a large d.c. field the attenuation becomes sensitive to a second order term in \underline{J}_e such as the acoustoelectric current (Mikoshiba, 1959). For example if $\mu \sim 1$ then the self-consistent field $E_1 \sim (u/S) \Lambda^2 E_0$. Since the strain $u/S \lesssim 10^{-5}$ and $\Lambda \ll 1$, the self-consistent electric field will be much smaller than the d.c. electric field E_0 . The large d.c. field coupled with a small second order d.c. term in \underline{J}_e could give rise to a significant contribution to the attenuation, not included in [22].

For maximum acoustic gain one would like a material with a large electron-sound wave coupling, high mobility carriers, and a relatively low carrier density to limit the ohmic losses. These characteristics are available in some semiconductors.

In non-piezoelectric semiconductors we expect the deformation potential to be the most important coupling mechanism between the electrons and the sound wave. For deformation potential coupling the attenuation of longitudinal waves is found by substituting [13] into [20] and assuming

$$D_{xx} = \frac{q^2 C_{xx}}{4\pi n e^2} \gg 1. \quad \text{Thus}$$

$$[23] \quad \alpha_L = \frac{nm}{\rho S \tau} D_{xx}^2 \operatorname{Re} \left[\frac{\epsilon_0 - 1}{\gamma \epsilon_x^{ld}} \right].$$

In order to evaluate this expression one needs to know the transport tensor components σ_x^d and R_x^d , which are defined by the integrals following [6]. After doing the integrations with Boltzmann statistics for the electrons as in Section 2.2, we find that in the limit $\omega\gamma\tau < 1$

$$[24] \quad \sigma_x^d = \frac{\sigma_0}{1 - i\omega\gamma\tau} \frac{2}{a^2} \left[a - \sqrt{\pi} \exp\left(\frac{1}{a^2}\right) \left\{ 1 - \Phi\left(\frac{1}{a}\right) \right\} \right]$$

where $a = q\ell/(1 - i\omega\gamma\tau)$ and the mean free path ℓ is defined in terms of a thermal velocity as $\ell = (2kT/m)^{\frac{1}{2}}\tau$, and

$$\Phi(x) = \frac{2}{\sqrt{\pi}} \int_x^\infty \exp(-t^2) dt.$$

In the quantum limit in which $q\ell, \omega\tau \gg 1$, the conductivity is

$$[25] \quad \sigma_x^d = \frac{2\sigma_0}{q\ell} \left[\sqrt{\pi} \left(\frac{S^d}{v_{th}} \right)^2 - i \frac{S^d}{v_{th}} \right]$$

where $v_{th} = (kT/M)^{\frac{1}{2}}$ and $v_{th} \gg S$ has been assumed. In most semiconductors the thermal velocity of the electrons v_{th} is much larger than the speed of sound S for temperatures above liquid helium temperature. The x component of the diffusion vector \underline{R}^d is related to the conductivity by

$$[26] \quad R_x^d = \frac{q\ell^2}{i\omega\gamma\tau(1 - \omega\gamma\tau)} \frac{\sigma_x^d}{2\sigma_0}$$

and the other components of \underline{R}^d are zero. The attenuation of longitudinal waves can now be evaluated in the low frequency limit ($q\ell \ll 1$) and in the quantum limit ($q\ell \gg 1$) by substituting [24] and [25] respectively into [23] and [26]. In the $q\ell \ll 1$ limit

$$[27] \quad \alpha_{\ell} = \frac{nm}{\rho S \tau} \left(\frac{C_{xx}}{kT} \right)^2 \frac{(qR)^4 (1 - \mu)}{\left(1 + (qR)^2 \right)^2 + \left(\frac{\omega}{\omega_p^2 \tau} \right)^2 (1 - \mu)^2}$$

where $R = [kT/(4\pi ne^2)]^{\frac{1}{2}}$ is the Debye-Hückel screening length and $\omega_p = (4\pi ne^2/m)^{\frac{1}{2}}$ is the plasma frequency. Similarly in the $q\ell \gg 1$ limit

$$[28] \quad \alpha_{\ell} = \frac{\sqrt{\pi}}{2} \frac{nm}{\rho S \tau} \left(\frac{C_{xx}}{kT} \right)^2 \frac{q\ell (1 - \mu)}{(1 + (qR)^{-2})^2}$$

for $S \ll v_{th}$.

The above procedure will now be applied to transverse waves in semiconductors. The attenuation of transverse waves is found by substituting the current expressions [16] and [18] and the electric field expressions [15] and [19] into the power equation [20]. In the case $D_{xy} \gg 1$, the current and field parallel to the propagation direction give the important contribution to the attenuation. The attenuation is given by

$$[29] \quad \alpha_t = \frac{nm}{\rho S \tau} D_{xy}^2 \operatorname{Re} \left[\frac{\epsilon_o - 1}{\gamma \epsilon_x^{1d}} \right].$$

A comparison of this result with the corresponding result for longitudinal waves, [23], reveals that the two are identical except that the diagonal component C_{xx} of the deformation potential tensor is replaced by the off diagonal component C_{xy} . Accordingly the $q\ell \ll 1$

and $q\ell \gg 1$ limits given in [27] and [28] respectively, also apply to transverse waves provided that C_{xx} is replaced by C_{xy} .

Although the preceding attenuation expressions have been derived assuming deformation potential electron-sound wave coupling, they may be readily modified to include a piezoelectric coupling constant. In piezoelectric materials such as CdS where the piezoelectric interaction is much larger than the deformation potential interaction at all attainable frequencies, the deformation potential factor qC_{xy} can be replaced by ed_{xy} , where d_{xy} is the piezoelectric constant. When this replacement is made the expression for the attenuation in the low frequency limit [27] reduces to that obtained by White (1962) using a different method. Note that in the regime in which the deformation potential (or piezoelectric) coupling is dominant, ultrasonic waves are amplified when the electron drift velocity in the direction of the sound propagation is greater than the sound phase velocity. This amplification has been observed in CdS (Vrba and Haering, 1973) and the measured acoustic gain is consistent with eqn.[27] (Hughes, 1975).

3.4 Conclusion

To summarize, we have outlined a transport equation approach to the problem of acoustic amplification in a d.c. electric field, that is much less complex than any that is currently available (Spector 1962, 1968). The new treatment duplicates the results of the earlier work and is simple enough to be readily generalized to apply to one and two dimensional metals. Furthermore the method is not restricted to

metals and can be easily applied to semiconductors, unlike the earlier treatment. In our calculation there is no need to make any special assumptions about the direction of the d.c. drift field.

P A R T B

MEASUREMENTS ON TTF-TCNQ

CHAPTER I

Experimental Method

1.1 Capacitive Measurement Technique

Capacitive transducers have been widely used for exciting and detecting small amplitude vibrations (Barmatz and Chen 1974, Cantrell and Breazeale 1977, McGuigan et al 1977). The two main reasons for the popularity of capacitive transducers are their practical simplicity and high sensitivity to small displacements. In the conventional capacitive displacement detector, a large d.c. bias voltage is applied between the test object and a nearby electrode. Oscillations in the position of the test object will modulate the capacitance between the test object and the electrode and cause a current to flow in a large series resistor. The voltage signal on the resistor becomes progressively smaller and harder to measure as the frequency of oscillation of the test object is lowered and the pickup capacitance decreases. In this paper we describe an alternative capacitive detection scheme which does not significantly lose sensitivity at low frequencies and low capacitance values.

The new approach to the capacitive vibration pickup was designed to make accurate sound velocity and absorption measurements in single crystals of TTF-TCNQ. A capacitive technique was chosen to avoid having to make good low loss acoustic bonds to the small and somewhat irregular TTF-TCNQ crystals. In order to be able to see longitudinal modes in the elongated TTF-TCNQ platelets, the pickup transducer must

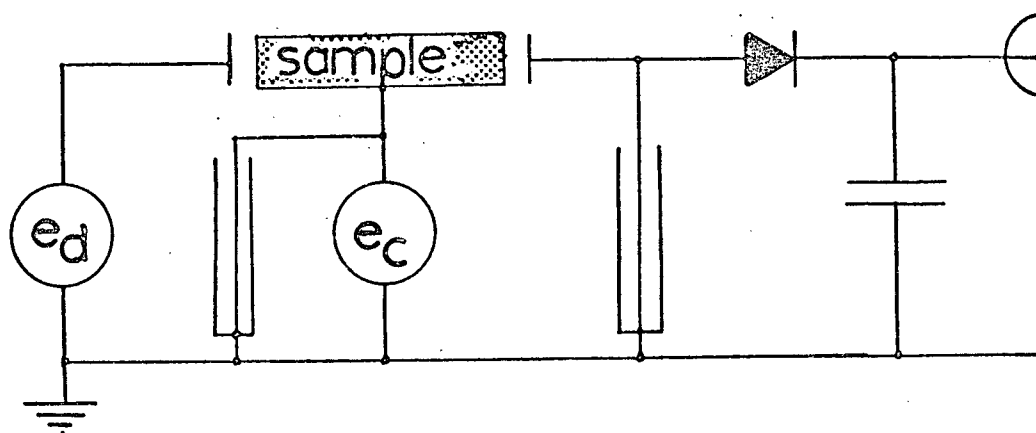


Fig. 15 - Drive and detection circuit

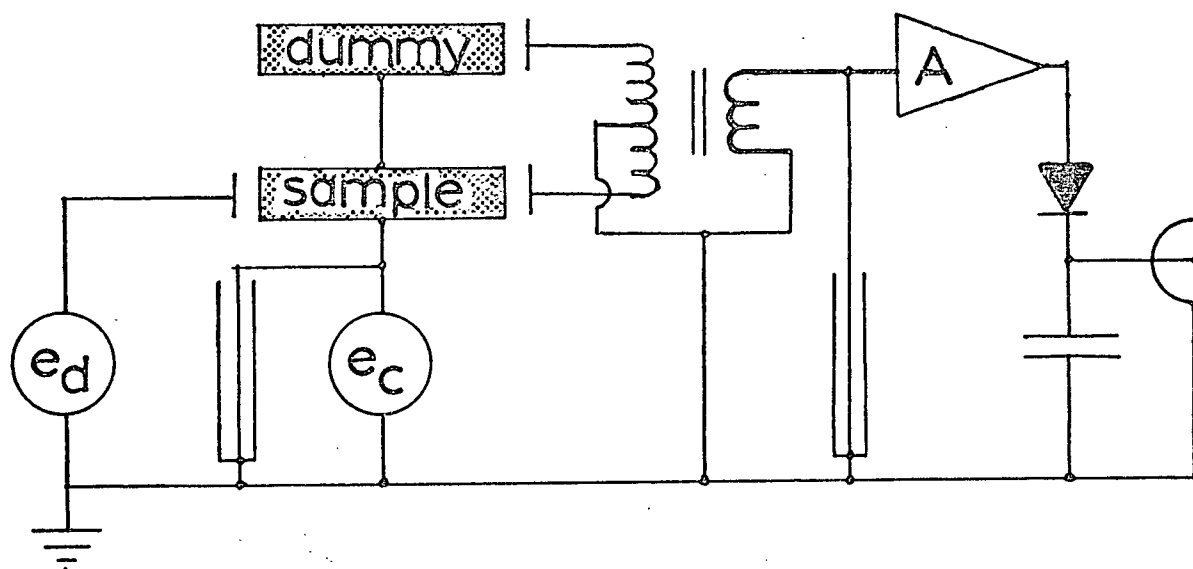


Fig. 16 - Drive and bridge detector circuit

operate effectively with a total capacitance of less than 0.1 pf. In the remainder of this section we describe the new capacitive displacement measuring technique, and the electrostatic vibration excitation scheme.

(i) Electronics

Acoustic resonances were excited in the samples electrostatically by relying on the force between the plates of a charged capacitor. As shown schematically in Fig. 15 the left hand end of the sample forms one side of the capacitor and a nearby electrode forms the other side. When this capacitor is driven by the oscillator shown as e_d in Fig. 15, there is a periodic force on the sample. This oscillator - a frequency synthesizer - is operated in the frequency range 0-10 MHz. To increase the force on the sample the synthesizer output voltage is stepped up by a factor of four to a maximum of 110 V peak-to-peak by a Vari-L, LF-452 wideband transformer. To further increase the driving force and to reduce the relative importance of the second harmonic component of the driving force, a d.c. bias of up to 400 V can be superimposed on the a.c. signal across the drive capacitor.

The vibration of the sample is detected by using an rf carrier signal to measure changes in a pickup capacitance. In the simplest case of a parallel plate capacitor, the capacitance will be inversely proportional to the distance between the sample and the pickup electrode. When the sample moves the detector capacitance will change leading to

a corresponding change in its impedance. This impedance variation may be detected using the circuit shown schematically in Fig. 15. The carrier signal generator marked e_c in Fig. 15 operates in the frequency band 300-1000 MHz, and its output is connected to the sample. When the sample vibrates, the varying impedance of the pickup capacitor, amplitude modulates the rf signal flowing through it. The amplitude modulation on the carrier is recovered by a Schottky barrier diode detector and low pass filter (see Appendix § 1.(i) for circuit diagram). Hence any displacement of the sample is reflected in the diode output voltage.

Although this simple detection scheme is adequate for many purposes, the sensitivity can be improved by using a bridge circuit as shown schematically in Fig. 16. In this circuit the rf signal transmitted through the sample pickup capacitor is compared with the signal through a stationary dummy capacitor. If the sample and dummy capacitances are equal the output from the balanced/unbalanced wideband transformer (Vari-L, HF-122) will be zero. Of course the inductive and resistive components of the impedance in the two arms must also be equal for a null output. In principle a tuned transformer would give better sensitivity, however, a wideband transformer was used in the TTF-TCNQ measurements because it is more convenient when dealing with a variety of samples of different size and shape. The output of the transformer is followed by a low noise UHF amplifier (Avantek, AMM-1010) and then by a diode detector.

The bridge improves the sensitivity of the detector for two main

reasons. The first reason is that the rf signal generator noise is cancelled out when the bridge is balanced, since this noise is the same in both arms. Secondly the signal is a small deviation from a null whereas without the bridge the signal is a small ripple on top of a large rf carrier. Since the bridge output signal is small it may be amplified in a low noise rf amplifier before detection. This preliminary amplification reduces the importance of diode noise.

The close proximity of the detector electrode to the drive electrode, particularly for small samples, can lead to problems with electrical pickup. Even though both electrodes are shielded there is a substantial direct capacitive pickup from the drive electrode to the detector electrode. This spurious pickup can cause problems; however, it may be filtered out with a shorted section of coaxial cable as shown schematically in Figs. 15 and 16. The length of the coaxial cable is chosen so that it is a quarter wavelength long at the frequency of the rf carrier. The quarter wave short acts as an open circuit at the carrier frequency and as a short circuit at the lower drive frequency. If a quarter wave short is connected to the bridge output, the direct pickup is eliminated before it can cause problems. A similar coaxial short at the output of the rf generator prevents any backflow of the drive signal into the rf oscillator.

As described above, when the drive oscillator is turned on the sample will vibrate and generate a signal that is proportional to the vibration amplitude at the output of the diode detector. This signal is detected using a heterodyne detection scheme, outlined in the block diagram in

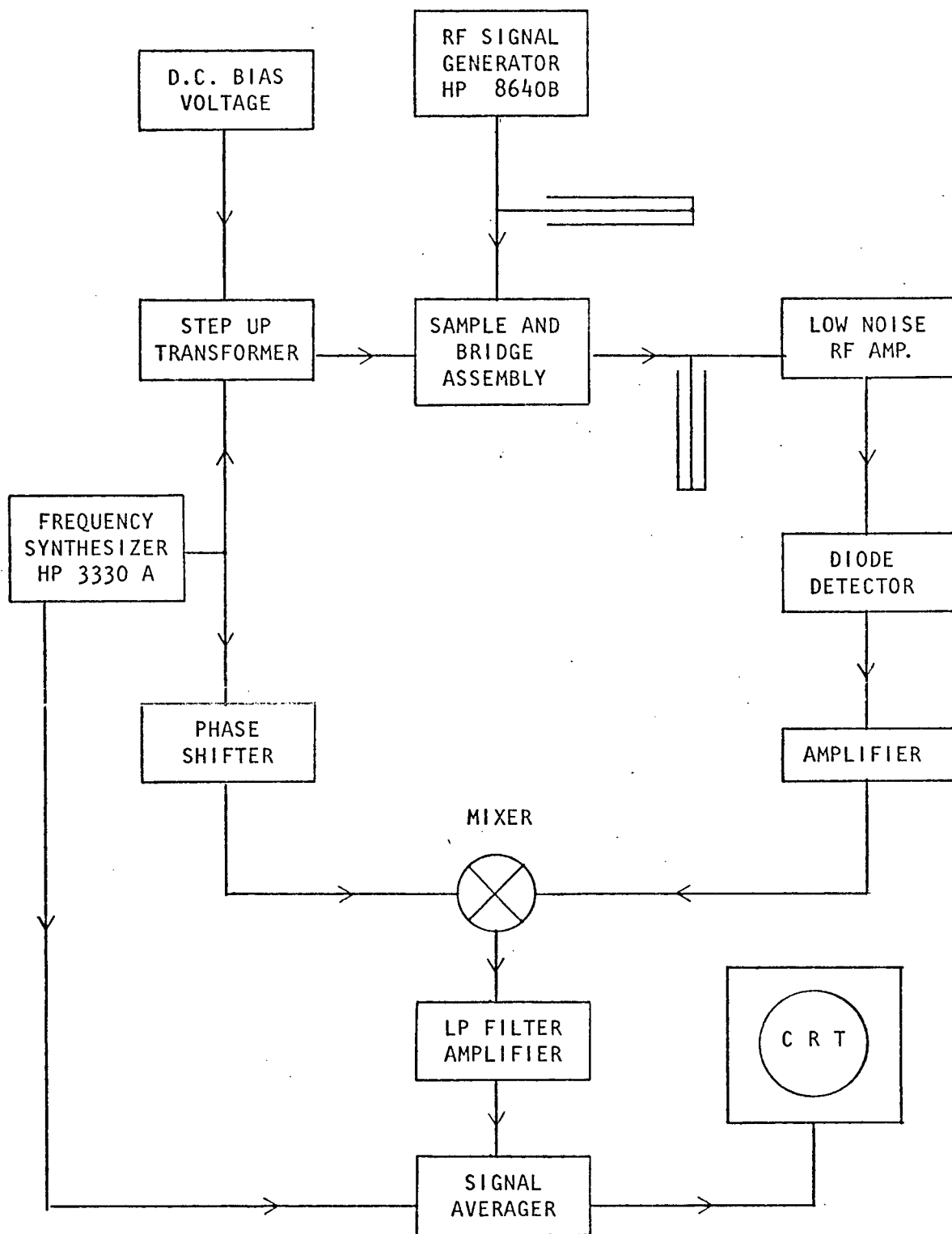


Fig. 17 - Block Diagram of Electronic Equipment

Fig. 17, which we now describe in detail. The first step is to amplify the diode output by about 40 db using a PAR 114 (plug-in 119) low noise preamp. The PAR preamp is used when the drive frequency is in the range 100 Hz to 1 MHz. For drive frequencies between 1 MHz and 10 MHz a MOSFET amplifier (see Appendix § 1.(ii) for circuit diagram) was used, followed by Avantek wideband amplifiers UA 105 and UA 106. The total gain for this combination was also about 40 db.

The amplified signal then goes into a double balanced mixer (Minicircuits ZAD-6) together with a reference signal from the drive oscillator. Since the reference signal and the signal coming from the vibrating sample are normally at the same frequency, the mixer will have a d.c. output whose amplitude will depend on the relative phase of the two input signals. The mixer output will be a maximum for zero phase difference and zero for 90° phase difference. Clearly the detector diode and amplifiers will introduce various unspecified phase shifts into the signal coming from the sample. To compensate, the phase of the reference signal can be adjusted by a phase shifter (see Appendix § 1.(iii) for circuit diagram). The mixer output is amplified (see Appendix § 1. (v) for the amplifier circuit diagram) and fed into a Nicolet 535 signal averager.

In operation the frequency synthesizer steps automatically through a preselected frequency interval in 100 or 1000 steps at a rate of 1, 3 or 10 ms per step. The signal averager stores the mixer output at each step so that successive frequency sweeps may be accumulated to improve the signal to noise ratio.

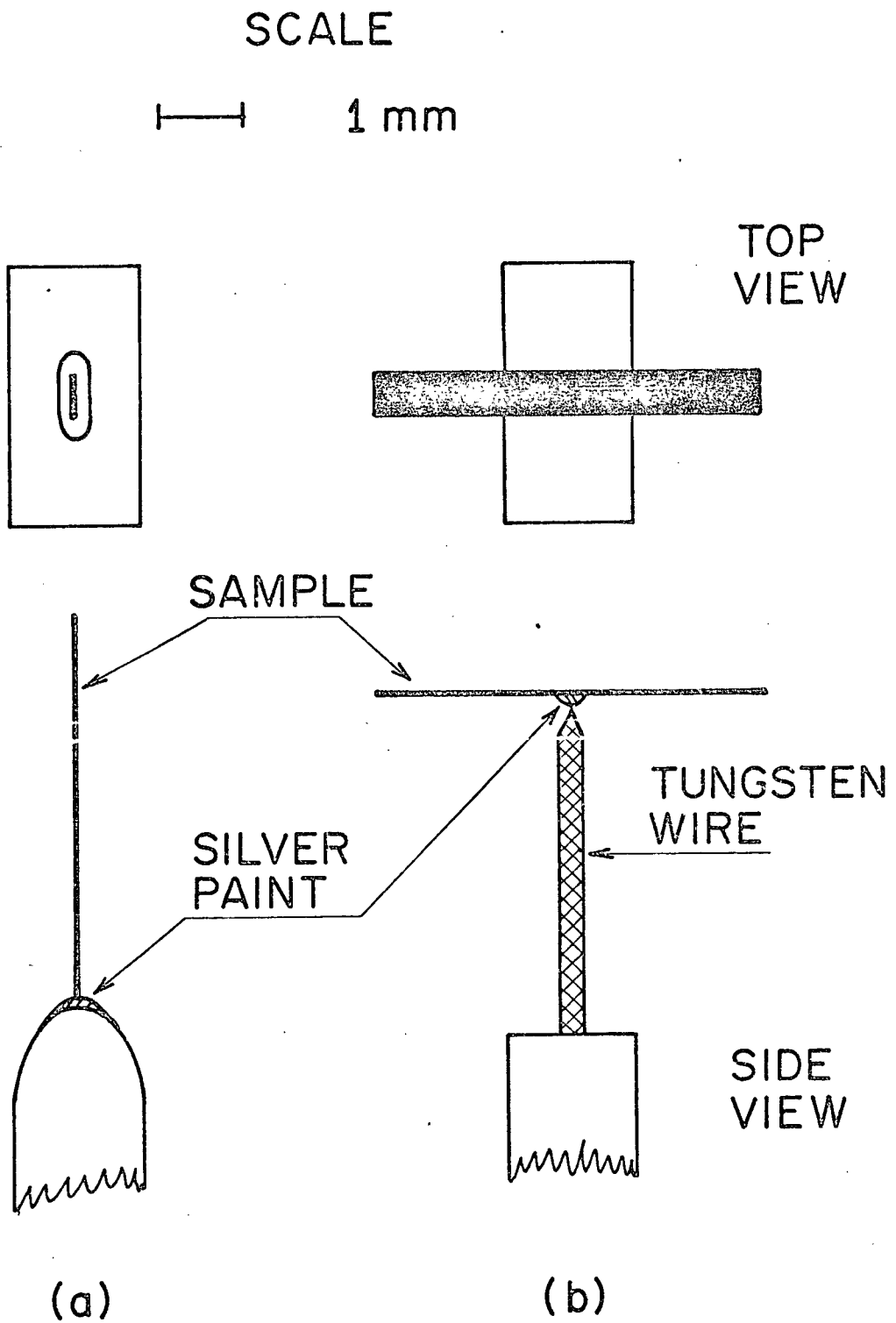
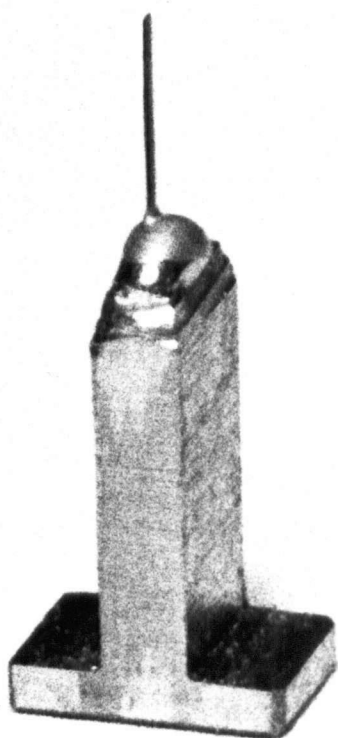
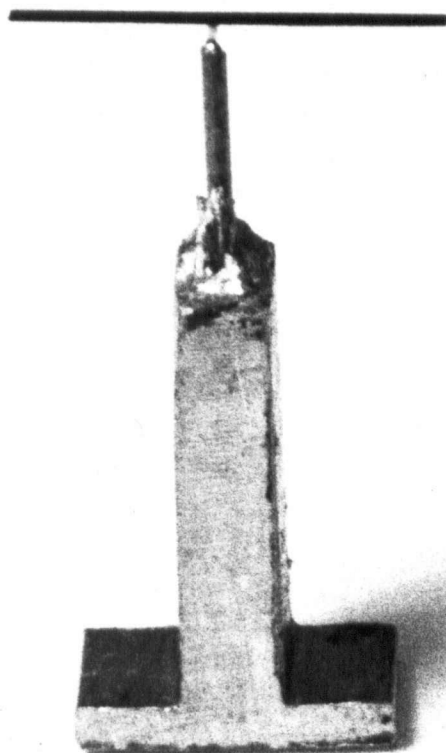


Fig. 18 - Sample mounting configurations



a



b

Fig. 19 - Photographs of mounted samples

Scale: 8 x actual size

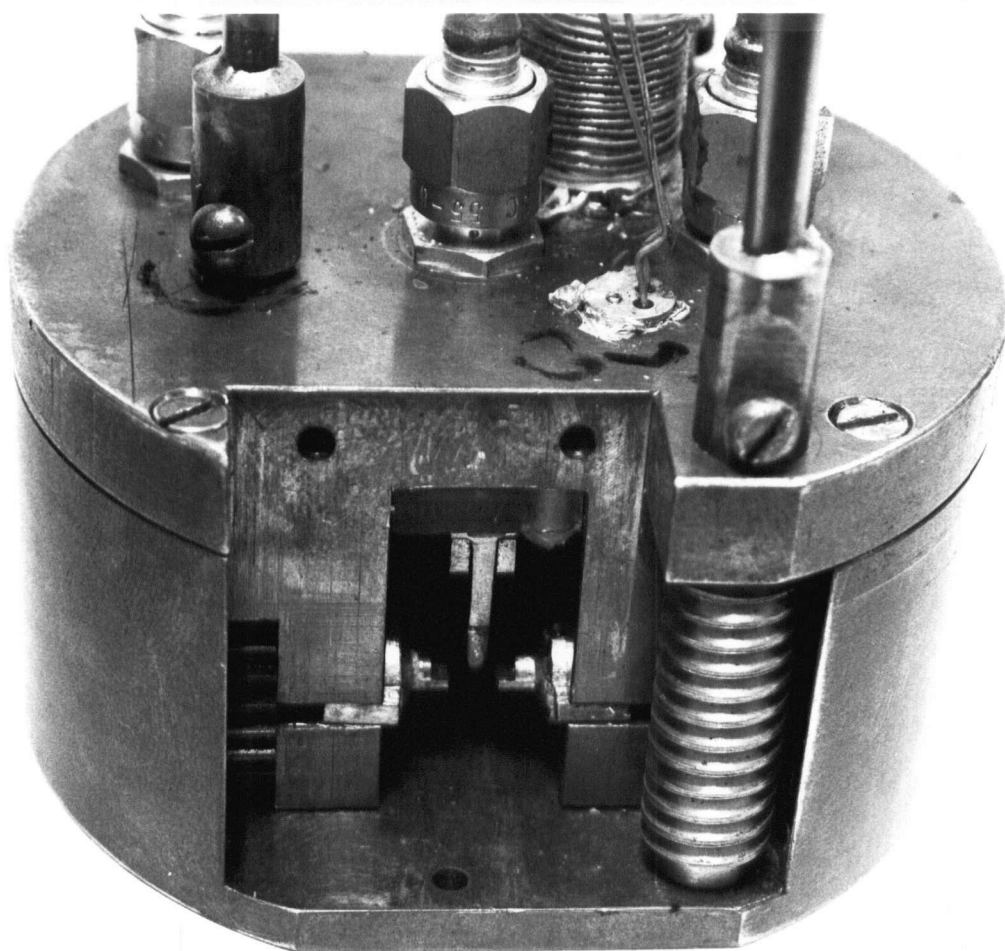


Fig. 21 - Photograph of the outside of the sample holder with the door plate removed.

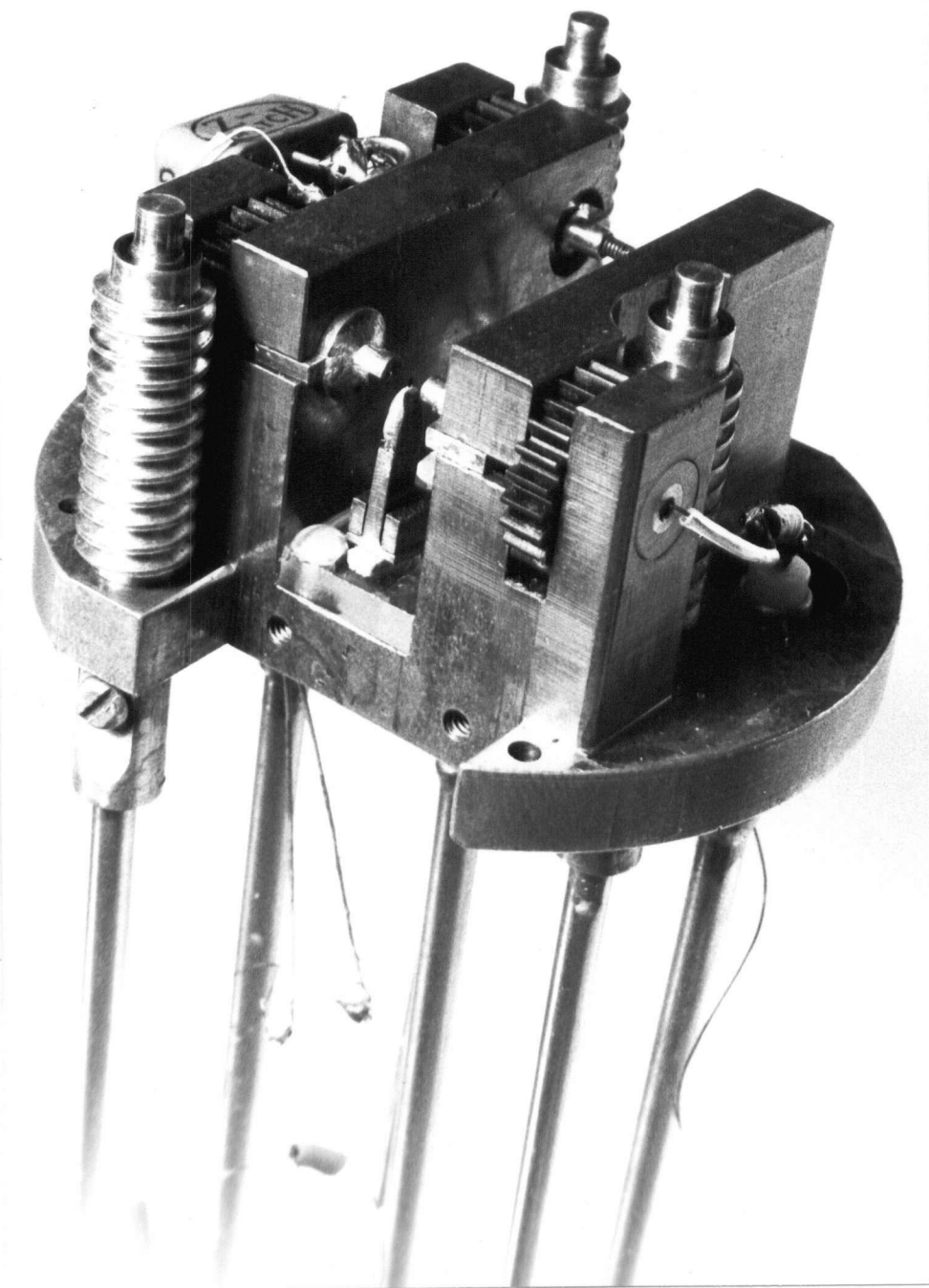


Fig. 22 - Photograph of the inside of the sample holder.
Note the a axis sample between the electrodes.

In practice one observes a series of peaks in the output as a function of the drive frequency. These peaks correspond to acoustic resonances in the sample or its support. The peak width, amplitude and centre frequency of these resonances are the quantities of interest.

(ii) Sample Support

In this section we describe the sample support mechanism and the ancillary low temperature apparatus. In all cases the TTF-TCNQ samples were glued to a conducting support with Dupont 4929 silver paint which was diluted with 2-butoxyethyl acetate to lengthen the drying time. Two basic mounting configurations were used as shown in Fig.18 and the photographs in Fig.19. In the "vibrating reed" configuration (Fig.18a) one end of the sample is glued to a brass support. In the other configuration (Fig.18b) the sample is attached to a pointed tungsten wire at the centre of its broad crystallographic *a b* face. In this case the glue contact spot is typically about .15 mm in diameter. A variety of different size tungsten wires were used from .003" to .015" in diameter. A point was etched on the wire electrolytically, in a 1M NaOH solution.

The mounted sample is held in a copper box between moveable shielded electrodes. A cut-away view of a sample mounted in the box is shown in Fig.20, and photographs of the outside and interior of the box are shown in Figs.21 and 22. Its main upper part was machined out of a single piece of copper to reduce rf leakage and improve the mechanical integrity

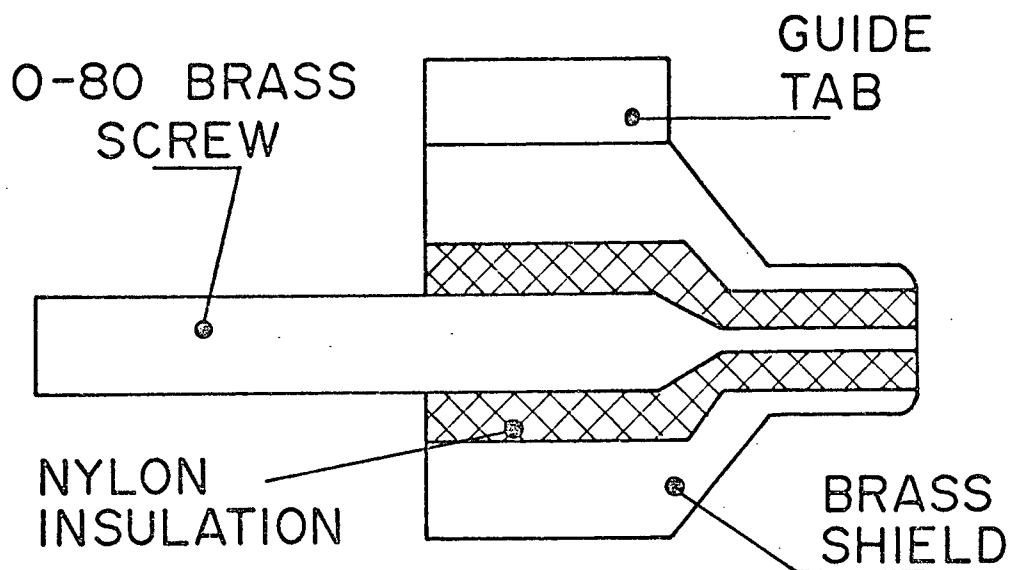


Fig. 23 - Shielded electrode

Scale: 8 x actual size

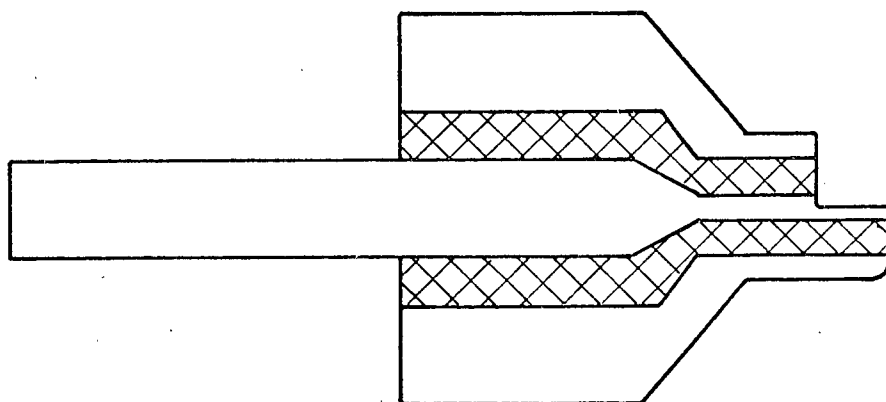


Fig. 24 - Special notched electrode
for small samples

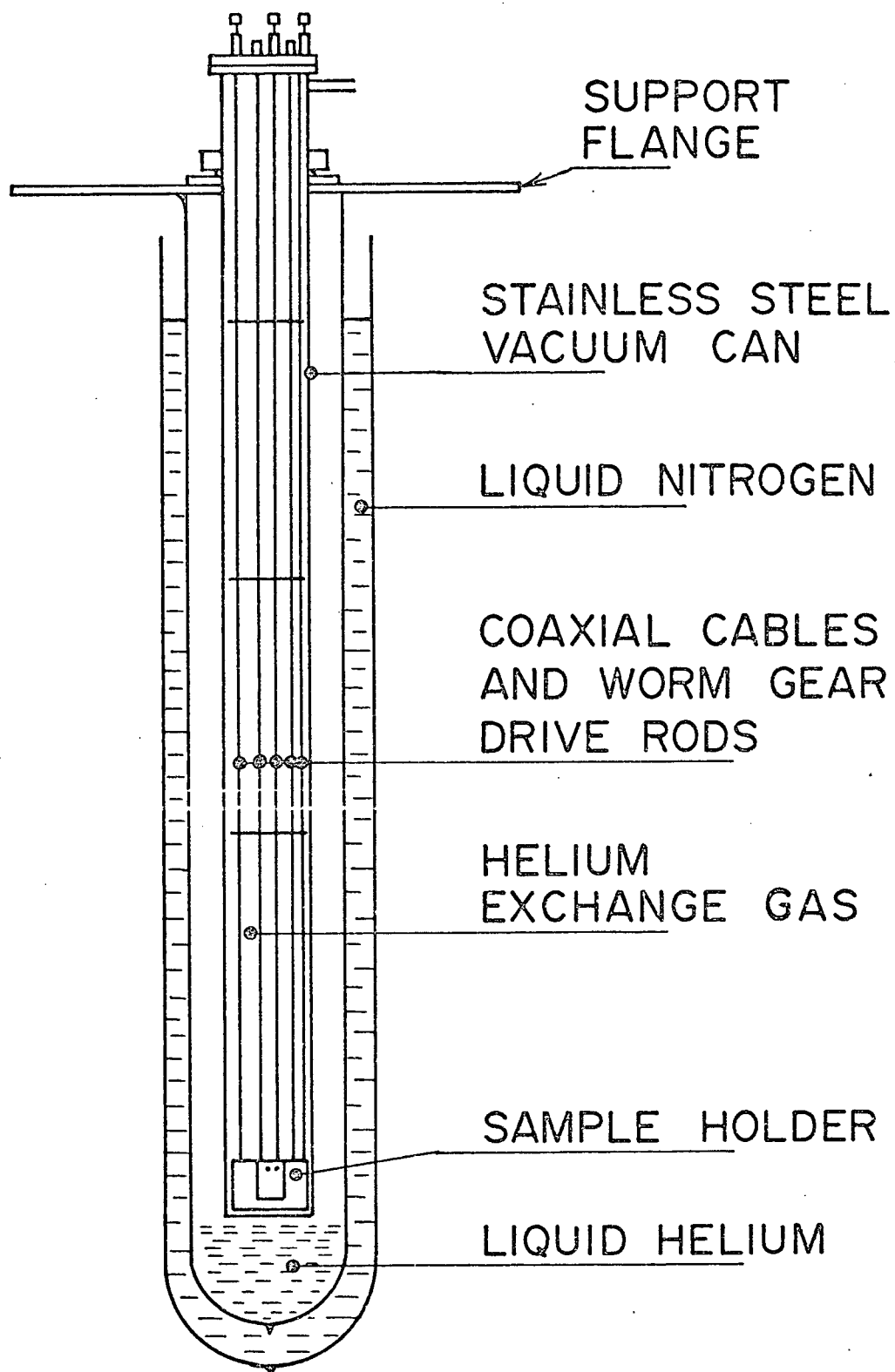


Fig. 25 - Cryostat for low temperature measurements

of the electrode drive mechanism. The electrodes can be removed from the box, so that different shape electrodes can be installed to match the size of the sample and the type of mode to be excited. Two of the electrodes used are shown in Figs.23 and 24. The notched electrode in Fig.24 was used with very small samples. The spacing between the electrode and the sample is adjusted to .01 - .10 mm by turning nylon spur gears threaded onto the 0-80 threaded brass shaft of the electrode. The spur gears in turn are driven by worms. One rotation of the worm gear moves the electrode by .013 mm, so that fine adjustments can be made to the spacing between the sample and the electrodes.

In addition to the electrode drive mechanism the copper box also contains the transformer and dummy sample needed for the bridge detection scheme described above (see Fig.20). The entire assembly is suspended by three 3 mm semi-rigid coaxial cables inside an evacuated stainless steel can, as shown in Fig.25. In addition, there are three pieces of thin walled stainless steel tubing connected to the worm gears. The three pieces of tubing protrude out of the top of the vacuum can through O ring seals, allowing adjustment of the positions of the electrodes when the sample chamber is evacuated. For low temperature measurements helium exchange gas is introduced into the can and allowed to circulate inside the copper box which contains the sample. As long as the pressure is ≤ 0.5 Torr, the exchange gas does not appreciably damp the sample vibration. During a low temperature run the vacuum can is normally suspended above the liquid level, in a

glass dewar containing liquid helium (Fig.25). In this mode of operation four litres of liquid helium will last about 24 hours.

The diode temperature sensor and heater on the top of the copper sample box (Fig.20) are used in conjunction with a Lakeshore Cryotronics diode temperature controller to maintain the copper box temperature constant to ≤ 10 mK. The diode (#D2755) was calibrated commercially and this calibration is given in the Appendix § 1. It was checked at liquid helium, liquid nitrogen and roughly at room temperature. In addition the diode was used to make four probe d.c. conductivity measurements as a function of temperature on a TTF-TCNQ crystal. The measured phase transition temperatures were consistent with earlier measurements (Tiedje 1975).

1.2 Sensitivity of the Measurement Technique

(i) Minimum Detectable Length Change

The sensitivity of the apparatus to small displacements of the sample was determined by driving an a axis sample in its fundamental flexural mode with a known driving voltage. When a force F is applied to the free end of a cantilever beam of length ℓ , according to elementary beam theory the resonant displacement of the free end is

$$\Delta d = \frac{Q}{3} \frac{F\ell^2}{EI}$$

where E is the Young's modulus, I is the area moment of inertia of the cross-section of the beam, and Q is the quality factor of the

mechanical resonance. The minimum detectable displacement is determined from the signal to noise ratio (SNR) for a known driving force F by

$$\Delta d_{\min} = \Delta d / \text{SNR}.$$

The force on the end of the beam can be estimated from the force on the plates of a charged parallel plate capacitor which is

$$F = \frac{\epsilon_0 A}{2} \frac{V^2}{d^2}$$

where A is the area of the plates, d is the plate separation and V is the voltage on the capacitor.

We consider Sample #22 with dimensions $0.335 \times 0.204 \times 0.018$ mm as an example. This sample had its fundamental flexural mode at 118 kHz, with an air damped Q of 100 at room temperature. The drive and detector electrodes covered the bottom third of the sample and were separated from the sample by approximately 0.08 and 0.02 mm respectively. Using the room temperature axis Young's modulus of 3.1×10^{11} dynes/cm² (see Chapter II below), the measured driving voltage (10V) and signal to noise ratio (176), we calculate that the minimum detectable displacement is $\Delta d_{\min} \approx 8 \times 10^{-11}$ cm. For the SNR of 176 quoted above, the signal averager output noise bandwidth was 1.2 Hz. According to the parallel plate formula, the pickup capacitor had a capacitance of 9×10^{-3} pf.

(ii) A.C. Method

In this section we examine some of the practical limitations to the sensitivity of the capacitive displacement measuring technique. We consider the simplified model of the detector circuit shown in the schematic in Fig.26 below.

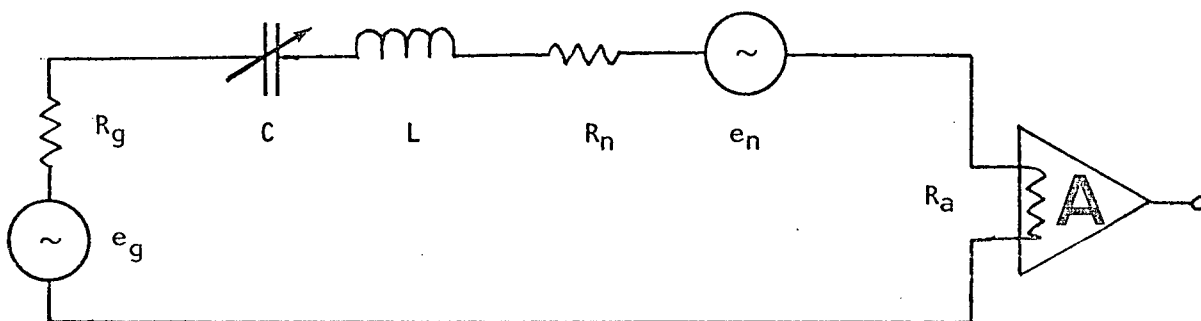


Fig. 26 - Capacitive Vibration Detector - A.C. Method

The noise source e_n is assumed to be due to Johnson noise in the resistive element in the LC resonant circuit, in which C is the pickup capacitor. We have ignored the generator noise, because in principle it can be cancelled out by a suitable bridge detection scheme. We also assume that the effective impedance of both the generator and the amplifier input can be adjusted to any desired value by impedance matching using transformers, for example. The matching circuitry has been omitted in Fig. 26 for clarity.

For optimum noise performance most rf amplifiers require a source impedance about equal to their input impedance. This condition will be satisfied at resonance provided $R_a = R_n + R_g$. Furthermore, we assume that the amplitude of the rf carrier signal is limited by the power dissipation in the sample, or equivalently by the power dissipation in the resistor R_n . In this situation the optimum transformed generator impedance is zero. Normally one detects changes in the pickup capacitance by monitoring the amplitude of the transmitted rf signal. In this case the circuit is most sensitive when the generator frequency $\omega_{\text{gen}} = \omega_e \left(1 \pm \frac{1}{2Q_e}\right)$ where ω_e is the resonant frequency of the LC circuit and Q_e is the quality factor for the electrical resonance.

When all of the above conditions are met the minimum detectable change in capacitance is

$$[1] \quad \frac{\Delta C}{C} = \zeta \frac{2}{Q_e} \frac{[k(T + T_a)\Delta\nu]^{\frac{1}{2}}}{P^{\frac{1}{2}}}$$

where T is the temperature of the resistor R_n , T_a is the noise temperature of the amplifier (Motchenbacher and Fitchen 1973) and $\Delta\nu$ is the output noise bandwidth of the detector. In eqn.[1] ζ is a factor which sets the desired detection threshold for a capacitance change. For example when $\zeta = 1$, a signal is considered to be detected if it has an amplitude equal to the rms noise level. In this section we use $\zeta = 2$. P is the power dissipated in R_n . An expression similar to [1] has been obtained by Braginskii and Manukin (1977).

In practice the power dissipation is not usually a limitation. The limiting factor is more likely to be the capacitor breakdown voltage. In this case, when the breakdown voltage is V_{\max} , the minimum detectable capacitance change is

$$[2] \quad \frac{\Delta C}{C} = \zeta \frac{4 [2k(T + T_a)\Delta v]^{\frac{1}{2}}}{(\omega_e C Q_e)^{\frac{1}{2}} V_{\max}} = \frac{\Delta d}{d}$$

where $\Delta d/d$ is the corresponding fractional change in the spacing of the capacitor plates.

An order of magnitude estimate for the maximum Q_e of an LC resonant circuit at room temperature is 100, taking into account coupling losses. Much higher Q_e 's could be obtained using superconducting circuits. For example, $Q_e > 10^6$ can be achieved for superconducting LC circuits and even higher Q_e 's are possible in superconducting cavity resonators (Hartwig 1973). However, we will consider room temperature circuits only.

It is interesting to compare the experimental sensitivity to the theoretical limit [2]. If the following values are used: $T = 300K$, $T_a = 170K$ (Avantek AMM-1010 amplifier), $\omega_e = 4 \times 10^9 \text{ s}^{-1}$, $C = 9 \times 10^{-3} \text{ pf}$, $Q_e = 100$ and $V_{\max}/d = 10^5 \text{ V/cm}$ (Cantrell and Breazeale 1974) then the limiting displacement is $\Delta d \approx 2 \times 10^{-13} \sqrt{\Delta v} \text{ cm}$. Experimentally the rf field on the detector capacitor is likely to be at least an order of magnitude less than 10^5 V/cm . Accordingly the experimental sensitivity of $8 \times 10^{-11} \sqrt{\Delta v} \text{ cm}$ is probably only about an order of magnitude less than the limiting value predicted from [2], using the actual rf field.

By judicious selection of the resonance frequency ω_e , $(\omega_e C Q_e)^{-1} \sim 1\Omega$ can be achieved at room temperature for a wide range of pickup capacitance. For $(\omega_e C Q_e)^{-1} = 1\Omega$, $\Delta d \approx 10^{-14} \sqrt{\Delta v}$ cm. Braginskii et al (1971) have built a detection system capable of measuring $\Delta d \approx 3 \times 10^{-14} \sqrt{\Delta v}$ cm with $C \sim 2000$ pf and $\omega_e = 3 \times 10^7$ s⁻¹.

(iii) D.C. Method

For comparison purposes we now consider the d.c. analogue of the capacitive displacement measuring technique described above. In the d.c. approach, a constant bias voltage rather than an a.c. signal, is used as a probe to measure changes in the pickup capacitance. A schematic of the detector circuit is shown in Fig. 27 below. Changes in the pickup capacitance C alter the stored charge and induce currents in the bias resistor R_b . Accordingly any vibration of the sample is reflected in a voltage on the bias resistor.

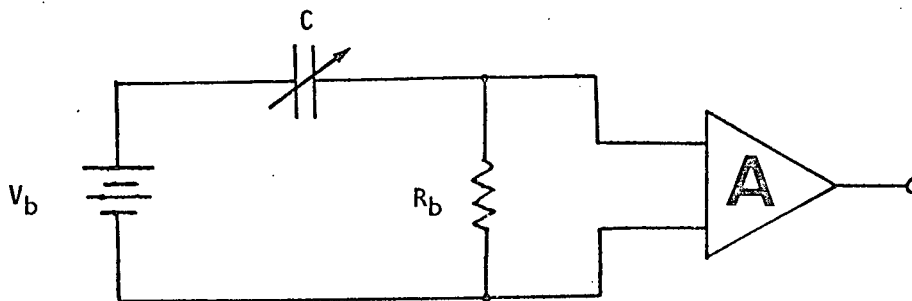


Fig. 27 - Capacitive Vibration Detector - D.C. Method

There are two main noise sources in the circuit shown in Fig. 27. They are the Johnson noise in the bias resistor and the amplifier noise. In order to estimate the sensitivity of the detector some information about the noise performance of the amplifier input stage is required. For vibration frequencies up to 10 MHz at least, the best available device for the input stage is a junction field effect transistor (JFET). To be specific, we will consider a Siliconix 2N4867 transistor which is a good low noise commercially available device.

A noise equivalent circuit for the capacitive detector using an amplifier with a JFET input stage, is shown in Fig. 28 below.

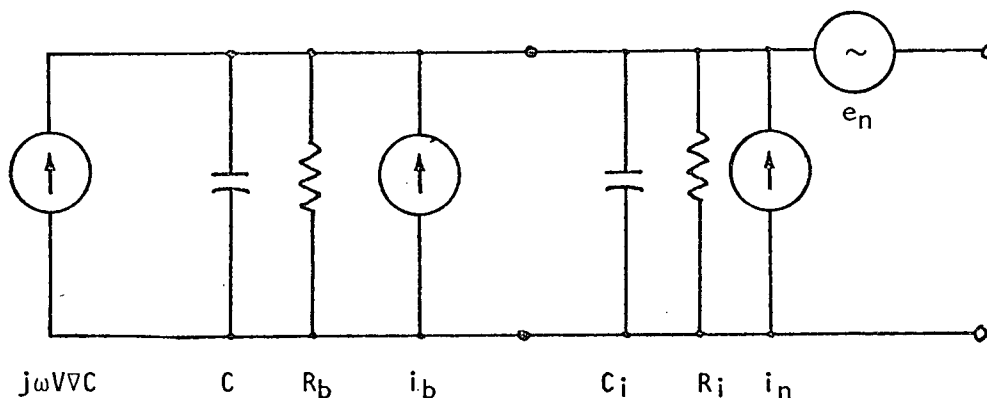


Fig. 28 - Noise Equivalent Circuit

The Norton equivalent circuit has been used for the bias resistor noise generator. The mean-square resistor noise current $\overline{i_b^2}$ is $4kT\Delta\nu/R_b$.

The current signal generated by the oscillating capacitance is represented by an equivalent current source $j\omega\Delta CV$, where ω is the mechanical vibration angular frequency. At midband the rms voltage noise e_n for the 2N4867 JFET is $2 \times 10^{-9} \text{ V } \sqrt{\Delta\nu}$ and the current noise i_n is $3 \times 10^{-15} \text{ A } \sqrt{\Delta\nu}$. Below 30 hz e_n is dominated by $1/f$ noise and above 10 khz i_n increases linearly with ω .

From the equivalent circuit in Fig. 28 we find that the minimum detectable capacitance change is

$$[3] \quad \frac{\Delta C}{C} = \frac{\zeta}{\omega CV} \left\{ i_b^2 + i_n^2 + e_n^2 \left[\left(\frac{1}{R_i} + \frac{1}{R_b} \right)^2 + \omega^2 (C + C_i)^2 \right] \right\}^{\frac{1}{2}} = \frac{\Delta d}{d}$$

for a 1 hz bandwidth. The highest sensitivity is achieved by using the largest possible bias resistor R_b up to a resistance of $[\omega(C + C_i)]^{-1}$ or where the current noise i_n dominates, at which time the sensitivity becomes independent of R_b . A reasonable upper limit for R_b is $10^8 \Omega$. We assume the input resistance of the JFET is larger than this and that $C_i = 5 \text{ pf}$. If we substitute the circuit parameters given above into [3] and use $C = 9 \times 10^{-3} \text{ pf}$ and $\omega = 7.4 \times 10^5 \text{ s}^{-1}$ corresponding to the first flexural mode of Sample #22 then the minimum detectable displacement is $\Delta d \approx 10^{-10} \text{ cm}$ when the bias field on the capacitor is 10^5 V/cm .

A contour map in the (ω, C) plane of the displacement measuring sensitivity of the d.c. capacitive technique is shown in Fig. 29. From the contour map we conclude that the d.c. method works best for high vibration frequencies and large pickup capacitances. In this regime

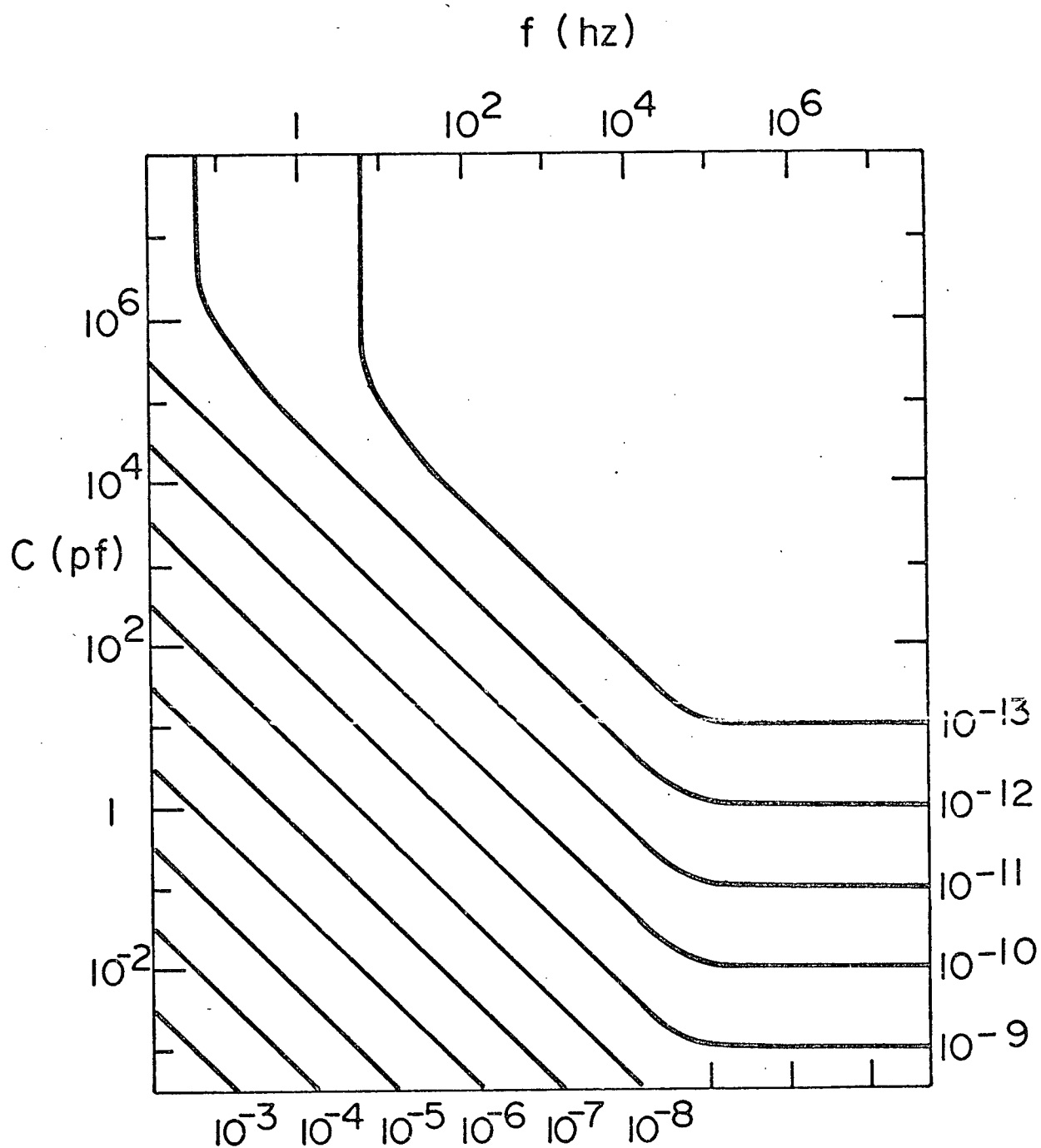


Fig. 29 - Minimum detectable displacement Δd as a function of frequency f and pickup capacitance C using the d.c. method. The contour labels are in centimeters.

its sensitivity is comparable with the a.c. method where $\Delta d \sim 10^{-14} \sqrt{\Delta v}$ cm. However, the d.c. method is less satisfactory for low vibration frequencies and small samples for which the pickup capacitance is necessarily small.

CHAPTER II

The Modes of Vibration of TTF-TCNQ Crystals

2.1 Low Frequency Modes of an elongated plate

The acoustic mode spectrum of an elastic body is exceedingly complex even for objects with simple shapes. It is feasible to calculate the acoustic resonance frequencies for only a few special cases. Provided that the material is elastically isotropic, the infinite medium, the infinite thin plate, the infinite cylinder, and the sphere are soluble. For arbitrary crystallographic symmetry only the infinite medium is soluble, although the other cases are soluble for certain types of elastic anisotropy. It is interesting to note that the acoustic resonator problem is much more complex than the comparable electromagnetic resonator problem. An intuitive explanation is that there are only two electromagnetic waves possible in an infinite medium, namely two linearly polarized transverse waves, whereas in the acoustic case there are three waves possible - two transverse waves and one longitudinal wave. The acoustic resonator we are interested in here is an elongated, approximately rectangular parallelepiped with monoclinic symmetry. Although it is not possible to calculate all of the resonance frequencies of a TTF-TCNQ crystal, it is possible to obtain some very good approximations for the low frequency modes.

To begin with let us assume that TTF-TCNQ is elastically isotropic, in order to simplify the discussion. The complications arising from

elastic anisotropy will be discussed later, although it will turn out that TTF-TCNQ is not far from being isotropic, elastically.

(i) Flexural Modes

The lowest frequency mode of the elongated platelet is a bending ("flexural") mode with displacements perpendicular to the broad face of the platelet. Since the TTF-TCNQ platelets are geometrically similar to an ordinary plastic ruler, the low frequency modes can be readily visualized with the help of a ruler. The ruler has three different types of modes which could be classified as flexural. The lowest frequency type (labelled F_{bc}) corresponds to bending along the length of the ruler with displacements perpendicular to the broad face. The second type (F_{ba}) is the same as the first except that the displacement is perpendicular to the edge of the ruler. The third type (F_{ac}) is a bend across the width of the ruler with displacements perpendicular to the broad face. The rationale behind the mode labelling scheme will become clear later.

The propagation of a flexural wave along a beam whose long axis is parallel to y , is described by the wave equation

$$[1] \quad \frac{\partial^2 u}{\partial t^2} + \frac{EI}{\rho A} \frac{\partial^4 u}{\partial y^4} = 0$$

in the limit that the wavelength is long compared to the beam thickness. In equation [1] u is the displacement of the beam centre line from the equilibrium position, A is the crosssectional area of the

beam, and E is its Young's modulus. The area moment of inertia I is the moment of inertia of the beam cross-section about a line through the beam centre line which is perpendicular to both the direction of the displacement u and the long axis of the beam. Consider the foot long ruler again as an example. If t is its thickness and w its width then $I = t^3w/12$ for the soft F_{bc} modes and $I = w^3t/12$ for the stiff F_{ba} modes. Equation [1] also applies to flexural modes in thin plates. For an isotropic plate with Poisson's ratio ν and a width much larger than a flexural wavelength, the Young's modulus E in [1] is replaced by the plate modulus $E/(1 - \nu^2)$.

The flexural resonance frequencies are determined by looking for the solutions of [1] which satisfy the boundary conditions on the ends of the beam. The resonance frequencies are given by (Timoshenko 1974)

$$[2] \quad f_n = \frac{1}{2\pi} \sqrt{\frac{EI}{\rho A}} \left(\frac{m_n}{\ell} \right)^2$$

where ℓ is the length of the beam and m_n is the n^{th} root of a transcendental equation which is specified by the boundary conditions. The boundary conditions of interest here are "clamped-free" for the vibrating reed (cantilever beam) configuration and "free-free" for the central pin support. For these boundary conditions the first four m_n values are given in Table III

TABLE III
Flexural Mode Parameters

	m_0	m_1	m_2	m_3
Clamped-Free	1.875	4.694	7.855	10.996
Free-Free	0	4.730	7.853	10.996
$(n + \frac{1}{2})\pi$	1.571	4.712	7.854	10.996

and the corresponding mode shapes are shown in Fig. 30.

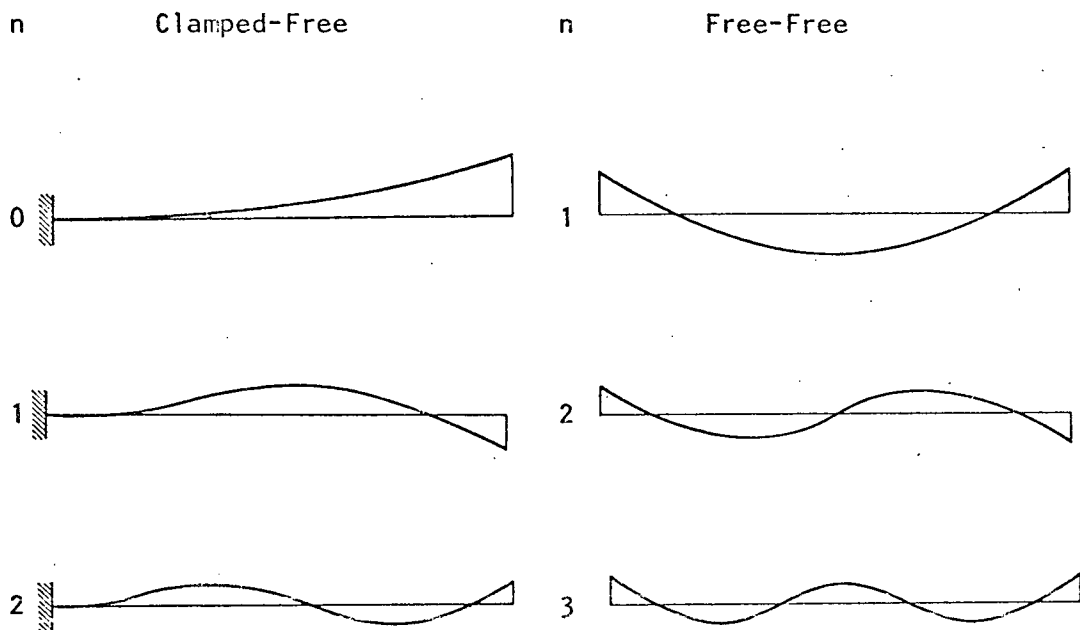


Fig. 30 - Flexural Mode Shapes

For large n , m_n asymptotically approaches $(n + \frac{1}{2})\pi$.

As pointed out earlier the one dimensional wave equation [1] is only a good approximation if the flexural wavelength is long compared to the beam thickness. Furthermore the approximation will break down if the shear modulus is very small. The importance of the shear modulus is best illustrated by considering the extreme case of a pad of paper where the shear force between sheets is nearly zero. In this case the flexural rigidity of the pad of paper is dominated by

the shear modulus between sheets and is therefore close to zero. In less extreme cases the contribution of the shear modulus is negligible, and the beam rigidity is determined entirely by the compression of the concave side of the beam and the extension of the convex side. Nevertheless, because of the chainlike nature of the crystal structure of TTF-TCNQ it has been suggested that the interchain shear moduli may be unusually small (Barmatz et al 1974).

The shear modulus and finite beam thickness can be taken into account by adding some more terms to [1] (Timoshenko 1974). If the modified differential equation is solved for the resonance frequencies, one finds that the additional terms in the equation reduce the effective Young's modulus for the n^{th} flexural mode in [2], by the factor (Goens 1931)

$$[3] \quad 1 + K \left(\frac{t}{\ell} \right)^2 m_n^2 \frac{E}{G}$$

where $K \sim 1$ and G is a shear modulus. The beam thickness t is measured in the direction of the beam displacement during bending. In order to obtain an exact expression for the resonance frequency of even the lowest frequency flexural mode one would have to solve a three dimensional differential equation and look for solutions which match the boundary conditions over the entire surface of the beam rather than just at its ends.

In the samples which are supported by the central pin, the post at the centre provides an additional constraint which is not easily dealt with

using simple beam theory. However, for the lowest flexural mode a semiquantitative estimate of the effect of the central support can be obtained from the numerical calculations of Southwell (1922) for centrally pinned discs. The effect of even a very small pin contact area is to raise the zero frequency $n = 0$ mode of a free-free beam up to about 80% of the $n = 1$ mode frequency. The flexural modes with a mode at the centre and the higher frequency flexural modes are not affected very much by the pin.

(ii) Torsional Modes

We now consider the low frequency torsional (T) modes of the elongated platelet (or ruler). The displacement of the platelet for the torsional modes we are interested in here, is a volume conserving strain in which neighbouring crosssections perpendicular to the long axis of the sample are twisted relative to one another. The propagation of torsional waves along a beam which is long compared to its lateral dimensions is described by the wave equation (Landau and Lifshitz 1970)

$$[4] \quad \frac{\partial^2 \phi}{\partial t^2} = \frac{C}{\rho I_p} \frac{\partial^2 \phi}{\partial y^2}$$

where the long axis of the beam is along y as before, and ϕ is the angle of rotation of a crosssection. I_p is the area moment of inertia of a crosssection about its centre, and C and ρ are the torsional rigidity and density of the beam respectively. The torsional resonance frequencies

for a beam of length ℓ are given by

$$[5] \quad f_n = \sqrt{\frac{C}{\rho I_p}} \frac{n}{4\ell}$$

For the clamped-free boundary conditions n is an odd integer and for the free-free boundary conditions n is an even integer.

Unless the crosssection of the beam is circular, plane crosssections become warped under torsion. Because of this feature, the torsional rigidity is a complicated function of the shape of the crosssection (Timoshenko 1951). The torsional rigidities for some simple shapes are given by Landau and Lifshitz (1970). For a beam with a rectangular crosssection of width w and thickness $t \leq 0.2 w$, C is given by (Timoshenko 1951)

$$[6] \quad C = G \frac{t^3 w}{3} \left(1 - \frac{192}{\pi^5} \frac{t}{w} \right).$$

In the $t \ll w$ limit, the torsional resonance frequencies in [5] reduce to

$$f_n = \frac{t}{w} \sqrt{\frac{G}{\rho}} \frac{n}{2\ell}$$

where G is the shear modulus, as before.

In theory, if the lateral dimensions of the beam are comparable to a torsional wavelength then a correction factor analogous to [3] is needed in the expression for the torsional resonance frequencies. In practice the correction factor does not change the frequency much even when the

lateral dimension is equal to a half wavelength. Furthermore an approximate theoretical calculation of the correction factor is apparently in disagreement with experimental results (Behrens 1968). This correction will be ignored here.

(iii) Comments on a Short Plate

We now describe qualitatively the low frequency modes of a plate in which the width of the plate is comparable to its length. This situation is of interest because it illustrates what happens to the modes of an elongated plate when the wavelength is comparable to its width. In addition some measurements were made on nearly square platelets cut off the end of standard elongated TTF-TCNQ crystals.

The low frequency modes of a plate are usually illustrated by Chladni figures, which are the patterns of nodal lines of the modes (Waller 1961, Leissa 1969). The experimentally determined patterns of nodal lines for the first few modes of a square cantilever plate and a rectangular free plate are shown in Fig.31 and 32 respectively. Observe that the first mode in Fig.31 appears to be purely flexural, the second one torsional and the third one flexural again. The fourth mode looks like a transverse flexural mode, but it is not purely flexural because of the edge clamp. Although the frequency of this mode cannot be calculated accurately using the simple beam formulas, the frequency of the first two modes can be calculated with reasonable accuracy from [2] and [5], since the vibration wavelength for both modes is at least four times the width of the "beam". In addition the first two modes are well separated from

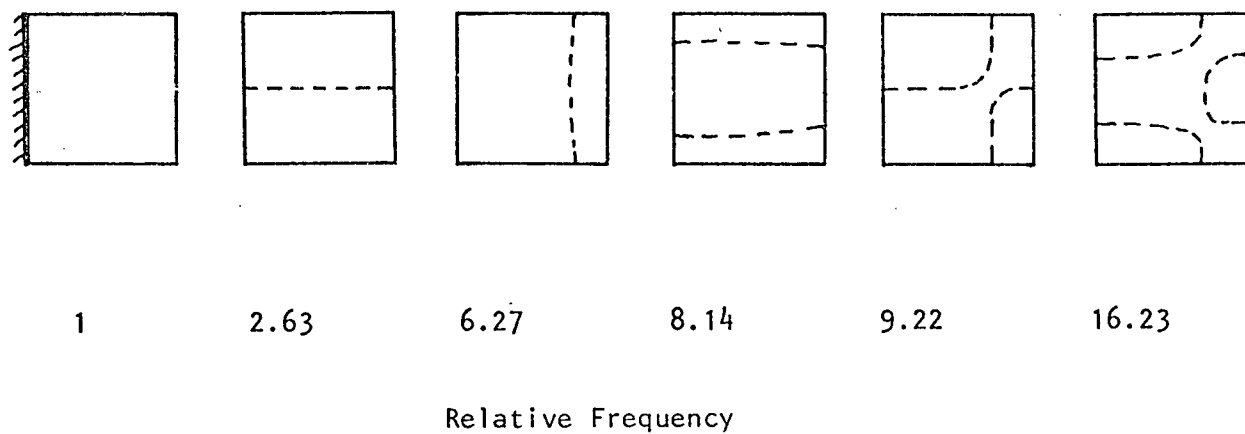


Fig. 31 - Modes of a Square Cantilever Plate

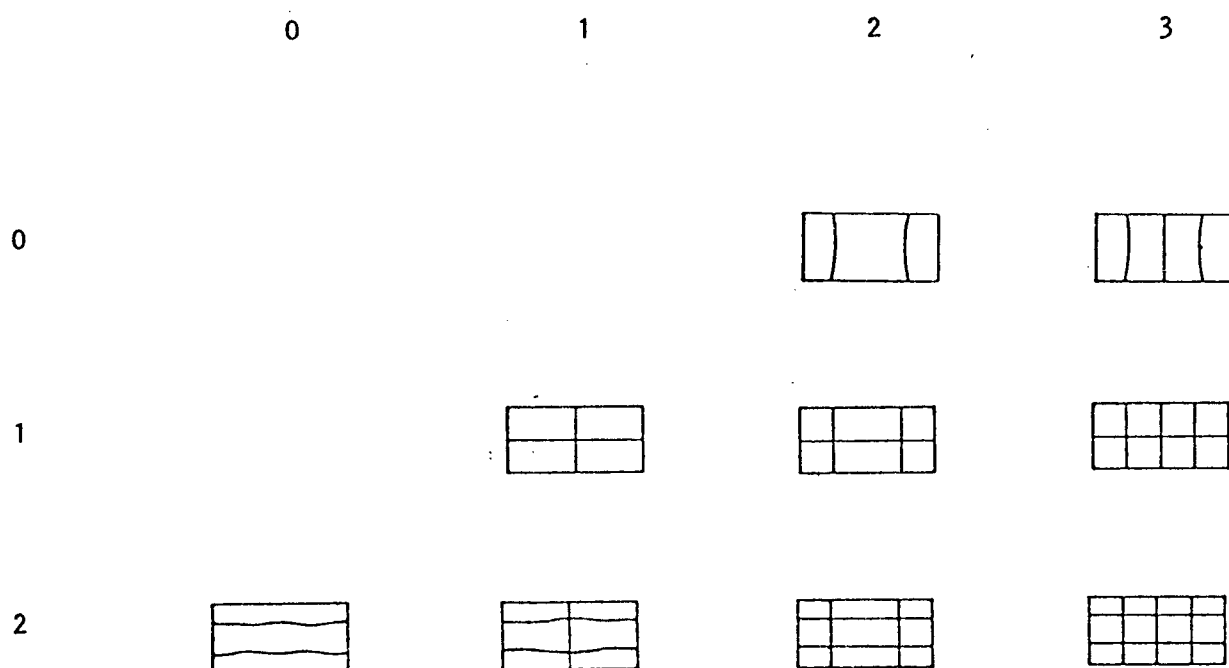


Fig. 32 - Modes of a Rectangular (2:1) Free Plate

their neighbours in frequency, making them easy to identify experimentally.

An examination of the nodal patterns in Fig.32 shows that just as for the cantilever plate, the higher frequency modes are likely to be a complex mixture of torsion and flex. It is difficult to obtain information about the elastic moduli from these modes because of their complicated nature. We now temporarily leave the subject of torsional and flexural vibrations and investigate another simple type of vibration of a long plate.

(iv) Elongational Modes

The final type of mode which we will consider is the longitudinal stretch or elongational (L) mode. The propagation of an extensional wave along a rod oriented parallel to the y axis, is described by the wave equation

$$[7] \quad \frac{\partial^2 u}{\partial t^2} = \frac{E}{\rho} \frac{\partial^2 u}{\partial y^2}$$

where u is the displacement of the rod along its axis. The Young's modulus E appears in [7] rather than a bulk wave longitudinal modulus because the rod is free to expand or contract laterally depending on whether it is being compressed or extended longitudinally.

As before, the resonance frequencies are obtained by looking for solutions of the wave equation which satisfy the boundary conditions

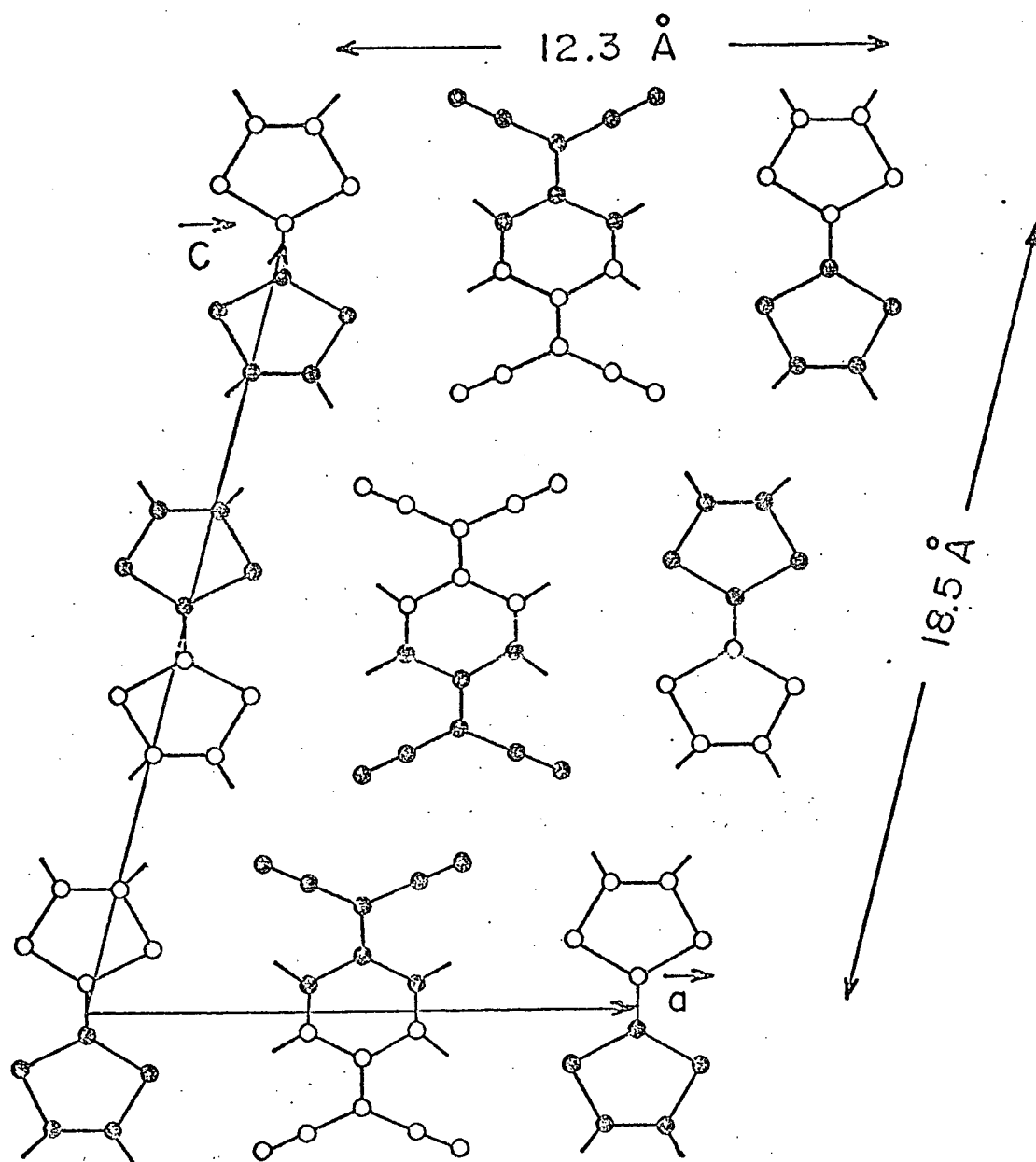


Fig. 33 - Arrangement of TTF and TCNQ molecules in the a c plane.
The solid dots are tipped up above the plane.

on the ends of the beam. For free-free boundary conditions the resonance frequencies are

$$[8] \quad \bar{f}_n = \sqrt{\frac{E}{\rho}} \frac{n}{2\ell} \quad .$$

For short beams and high frequencies the longitudinal acoustic wavelength may be comparable with the transverse dimensions of the beam. In this situation, the one dimensional wave equation [7] is no longer a good approximation just as the one dimensional equations for the flexural and torsional waves are no longer a good approximation in the same limit. Provided the wavelength is not too short, the elongational resonance frequencies may be corrected by dividing the Young's modulus E by the factor (Love 1944)

$$[9] \quad 1 + \frac{1}{3} \left(\frac{n\pi}{2\ell} \right)^2 \nu^2 (t^2 + w^2)$$

for a beam with Poisson's ratio ν and a rectangular crosssection.

(v) Crystallographic Symmetry

Up to now we have assumed the vibrating plate or beam to be made of an isotropic material. However, the TTF-TCNQ samples on which the measurements were made are not isotropic; rather, they are monoclinic crystals (space group $P2_1/C^\dagger$). The positions of the TTF and TCNQ molecules in the crystallographic a c plane are shown in Fig. 33

[†] This notation is explained by Henry and Lonsdale (1951).

(Blessing and Coppens 1974). Fig. 2 shows the segregated stacking arrangement of the molecules in the b direction which is largely responsible for the unusual electrical properties of TTF-TCNQ.

All of the UBC grown TTF-TCNQ crystals have the unique (b) axis parallel to the long axis of the crystal and the a axis parallel to the broad transverse dimensions. The c axis is about 14.5° away from being perpendicular to the other two axes; hence it is not quite perpendicular to the broad a b face of the crystal. This feature allows a two fold ambiguity in the direction of the c axis in a real crystal and opens up the possibility that what appears to be a single crystal may actually be twinned. For convenience we will use the reciprocal lattice vector c^* which is defined to be perpendicular to a and b , instead of c when discussing the vibration modes in relation to the crystallographic symmetry axes.

Monoclinic acoustic resonators are not easy to deal with theoretically, because in general 13 independent elastic constants need to be considered (Auld 1973). In a beam made of a monoclinic material, the flexural modes are coupled to the torsional modes in a complex way, by certain elastic constants. However, if the TTF-TCNQ c axis were perpendicular to a (or the crystal were suitably twinned), the flexural modes and torsional modes would be uncoupled. To make the vibration problem manageable we will assume that c is perpendicular to a . This amounts to assuming that the samples have orthorhombic symmetry and that the crystallographic symmetry axes are aligned along the symmetry axes of the sample crystal. The approximation is probably not unreasonable since the c axis is only 14.5° away from being perpendicular to the a axis.

In general an orthorhombic material has nine elastic constants, which may be broken down into three Young's moduli, three Poisson's ratios and three shear moduli. The elastic moduli are most conveniently defined in terms of the 6X6 compliance matrix s_{ij} (Auld 1973). The Young's moduli E_a , E_b and E_c for the three crystallographic symmetry directions are equal to s_{11}^{-1} , s_{22}^{-1} and s_{33}^{-1} respectively when the a b and c^* axes are aligned parallel to the x y and z axes. Similarly the three shear moduli c_{44} , c_{55} and c_{66} are equal to s_{44}^{-1} , s_{55}^{-1} and s_{66}^{-1} respectively (Lekhnitskii 1963).

The expressions for the resonance frequencies of isotropic beams can be readily generalized to apply to orthorhombic beams. Let us consider the flexural modes first. The Young's modulus in the frequency expression [2] should be the modulus along the direction in which the beam is compressed and extended during vibration. For example, the relevant Young's modulus for the F_{bc} and F_{ba} modes is E_b . The shear modulus which goes into the correction factor [3] is best described with the help of the pad of paper analogy. If the beam were a stack of weakly interacting sheets, bent in its softest direction, the appropriate shear modulus to put into the correction factor would be the modulus against sliding of the sheets on top of one another in a direction parallel to the long axis of the beam. For the F_{bc} modes, c_{44} is the appropriate shear modulus. The elastic constants which apply to the three experimentally observed types of flexural modes are summarized in Table IV.

TABLE IV
Flexural Mode Elastic Constants

Mode	Young's Modulus [†] E	Shear Modulus [†] G
F _{bc}	E _b	c ₄₄
F _{ba}	E _b	c ₆₆
F _{ac}	E _a	c ₅₅

[†] refer to eqn. [2] and [3]

The torsional rigidity has been calculated for an orthorhombic beam with a rectangular crossection in the books by Hearmon (1961) and Lekhnitskii (1963). The results may be readily adapted to the two different types of torsional modes which were studied experimentally. In the first type of mode (T_a mode) the torsion axis is parallel to the a axis. In this case the torsional rigidity [6] should be replaced by

$$[10] \quad C = c_{66} \frac{t^3 w}{3} \left(1 - \frac{192}{\pi^5} \frac{t}{w} \left(\frac{c_{66}}{c_{44}} \right)^{\frac{1}{2}} \right)$$

for $t \leq 0.2 w$ and $c_{66} \sim c_{44}$. The thickness t is to be measured in the c^* (thin) direction, and the width is measured in the b direction.

Similarly, when the torsion axis is parallel to b (T_b mode)

$$[11] \quad C = c_{66} \frac{t^3 w}{3} \left(1 - \frac{192}{\pi^5} \frac{t}{w} \left(\frac{c_{66}}{c_{55}} \right)^{\frac{1}{2}} \right)$$

where t is measured in the c^* as before, and the width w is measured in the a direction.

It is trivially easy to generalize the expression for the elongational mode frequencies to an orthorhombic beam. One need only replace the isotropic Young's modulus E in [8] by the b axis Young's modulus E_b . Although only the b axis modes were measured experimentally, the frequencies of elongational modes for beams with long axes in the a or c direction could be calculated in an exactly analogous way. Similarly, the correction factor [9] for the b axis mode should be replaced by (Behrens 1968)

$$[12] \quad 1 + \frac{1}{3} \left(\frac{n\pi}{2\ell} \right)^2 \left(v_{12}^2 w^2 + v_{23}^2 t^2 \right)$$

for an orthorhombic beam where v_{12} and v_{23} are Poisson's ratios defined in terms of the elements of the compliance matrix by $v_{12}/E_a = -s_{12}$ and $v_{23}/E_c = -s_{23}$.

Before going on to describe some of the experimental results we first discuss a more drastic approximation to the elastic symmetry of TTF-TCNQ. This approximation will be useful later on in obtaining an estimate for the bulk modulus from the experimental data. The salient feature of the TTF-TCNQ structure is the linear stacking of the molecules along the

b direction. Accordingly one might expect the elastic properties to be different depending on whether the strain is parallel or perpendicular to the molecular stacks. The highest symmetry crystal system for which this distinction is possible is the hexagonal system, in which there are five independent elastic constants. A crystal belonging to the orthorhombic system will have hexagonal symmetry if two of the orthorhombic symmetry directions are equivalent. This relationship implies that when b is the preferred direction in a hexagonal material, the a c plane is elastically isotropic. A necessary condition for the hexagonal symmetry to be a good approximation is that the difference between the a and c axis Young's moduli be small, at least compared to the difference between the a and b axis Young's moduli. The idea that the a and c directions are approximately equal by comparison, is supported by recent room temperature compressibility measurements (Debray et al 1977) and thermal expansion data (Blessing and Coppens 1974). In conclusion a hexagonal model is the simplest approximation to the structure of TTF-TCNQ that still includes the essential anisotropy of the material.

2.2 Interpretation of Experimental Mode Spectrum

The expressions derived in the previous section for the vibration frequencies of elongated plates will be used to interpret the experimental mode spectrum of TTF-TCNQ crystals. As we have already pointed out there are severe mathematical difficulties in calculating the vibration frequencies of a rectangular resonator made of a monoclinic

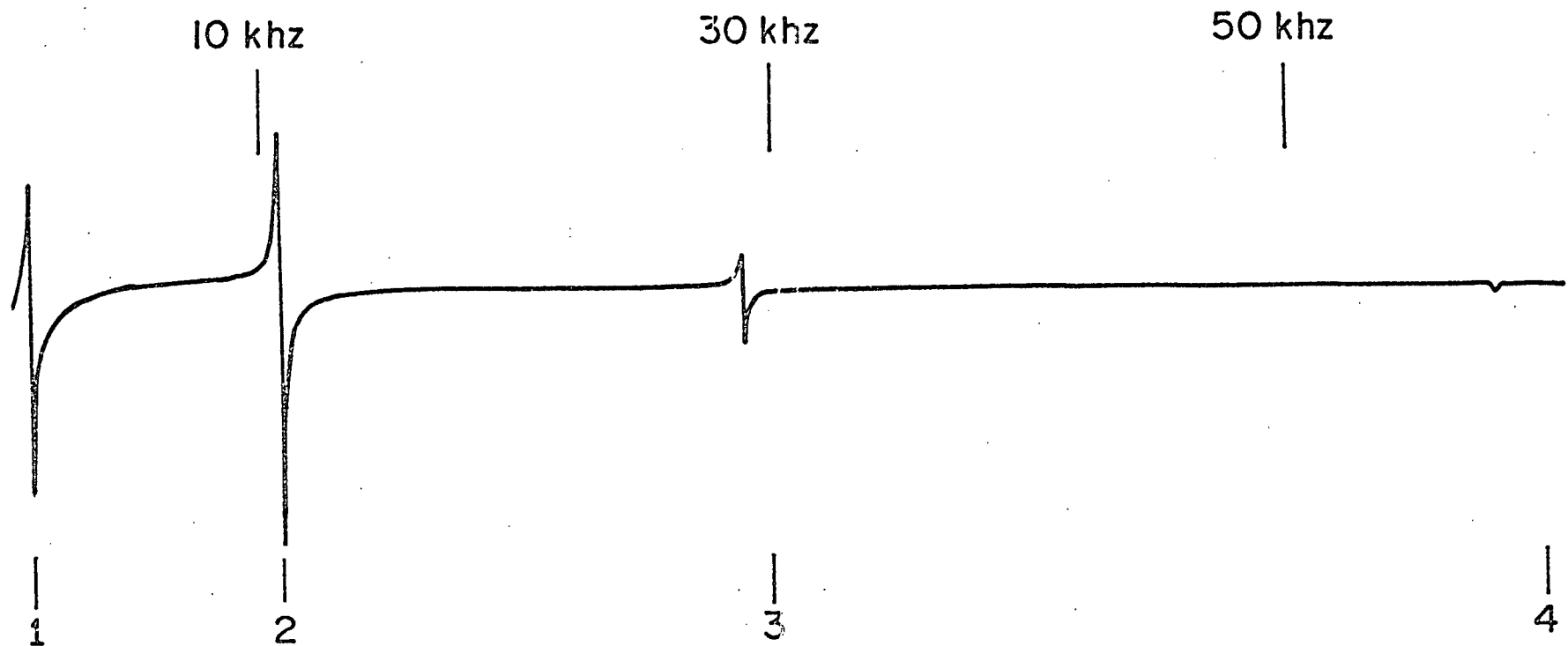


Fig. 34 - Experimental flexural mode spectrum. The numbered marks below the experimental trace indicate the frequencies of the flexural modes computed from [2] using the measured sample dimensions and a sound velocity to fit the second flexural mode. The noise level is comparable to the thickness of the line.

material. However, a more serious practical limitation to the accurate calculation of the resonant frequencies is the somewhat irregular geometry of the available TTF-TCNQ crystals. For example, the sample thickness (c^* dimension) which is normally the least uniform dimension, typically tapers off substantially near the ends. If the ends are cut off with a razor blade a good crystal will not vary in thickness by more than about 10% over its length. In addition, the silver paint clamp on the end of the sample in the vibrating reed configuration, is neither perfectly rigid nor perfectly uniform. Similarly the central support point for the longitudinally mounted samples perturbs the free-free boundary conditions. For all of these reasons we expect to see deviations from the idealized resonance frequencies given in Section 2.1 above.

(i) Vibrating Reed Support

The vibrating reed support configuration was used to study flexural and torsional modes. An experimental flexural mode spectrum is given in Fig.3⁴, which shows the first four F_{bc} flexural modes along with a theoretical spectrum obtained from [2] by adjusting the Young's modulus to fit the second experimental flexural mode. The first resonance in Fig.3⁴ appears to be weaker than the second one because it has a lower Q (see Section 2.3 below) and the amplifier gain is smaller at low frequencies. The resonance lines are antisymmetric because the phase of the reference input to the mixer has been set to detect the component of the sample response which is out of phase with the driving force.

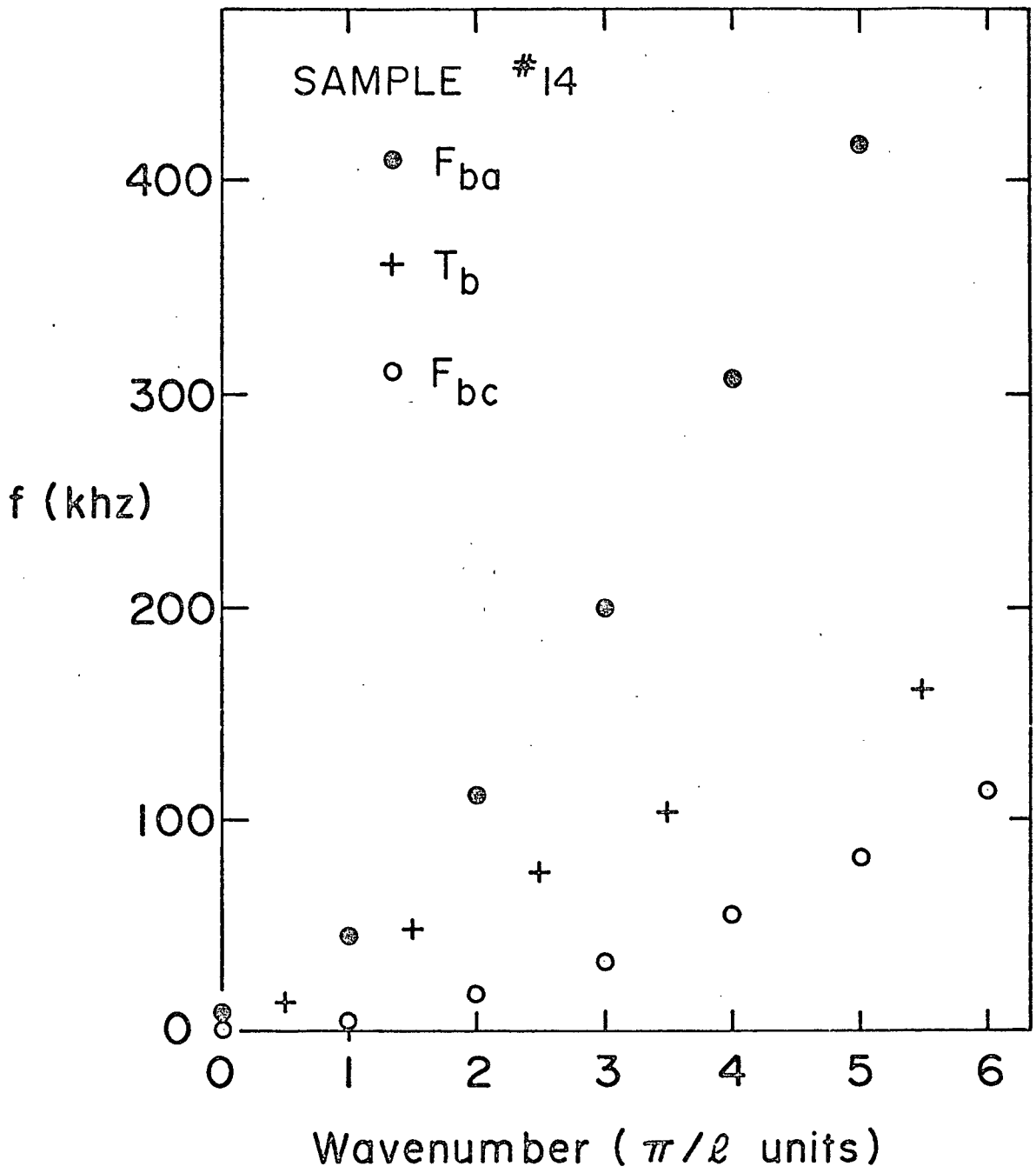


Fig. 35 - Low frequency flexural and torsional modes of a vibrating reed.

By increasing the system gain, it was possible to see the next five harmonics in the series shown in Fig.34. In addition, six low frequency T_b torsional and F_{ba} flexural modes were identified. By analogy with the continuous dispersion curves for acoustic waves propagating along an infinitely long sample, dispersion curves can also be plotted for the modes of a finite length sample as a series of discrete points. The low frequency mode dispersion diagram for a sample in the vibrating reed configuration is shown in Fig.35. In addition to the modes plotted in Fig.35, a large number of unidentified higher frequency modes are observed experimentally up to about 1 MHz.

Three pieces of information are helpful in identifying the various flexural and torsional modes. First, the torsional modes can be separated from the flexural modes by their temperature dependences. The torsional mode frequencies depend on a shear velocity which has a weaker temperature dependence than the Young's modulus velocity which determines the flexural frequencies (see Chapter III below). Secondly, the two different types of flexural modes (F_{ba} and F_{bc}) may be distinguished by the way they couple to the drive and detector electrodes. For example the F_{ba} flexural modes are preferentially excited if the axis of the drive and detector electrodes is aligned parallel to the a axis. Needless to say, no matter which type of mode is preferentially excited it is almost impossible to avoid a slight excitation of all the other types of modes through non-ideal sample and electrode geometry. Finally, once the modes have been

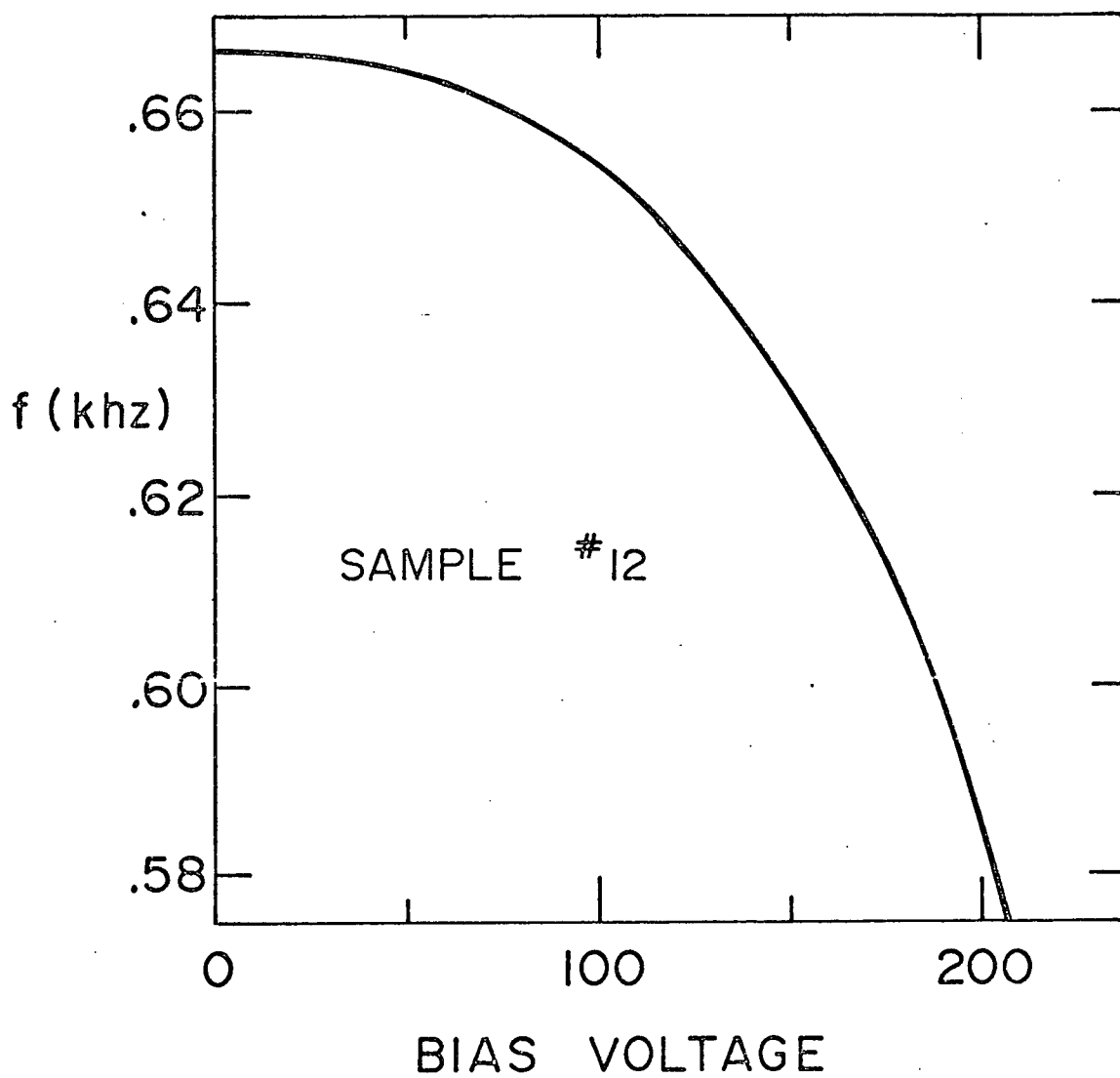


Fig. 36 - Effect of d.c. bias voltage on fundamental F_{bc} flexural mode resonance frequency.

identified as F_{ba} , F_{bc} or T_b , the frequency equations [2] and [5] can be used to assign harmonic numbers and as a check on the F_{ba} , F_{bc} and T_b identification.

The resonance frequencies of a thin vibrating reed can be artificially reduced if a large d.c. bias voltage is applied to the drive or detector electrodes (Barmatz and Chen 1974). Because of the d^{-2} dependence of the force on the plates of a charged parallel plate capacitor, the spring constant for a bent reed will have an electrical component as well as an elastic component. In the technique described here no d.c. bias field is required on the detector capacitor. However, a d.c. bias is used at the drive electrode to increase the driving force on the sample. The effect of this bias voltage on the frequency of the fundamental F_{bc} flexural mode is shown in Fig.36. The d.c. field has a much smaller effect on the torsional and higher harmonic flexural modes.

As long as the long axis of the reed is aligned parallel with the crystallographic b axis, the low frequency modes give no information about the Young's moduli perpendicular to the b axis. In order to measure the a axis Young's modulus, thin slices were cut off the end of normal TTF-TCNQ crystals perpendicular to the b axis. The shape of the four slices studied experimentally ranged from nearly square to rectangular with the a dimension twice as long as the b dimension. One end (bc^* plane) of the sample was glued to a support to produce a small vibrating reed with its long axis in the a direction. Only the first three or four modes could be confidently interpreted in

terms of the mode patterns shown in Fig.31 of Section 2.1 (iii) above. The first and third resonances are F_{ac} flexural modes, whose frequencies are determined by the a axis Young's modulus E_a as outlined in Table IV. Section 2.1 (v) above. Similarly, the second mode is a T_a torsional mode whose frequency is determined by the shear modulus c_{66} as indicated in eqn. [11]. The measured sound velocities are summarized in Table IV.

The signal to noise ratio for the fundamental flexural mode was greater than 100 with a 1 Hz noise bandwidth even for the smallest sample studied, which was a $2\mu\text{g}$, 0.3 mm long slice. Since the a axis samples were significantly less uniform than the bigger b axis samples the experimental value for E_a is not as accurate as the experimental value for E_b .

Another experimental difficulty arose on cooling the a axis samples. Unless the length (a dimension) of the sample was significantly bigger than its width (b dimension), differential thermal contraction of the bond at the end would split the sample in half along its length. Thermal cracking of the sample shows up as a large irreproducible discontinuity in the temperature dependence of the resonance frequency, and in a splitting of a single resonance line into a doublet or multiplet. The thermally induced cracks are visible if the crystal is examined under a microscope. Of the four a axis vibrating reeds measured only one would cycle down to helium temperature and back to room temperature without breaking. It is possible that some small fractures were also produced near the bond in the longer b axis vibrating reed samples during thermal cycling.

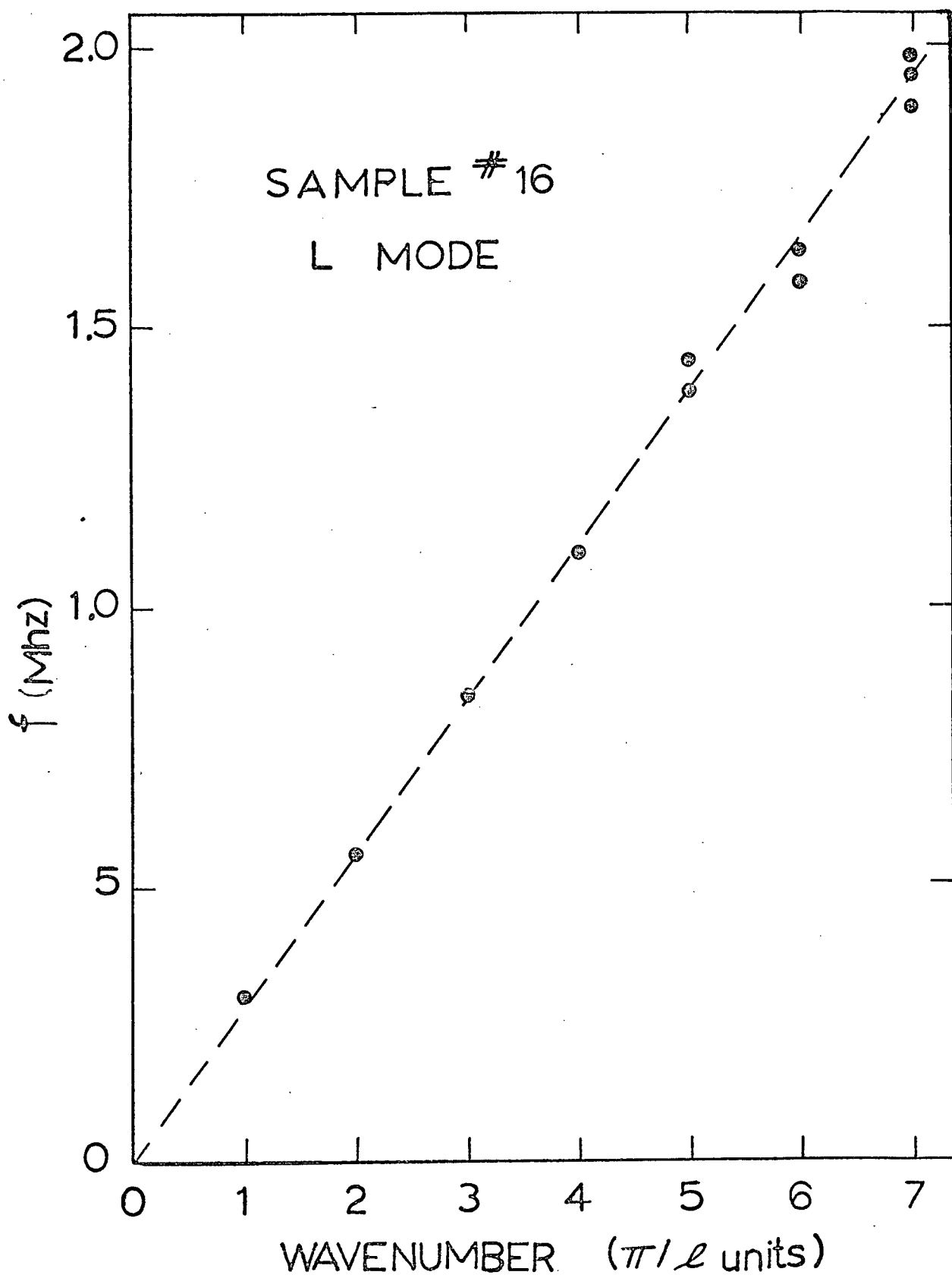


Fig. 37 - Longitudinal mode dispersion

(ii) Central Pin Support

The problems with differential thermal contraction may be largely avoided if the sample is supported by a very small silver paint contact on the end of a pointed wire, as described in Chapter 1, Section 1.1 (ii). This support configuration is a favourable one for exciting elongational acoustic modes in the sample. For a long sample with a uniform cross-section, the elongational resonance frequencies are given by [8] provided one ignores the small pin contact at the centre of the broad a b face of the sample. This approximation is expected to be best for the odd numbered modes since these modes have a node at the support pin. If the experimental elongational mode frequencies are plotted as a function of the wavenumber $2\pi n/\ell$, where ℓ is the length of the sample, then one obtains the discrete dispersion curve shown in Fig.37. Eqn.[8] predicts a linear dependence of the resonance frequency on wavenumber. A close examination of Fig.37 reveals that the even harmonics are slightly below the straight line and the odd harmonics are slightly above the straight line. In addition, the even harmonics tend to be more heavily damped than the odd harmonics. We attribute these differences between the even and odd harmonics to the effect of the central pin support. The effect of the finite length correction factor [9] (or [12]) is to reduce the frequency of the seventh harmonic by 1-2%.

Beyond the fourth harmonic, more than one frequency is plotted in Fig.37 for each wavenumber. The reason for the multiplicity is that there are several modes of nearly equal strength near the frequency where a longitudinal resonance should be. Presumably, as the wave-

length of the longitudinal mode becomes shorter, the non-uniformities in the sample dimensions become progressively more important and the longitudinal modes are coupled more strongly to other acoustic cavity modes. The other acoustic modes which could be coupled to the longitudinal modes are high frequency harmonics of the b axis flexural and torsional modes and transverse F_{ac} type flexural modes. Moreover, the sample whose longitudinal resonance frequencies are shown in Fig. 37 begins to support transverse shear wave resonances at frequencies corresponding to $n \geq 7$. Above 2 MHz the acoustic mode spectrum degenerates into a closely spaced set of heavily damped resonances. Of course all of these modes are affected in some complicated way by the central support. This complexity of the high frequency acoustic mode spectrum provides a practical upper limit to the frequency range for which the acoustic resonance method is useful. The measurements could probably be extended to higher frequencies by studying acoustic pulse propagation along the sample rather than looking at resonances.

A comparison of eqns. [2] and [8] in light of the discussion on the crystalline anisotropy in Section 2.1 (v) above, reveals that the elongational and b axis flexural resonance frequencies are determined by the same elastic constant to first approximation - namely E_b . The Young's modulus velocity $(E_b/\rho)^{1/2}$ has been measured for eight TTF-TCNQ samples by substituting the experimentally determined flexural and longitudinal resonance frequencies into [2] and [8] respectively. Within our experimental error there is no systematic softening of the F_{bc} type flexural modes as would be expected from [3], if the shear modulus c_{44} were anomalously small as has been suggested by

Barmatz et al (1974) and Ishiguro et al (1977). The shear softening of the higher frequency F_{ba} type modes is consistent with the shear modulus c_{66} that is determined from the torsional modes.

Even though the flexural modes can be used to determine the same extensional velocity $(E_b/\rho)^{\frac{1}{2}}$ as the longitudinal mode, the longitudinal one generally gives a more accurate estimate of this velocity. The reason is that the longitudinal resonance is less sensitive to variations in the sample thickness (c^* dimension) which is the least uniform dimension. The room temperature sound velocities as determined from the acoustic resonance frequencies of fifteen different samples, are summarized in Table V. The b axis extensional velocity $(E_b/\rho)^{\frac{1}{2}}$ and the shear velocity $(c_{66}/\rho)^{\frac{1}{2}}$ are consistent with inelastic neutron scattering measurements of Shapiro et al (1977). The a axis extensional velocity $(E_a/\rho)^{\frac{1}{2}}$ is consistent with recent compressibility measurements of Debray et al (1977). The detailed temperature dependence of these velocities is discussed in the next chapter.

TABLE V

Room Temperature Sound Velocities in TTF-TCNQ

Mode	Velocity (10^5 cm/s)
b axis extensional	$2.8 \pm .1$
a axis extensional	$4.4 \pm .5$
c_{66} shear	$1.7 \pm .2$

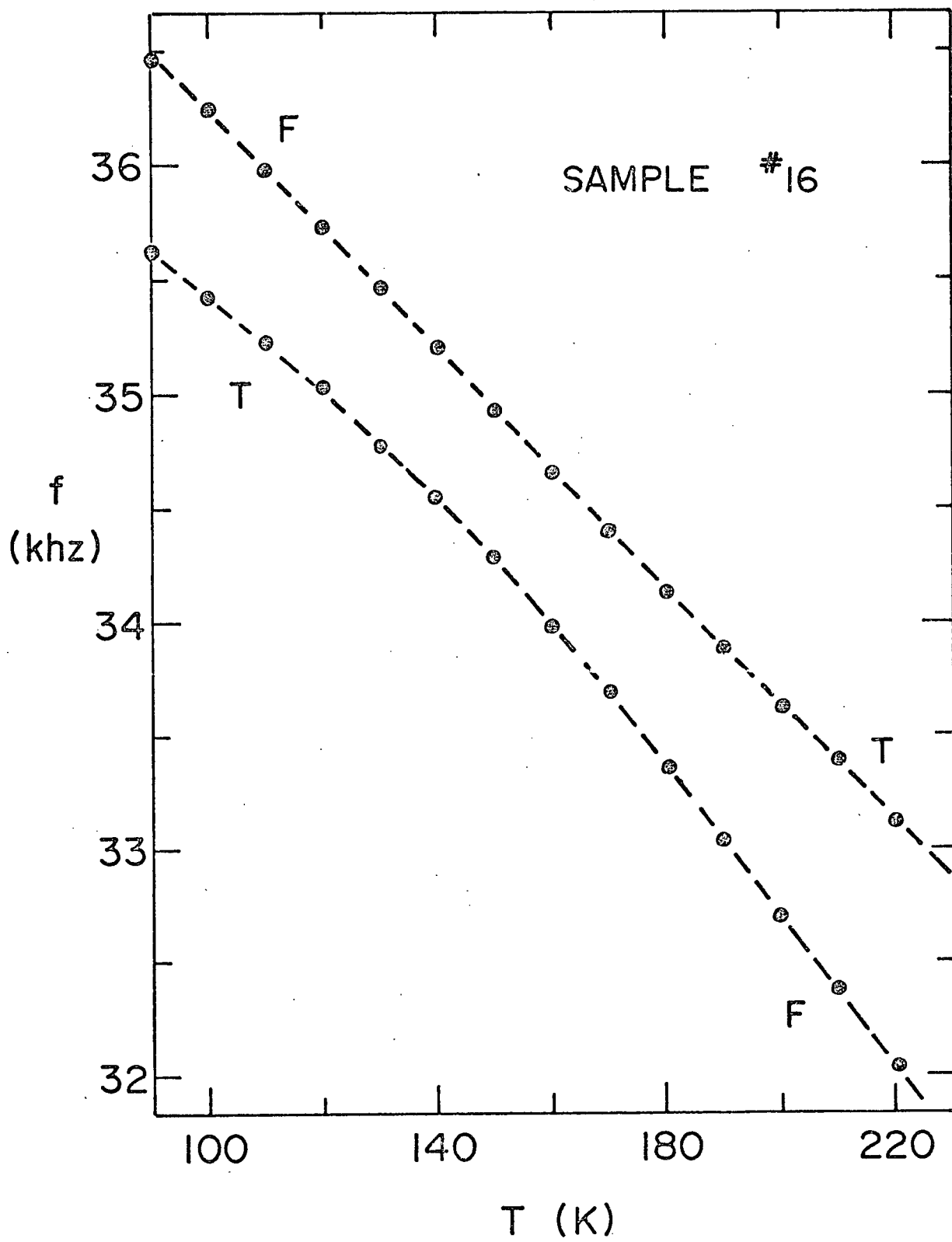


Fig. 38 - Flexural and torsional mode crossing

(iii) Mode Coupling

Before going on to discuss the temperature dependence of the sound velocities in detail, we first outline some of the effects of extraneous mode coupling on the temperature dependence of the resonance frequencies. As pointed out in the next chapter, the b axis Young's modulus velocity has a stronger temperature dependence than the shear velocity. For this reason, if a mode which depends on the Young's modulus is at nearly the same frequency as a torsional mode at one temperature the two modes may cross as the temperature is changed. A mode crossing of this type is shown in Fig. 38. The torsional mode starts off just above a nearby flexural mode at high temperatures. As the temperature is lowered the frequency of the torsional mode moves below the flexural mode because of the difference in their temperature dependences. Coupling between the two modes prevents them from actually intersecting. The coupling could be caused by the off diagonal component s_{26} in the monoclinic compliance matrix (Hearmon 1961) or by asymmetry in the sample or support. The torsional mode in Fig. 38 is the fundamental torsional mode and the flexural mode is probably a symmetric F_{bc} type flexural mode with three nodes. These resonances were observed with the sample supported in the longitudinal mode configuration.

Mode coupling can be a problem in making accurate measurements of the temperature dependence of the sound velocity. The problem seems to be particularly severe for elongational modes in the temperature range between 20K and 52K, where the Young's modulus has an anomalously strong temperature dependence compared with the shear modulus (see next chapter).

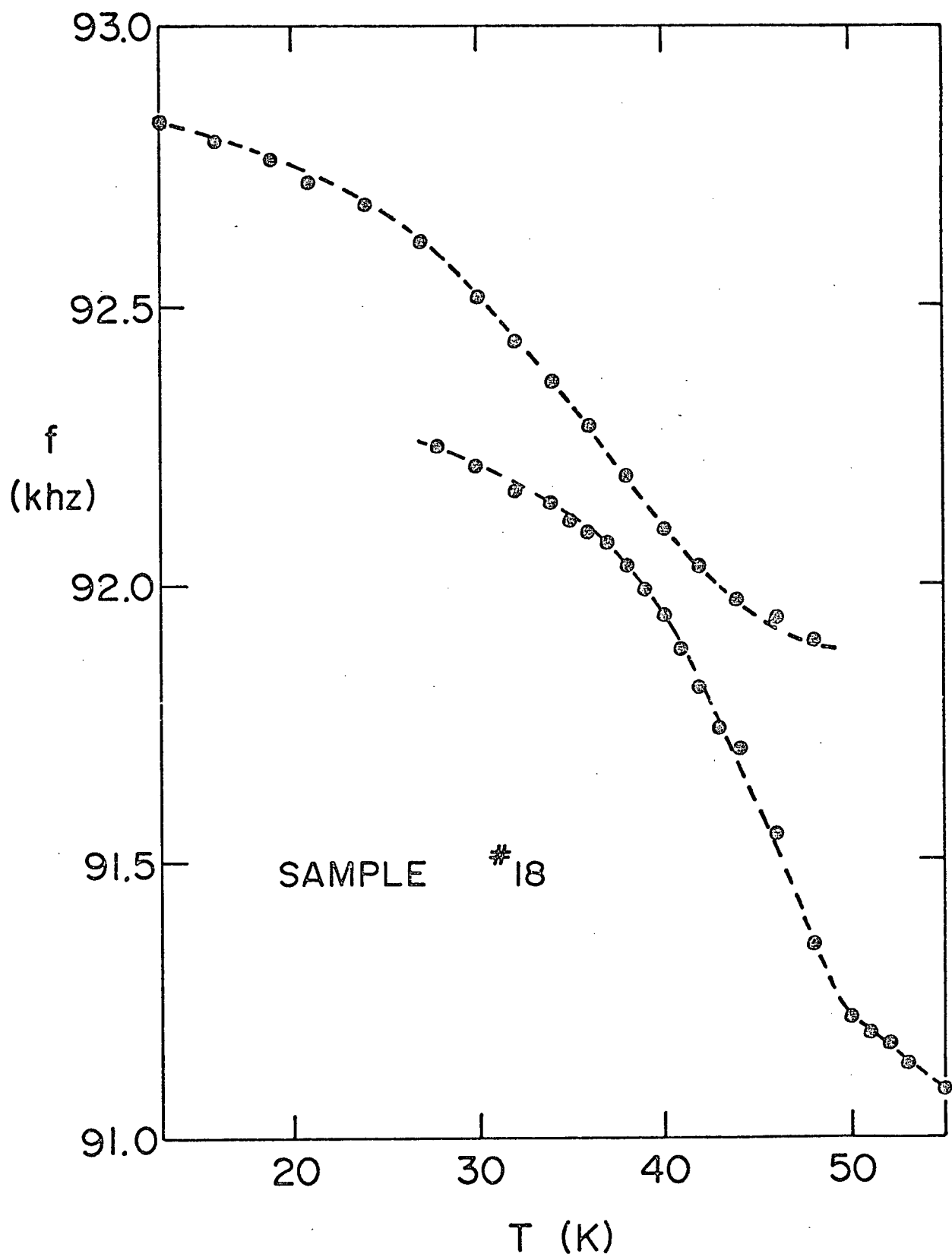


Fig. 39 - F_{ac} flexural mode with interference from an unidentified mode of the support

The strong temperature dependence makes it more likely that the resonance of interest will cross some other mode with a weaker temperature dependence. Fig. 39 shows a typical mode crossing of this type. Here an F_{ac} type mode is crossed near 39K by an unidentified mode, that is probably related to the support.

(iv) Support Modes

It is virtually impossible to avoid some interference with the sample resonances from the modes of the support. However, it is possible to avoid support modes over a limited frequency range. For example no support modes were observed among the low frequency flexural and torsional modes of b axis crystals clamped in the vibrating reed configuration. On the other hand, as illustrated in Fig. 39 there were some problems with interference with the flexural modes of the a axis slices probably because these modes were at higher frequencies. Interference from the modes of the tungsten support wire for the longitudinally mounted samples, was alleviated by using a thick support post (0.015" diameter) so that the support modes were widely spaced and at relatively high frequencies. In any case the sample modes and support modes can be easily distinguished at high temperatures, by the dramatic difference in their temperature dependences.

2.3 Vibration Damping

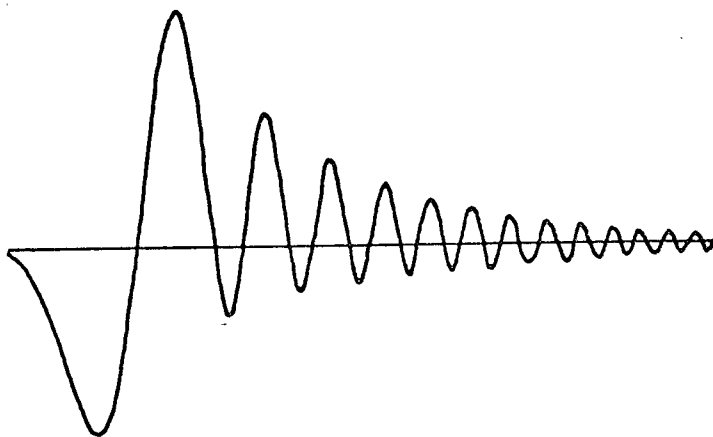
(i) Q Measurement

The acoustic resonances can be used to determine the absorption of sound as well as the velocity of sound. The absorption is proportional

to the width of the resonance line. A convenient measure of the absorption is the quality factor Q defined by $Q^{-1} = \Delta f/f$ where f is the resonance frequency and Δf is the "full width at half maximum" of the symmetric (in phase) amplitude response. Equivalently Δf is the separation between extrema in the antisymmetric (out of phase) resonant response. The Q is related to the intensity attenuation factor α discussed in Part A above by $\alpha = Q^{-1}q$ where q is the sound wavenumber.

The Q was measured experimentally by comparing the symmetric response of the sample with a synthetic lorentzian on a dual beam oscilloscope. The synthetic lorentzian was generated by sweeping a voltage controlled oscillator through the resonance frequency of a tuned circuit ($Q \sim 70$) as shown in the circuit diagram in Appendix § 1.(v). By adjusting the amplitude of the frequency sweep of the voltage controlled oscillator, the apparent width of the synthetic line could be adjusted to match the width of the sample resonance. After calibration the synthetic lorentzian provided a convenient means for measuring linewidth to a relative accuracy of 1%.

In order to make accurate linewidth measurements one must be careful to avoid distorting the sample resonance lines. For example if the drive oscillator is swept too quickly through the acoustic resonance, a ringing phenomena known in NMR as "wiggles" (Abragam 1961) will occur. An extreme example of wiggles is shown in Fig. 40.



Horizontal scale: 1 Hz/cm

Sweep rate: 3.3 Hz/s

Fig. 40 - Wiggles

(ii) Thermoelastic Damping

Heat conduction is an important loss mechanism for the low frequency flexural modes of TTF-TCNQ crystals. As discussed by Zener (1948) and Bhatia (1967), whenever the isothermal and adiabatic elastic moduli (see Chapter III) are not equal, thermal conduction between compressions and rarefactions will cause acoustic damping. In conventional metals thermal conduction does not cause significant damping of longitudinal waves at frequencies below about 10 GHz. However, the damping can be substantial for flexural modes of thin plates where the compressed part of the plate is close to the expanded part.

The thermoelastic damping of a flexural resonance of a reed with a rectangular crosssection is given by (Bhatia 1967)

$$[13] \quad Q^{-1} \approx \frac{E_S - E_T}{E_S} \frac{ff_0}{f^2 + f_0^2}, \quad f_0 = \frac{\pi}{2} \frac{D}{t^2}$$

where E_S and E_T are the adiabatic and isothermal Young's moduli respectively, f is the resonance frequency and t is the reed thickness, measured along c^* for the F_{bc} modes. The thermal diffusivity D is the ratio of the thermal conductivity κ to the specific heat at constant volume, C_V . To obtain a numerical estimate for the absorption we approximate $(E_S - E_T)/E_S$ by $(B_S - B_T)/B_S$ where B_S (B_T) is the adiabatic (isothermal) bulk modulus, and use $B_T/B_S = C_V/C_P$ derived by Bhatia (1967) (see also eqn. [2] in Chapter III below). With the expression for the difference between C_P and C_V given by Landau and Lifshitz (1969) and using the Grüneisen approximation discussed in Section 3.1 of Chapter III below, we obtain

$$[14] \quad \frac{E_S - E_T}{E_S} \approx \frac{C_P - C_V}{C_P} = \gamma\alpha T$$

where $\gamma \sim 2.6$ is a Grüneisen constant and α is the volume expansion coefficient.

From eqns [13] and [14] we can estimate Q^{-1} for the flexural modes using published thermal expansion (Schafer et al 1975, Blessing and Coppens 1974), b axis thermal conductivity (Salamon et al 1975) and specific heat data (Craven et al 1974). For example, consider Sample #13 which was 0.038 mm thick and had its fundamental flexural resonance

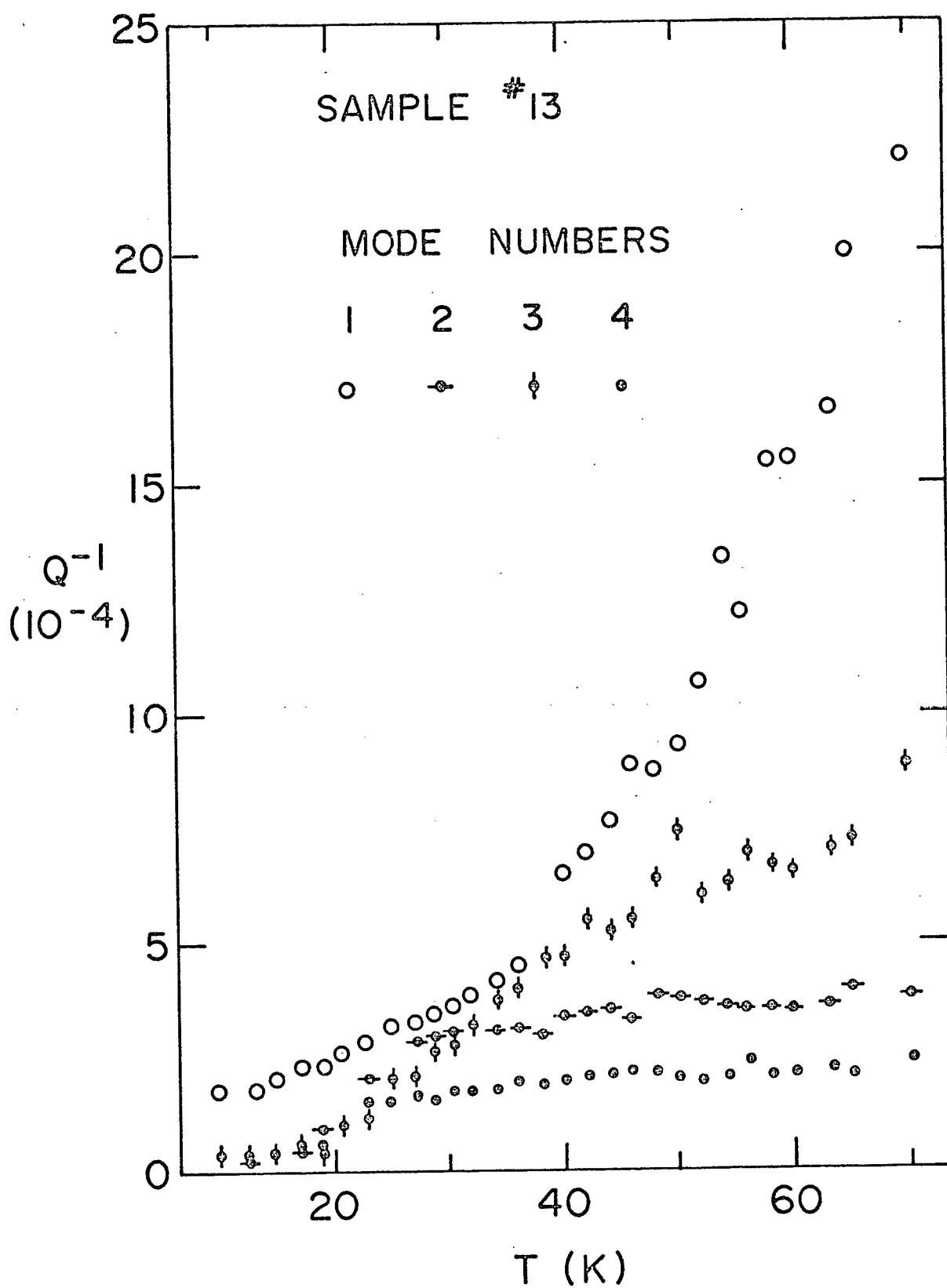


Fig. 41 - Damping of first four F_{bc} flexural modes

at 2.1 khz. For this mode we estimate $Q^{-1} = 8 \times 10^{-4}$ using a thermal relaxation frequency $f_0 = 21$ khz. The experimentally determined absorption is shown in Fig. 41 as a function of temperature for the first four F_{bc} flexural modes. Although the estimated value of Q^{-1} at 55K of 8×10^{-4} is close to the measured value of 13×10^{-4} for the fundamental flexural mode at 55K, the dependence of the damping on the flexural mode frequency is wrong. With $f_0 = 21$ khz in [13] the absorption will be larger for the second flexural mode whereas experimentally it is observed to be smaller. In addition, above 55K the damping of the second, third and fourth harmonics is only weakly temperature dependent (see Fig. 41).

To help explain these features of the experimental data we make the following observations. First the thermal relaxation rate f_0 will increase with decreasing temperature at least as fast as T^{-1} . This temperature dependence should be valid down to 30K, at least. Secondly $\gamma \alpha T f_0$ will be a weak function of temperature. The experimental data in Fig. 41 may now be accounted for qualitatively by postulating that f_0 satisfies $f_1 < f_0 < f_2$ where $f_1(f_2)$ are the first (second) flexural resonance frequencies. Furthermore, if we observe that the damping is nearly equal for the first two modes at 40K, we can estimate f_0 at this temperature. This estimate for f_0 (5 khz) implies that the thermal conductivity in the c^* direction is 0.02 W/cm-K. This value compares with 0.12 wa/cm-K for the b axis thermal conductivity measured by Salamon et al (1975) at the same temperature. Similarly $f_0 = 5$ khz implies that $Q^{-1} = 12 \times 10^{-4}$

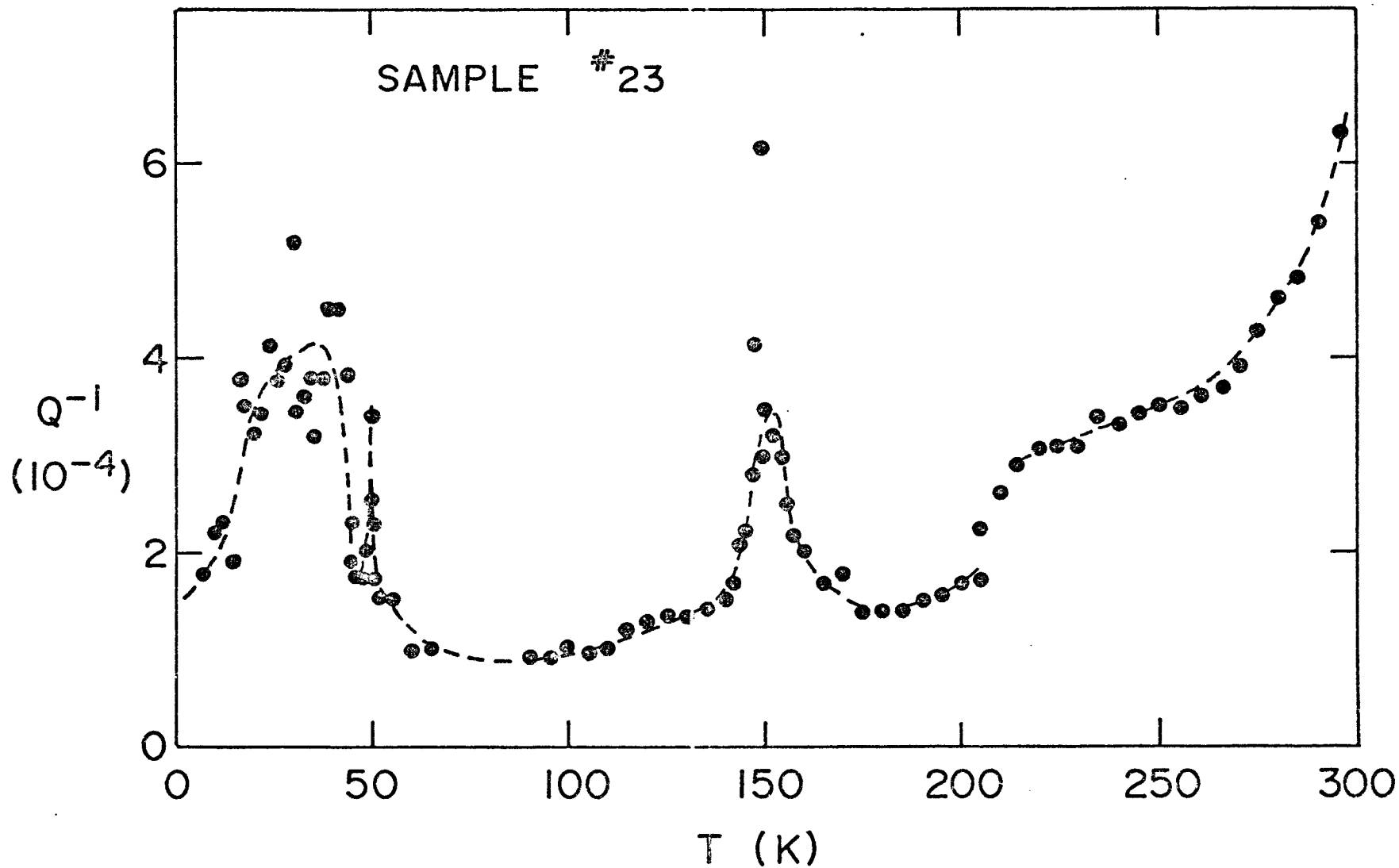


Fig. 42 - Damping of fundamental longitudinal mode. The discontinuity at 205K arose when a measurement was repeated after allowing the sample to remain at low temperatures overnight.

at 40K, which is about a factor of two bigger than the observed absorption. Clearly, all of these calculations are very rough. Nevertheless, one can conclude that thermal conduction will have a significant effect on the damping of the flexural modes. It should be possible to determine the transverse thermal diffusivity, by careful measurements of the damping of flexural modes. Finally, we note that thermoelastic damping may account for the anomalous frequency dependence observed by Barmatz et al (1975) in the damping of flexural modes in 2H-TaSe₂.

(iii) Elongational Modes

The room temperature damping of the fundamental elongational mode in TTF-TCNQ is typically an order of magnitude smaller than the room temperature damping of the fundamental flexural mode. In addition the absorption for the elongational modes increases with harmonic number unlike the first few flexural modes. The temperature dependence of the acoustic absorption for the fundamental longitudinal mode of Sample #23 is shown in Fig. 42. Although the magnitude and detailed temperature dependence of the experimentally observed longitudinal mode damping are not completely reproducible between different samples and different runs with the same sample, certain gross features are always present. There is a broad minimum in the vicinity of 60K where $Q \sim 10^4$. As the sample is cooled through the metal insulator transition the absorption begins to increase, reaching a peak in the range 30-40K where it is a factor of 3-6 times larger than the absorption near 60K. As the temperature is lowered still further the absorption decreases again.

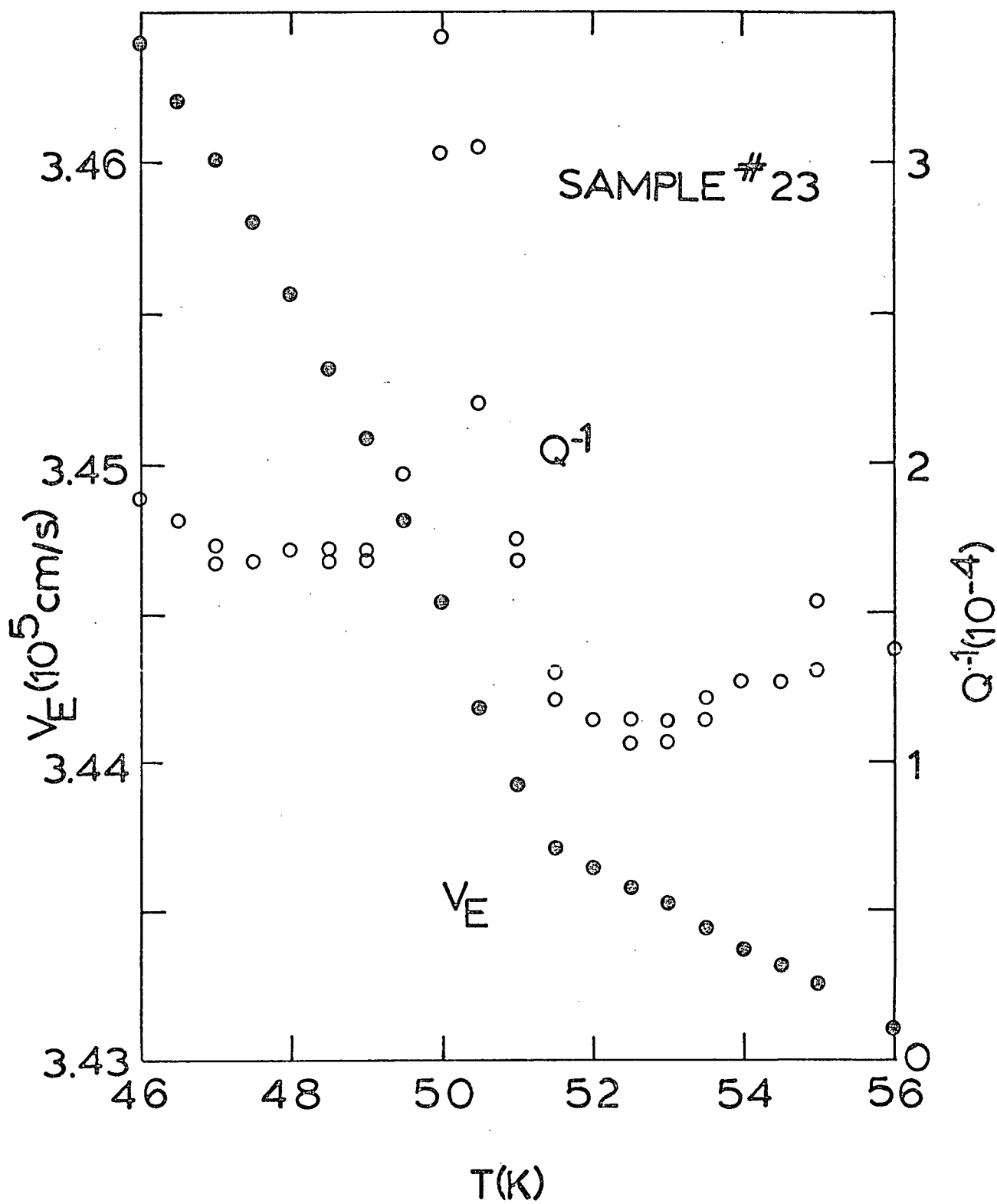


Fig. 43 - Sound velocity and attenuation near the metal-insulator transition

In Sample #23 there is also a 10K wide absorption peak near 150K and a very narrow ($< 0.5\text{K}$ wide) peak in the damping just below the metal-insulator transition. The details of the temperature dependence of the damping and the velocity of sound near the metal-insulator transition are shown in Fig. 43. The temperature dependence of the velocity of sound is discussed in detail in the next chapter. Although neither the narrow absorption peak near the transition nor the wider maximum near 150K were observed in any other sample, it is quite possible that they were missed by not taking measurements at fine enough temperature intervals. The absorption peak near the metal-insulator transition is reminiscent of a similar feature observed near the incommensurate charge density wave transition in 2H-TaSe_2 by Barmatz et al (1975). Although the peak near 150K may be due to some extraneous effect, it is tempting to try to relate it to the disappearance of the $2k_F$ scattering of diffuse X-rays, observed by Khanna et al (1977) near 150K.

An upper limit to the conventional electronic contribution to the absorption can be obtained by using the expressions derived in Part A, Chapter I, for the attenuation of sound in three dimensional metals, or the expression for the peak attenuation just below the metal-semiconductor transition, discussed in Part A, Section 2.3. From the bandstructure (Berlinsky et al 1974), d.c. conductivity, and crystal structure we estimate the electronic effective mass $m^* = 6 m_0$, the Fermi velocity $v_F \sim 10^7 \text{ cm/s}$, the electronic scattering time $\tau \sim 5 \times 10^{-14} \text{ s}$ at 60K and the carrier density $n = 2.8 \times 10^{21} \text{ cm}^{-3}$.

With these values for the material parameters, the electronic contribution to the damping of a 300 khz longitudinal mode is calculated to be $Q^{-1} \sim 10^{-9}$. Since the measured absorption is of order 10^{-4} , we conclude that the observed damping is not due to the conduction electron loss mechanism discussed in Part A. If TTF-TCNQ remained metallic at low temperatures it is possible that this electronic loss mechanism would eventually become important at low temperatures, as it does in ordinary metals.

Although thermal conduction is probably the dominant loss mechanism for the low frequency flexural modes, its contribution to the damping of the longitudinal modes is completely negligible. Dislocation damping (Bhatia 1967) and coupling to low Q support modes are probably important sources of loss for the longitudinal modes. An additional damping mechanism is suggested by the model used in the next chapter to explain the temperature dependence of the sound velocity. We comment on this loss mechanism at the end of the next chapter.

(iv) Effect of Air on Resonance Frequency and Q

Before going on to discuss the temperature dependence of the sound velocity in TTF-TCNQ we briefly outline the effect of air at one atmosphere on the resonant frequencies and Q of the vibrating sample. The shift in the resonant frequency is due to the mass of entrained air that accompanies the vibrating sample. When the sample vibration frequency is low enough that the corresponding wavelength of sound in air is long compared to the transverse (a) dimension of the

sample, the surrounding air may be treated as an incompressible non-viscous fluid. For typical TTF-TCNQ crystals this condition is well satisfied up to about 50 khz. In this limit the air entrained by an F_{bc} flexural mode may be approximated by a cylinder with its axis along b and its diameter equal to the width of the crystal, as shown in Fig. 44.

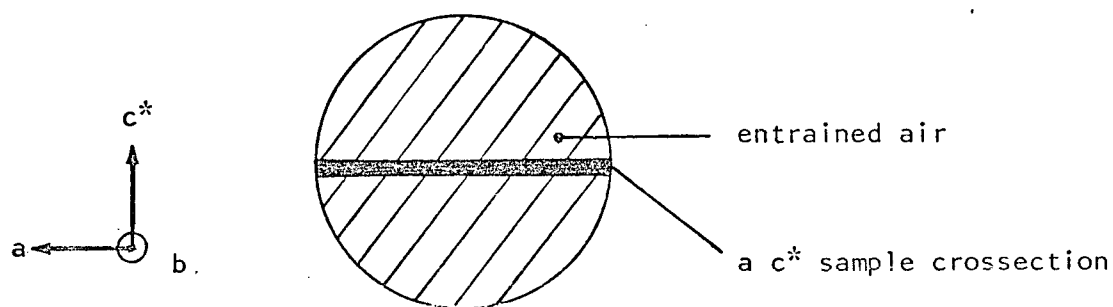


Fig.44 - Air Entrained by a Flexural Mode

It is easy to show that the effective increase in the mass of the sample per unit length leads to a reduction in the Flexural (F_{bc}) resonant frequency by the factor

$$[15] \quad \left(1 + \frac{\pi w \rho_{air}}{4 t \rho}\right)^{-1}$$

where ρ_{air} and ρ are the densities of air and the sample respectively. The same result has been obtained by Lindholm et al (1965) using a more sophisticated approach.

Lindholm et al (1965) also calculate the corresponding mass loading for torsional modes and obtain the correction factor

$$[16] \quad \left(1 + \frac{3\pi w \rho_{\text{air}}}{32 t \rho} \right)^{-1} .$$

This factor may be approximated by calculating the additional axial moment of inertia contributed by two cylinders of air parallel to the long axis of the sample (b) and with diameters equal to half the width of the sample as shown in Fig. 45. The resulting correction factor is

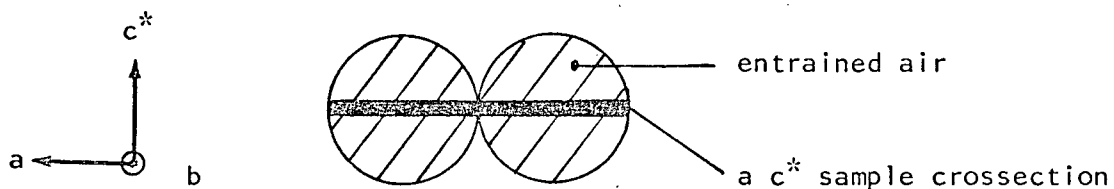


Fig.45 - Air Entrained by a Torsional Mode

the same as [16] except that the numerical factor $3\pi/32$ is replaced by $9\pi/64$.

The frequency shifts caused by air loading can be measured by looking for a change in resonance frequency when the sample chamber

is evacuated. For example consider Sample #14. A comparison between the observed effect of air on the resonance frequency and the predictions of [15] and [16] is shown in Table VI for the second and fifth F_{bc} flexural modes and the second and third T_b torsional modes. In Table VI the air is assumed to be at one atmosphere with density 0.00129 g/cm^3 . The observed frequency shifts are in reasonable agreement with the predicted values.

TABLE VI

Effect of Air at One Atmosphere on Flexural and Torsional Mode Frequencies

Mode	Frequency (khz)	Frequency Shift (hz)	
		Theory	Expt.
$F_{bc}2$	5.3	19	25
$F_{bc}5$	44.6	162	120
$T_b 2$	47.2	65	100
$T_b 3$	73.5	101	100

The elongational modes are at too high a frequency for the air to be treated as an incompressible non-viscous fluid. The primary source of air entrainment in a longitudinal mode is the viscous boundary layer which attaches itself to the broad ab surface of the crystal because of the non-zero viscosity of the air. The effective thickness of the boundary layer is $\delta/2$ (Landau and Lifshitz 1959) where $\delta = \left(2\eta/\omega\rho_{\text{air}}\right)^{\frac{1}{2}}$ is a skin depth for shear waves in a fluid with

viscosity η . If we take $\eta = 1.8 \times 10^{-4}$ poise ($\text{g/cm}^2\text{-s}$) at room temperature then $\delta/2 \sim 2 \times 10^{-4}$ cm for a 300 khz mode. This layer of air will reduce the resonant frequency of a 300 khz elongational mode by 12 Hz. Experimentally the change in resonance frequency is usually observed to be larger than 12 Hz. Furthermore the shift does not always have the same sign for different samples. This behaviour is interpreted as being due to a change in coupling between the elongational mode and other nearby modes caused by the increase in Q when the air is removed.

The Q of a lossless sample vibrating in air is determined by power loss due to viscous heating of the air and radiated acoustic energy. The air damping may be calculated approximately for standard size samples above 50 khz. In this case the viscous loss is relatively small compared to the radiation loss and the interior dimensions of the sample container are large compared to the sound wavelength, so that walls can be ignored.

First we consider the high frequency limit in which the wavelength of sound in air is small compared to both the a and b dimensions of the sample. This limit is applicable at typical longitudinal mode frequencies. The radiated sound power is given by

$$\Delta I = \rho_{\text{air}} v_s \overline{u_n^2} \Delta A$$

where v_s is the velocity of sound in air and u_n is the normal component of the velocity of the surface element ΔA . If we assume that the entire surface area generates sound, partly because of surface roughness

and partly because there may be coupled lateral motions of the sample, then $u_n \approx u$ and

$$[17] \quad Q \approx \frac{1}{2} \frac{\rho}{\rho_{\text{air}}} \frac{\omega t}{v_s}$$

where $Q/2\pi$ is defined as the energy stored divided by the energy dissipated per cycle. The actual air damped Q of Sample #10 was 176 whereas [17] predicts a Q of 143. In a vacuum the measured Q was 3100.

In the intermediate frequency range in which the sound wavelength in air is longer than the a dimension of the sample but still shorter than the b dimension, the sample may be modelled by an infinite cylinder with diameter w . The sound power radiated by an intermediate frequency flexural mode may be approximated by the power radiated by a transversely oscillating cylinder, given by (Landau and Lifshitz 1959)

$$I = \frac{\pi^2}{4} \rho_{\text{air}} \frac{\omega^3}{v_s^2} \left(\frac{w}{2}\right)^4 \overline{u^2}$$

per unit length where u is the velocity of the cylinder. The corresponding expression for the Q is

$$[18] \quad Q = \frac{16}{\pi^2} \frac{\rho}{\rho_{\text{air}}} \frac{v_s^2 t}{\omega^2 w^2} .$$

If we substitute values appropriate to the fifth F_{bc} flexural mode

(44.6 khz) of Sample #14, then [18] yields $Q = 993$. In the absence of air the observed Q is 1500. Adding this measured intrinsic loss to the calculated air loss leads to a net air damped Q of 597. This compares with an experimental value of 500.

Although our calculations of the effect of air on the damping and resonance frequencies of vibrating TTF-TCNQ samples are only approximate, the physical origin of the observed effects appear to be well understood.

CHAPTER III

Interpretation of Temperature Dependence of Sound Velocity

3.1 Overall Temperature Dependence

Before discussing the temperature dependence of the elastic moduli, we first compare the measured elastic constants (see Table V, in the previous chapter) and anisotropy of TTF-TCNQ with some common materials. Table VII contains a list of Young's moduli for covalent (Si), metallic (Au, Pb, Na), ionic (NaCl) and van der Waals (Ar) solids.

TABLE VII

Young's Moduli For Various Materials [†]

Material	Young's Modulus (10^{11} dynes/cm ²)	T(K)
Si	13.1	300
Au	4.65	0
NaCl	4.37	300
TTF-TCNQ a	4.3	0
b	2.0	0
Pb	2.05	0
Na	0.241	90
Ar	0.117	82

[†] Huntington (1958), Kittel (1971), Gewurtz et al (1972)

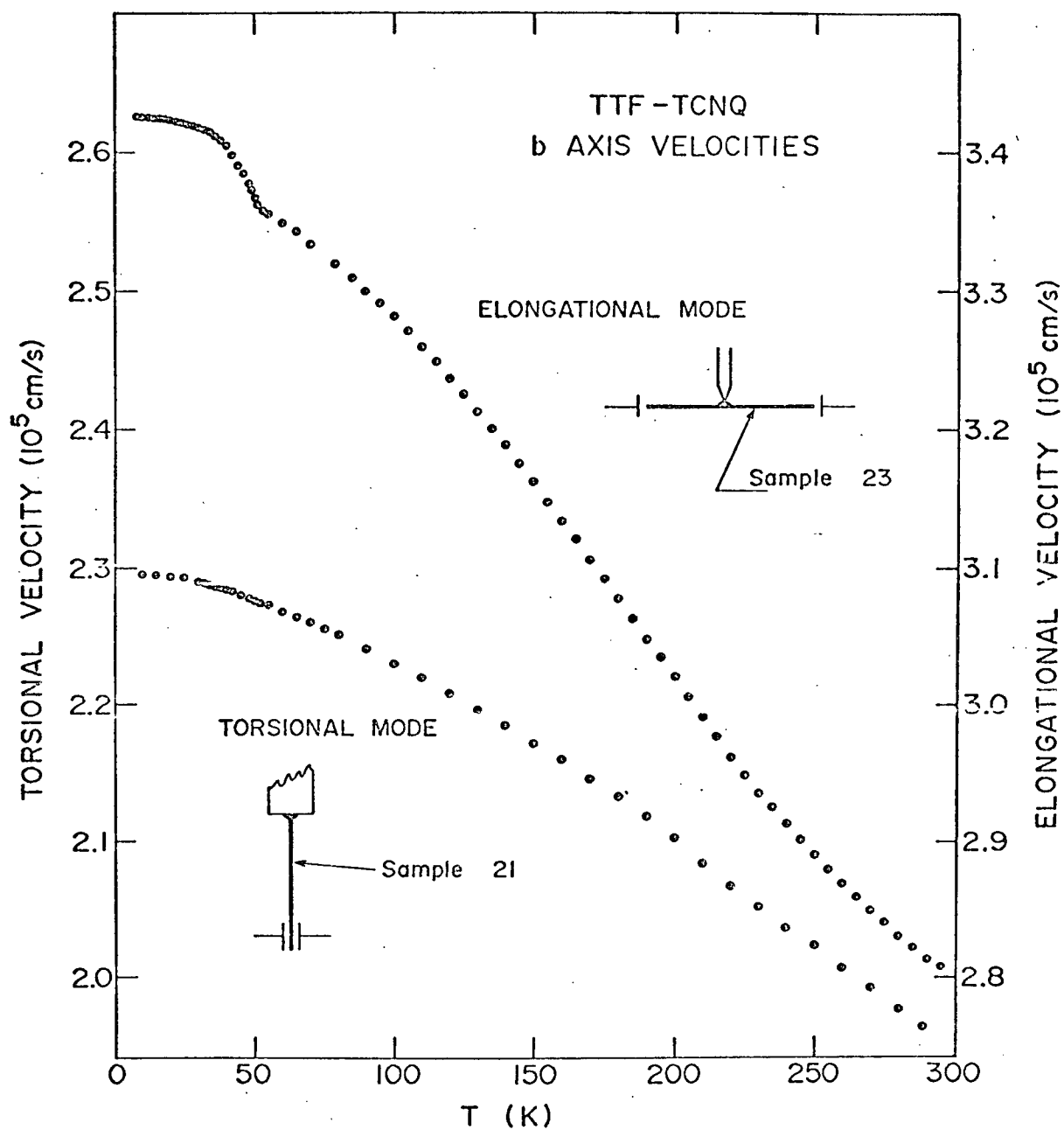


Fig. 46 - Temperature dependence of b axis elongational and torsional mode velocities

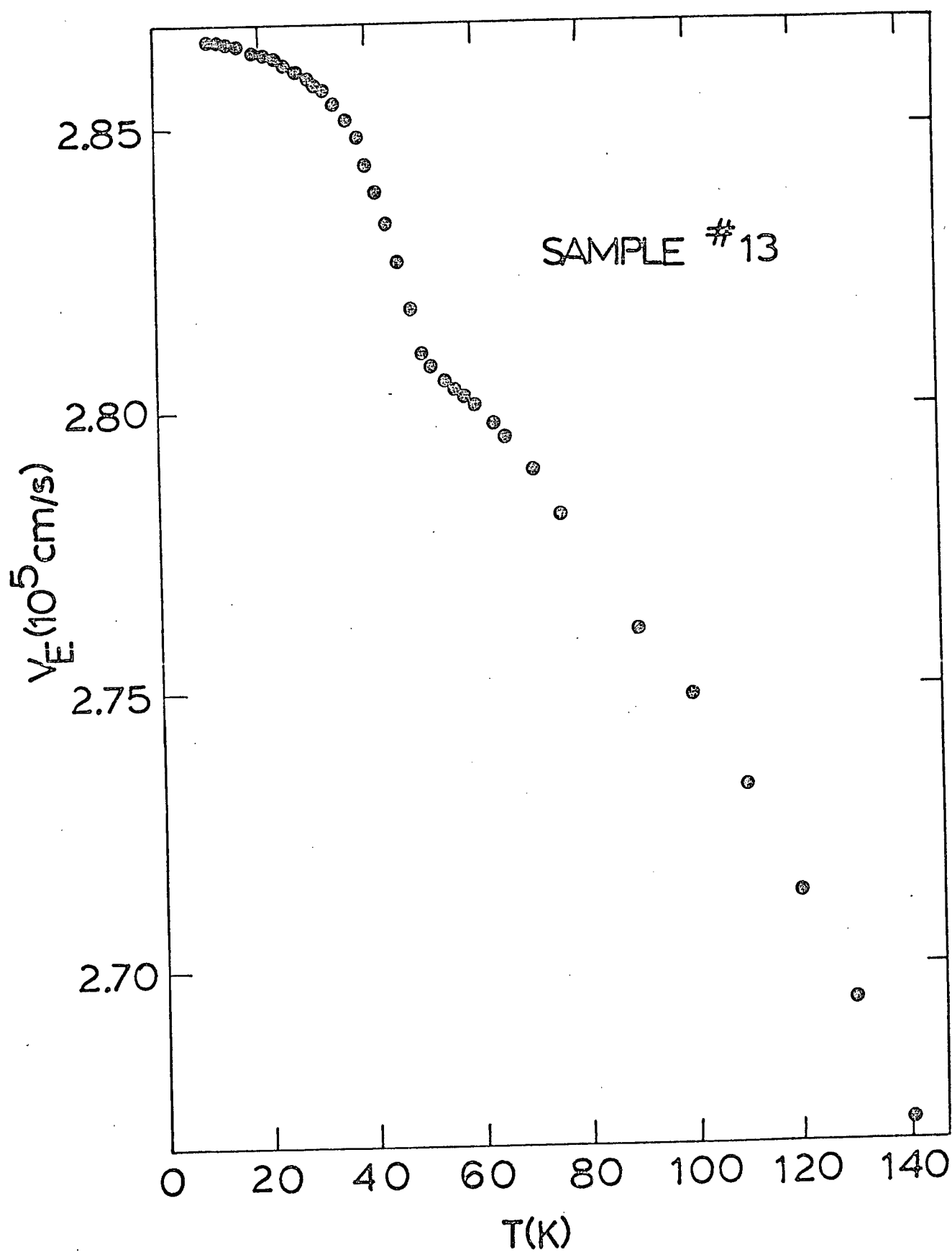


Fig. 47 - Temperature dependence of b axis Young's modulus velocity obtained from an F_{bc} mode

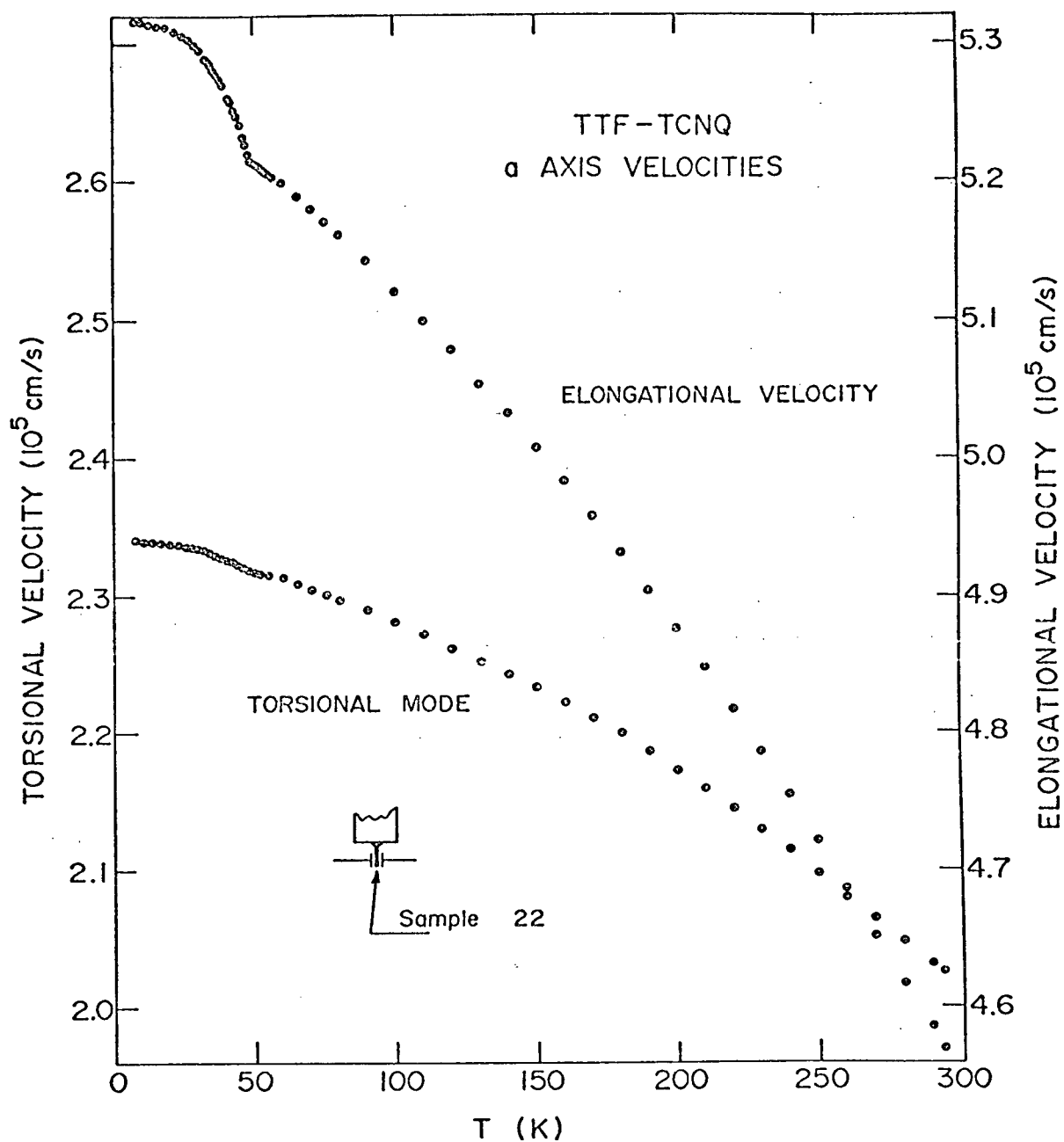


Fig. 48 - Temperature dependence of a axis Young's modulus velocity and shear velocity obtained from F_{ac} and T_a modes respectively

The bonding in the a direction in TTF-TCNQ is expected to be at least partly ionic and the corresponding Young's modulus is comparable with the ionic solid NaCl. Similarly in the b direction where we expect some metallic component to the bonding, the TTF-TCNQ Young's modulus is comparable to lead, a soft metal. Certainly within the category of metallic solids and to a lesser extent the ionic solids there is a wide range of elastic constants. Nevertheless, it is clear that the elastic constants of TTF-TCNQ are comparable to those for other common materials.

An anomalously soft a axis modulus might be expected if the conducting molecular stacks were weakly coupled. However, both the a and b axis moduli are significantly bigger than the modulus for a weakly bound solid such as Argon at 82K (see Table VII). Some idea of the elastic anisotropy is obtained by taking the ratio of the Young's modulus along a to the Young's modulus along b. This ratio is about 2.2 for TTF-TCNQ, whereas for zinc (hexagonal) the ratio of the Young's moduli parallel and perpendicular to the hexagonal symmetry axis, is 3.37. By this measure zinc is more anisotropic elastically than TTF-TCNQ. A comparison with the elastic constants of other crystalline materials confirms that the elastic anisotropy of TTF-TCNQ is more or less typical of non-cubic crystalline materials.

Now let us consider the temperature dependence of the velocity of sound in TTF-TCNQ. The temperature dependence of the b axis Young's modulus velocity $(E_b/\rho)^{\frac{1}{2}}$ is shown in Figs. 46 and 47. The data in Figs. 46 and 47 were obtained from an elongational mode and an F_{bc} flexural mode

respectively. Fig.48 shows the temperature dependence of the a axis Young's modulus velocity $(E_a/\rho)^{\frac{1}{2}}$ as determined from an F_{ac} flexural mode. As discussed in Chapter II, Section 2.1 two different torsional modes can be used to measure the shear velocity $(c_{66}/\rho)^{\frac{1}{2}}$, to a good approximation. The temperature dependence of this shear velocity is shown in Figs.46 and 48. The shear velocity data in Fig.46 was obtained from a T_b torsional mode and the data in Fig.48 from a T_a mode. All of the above sound velocity measurements have been corrected for thermal expansion using the correction of Jericho et al (1977) given in the Appendix § 3. This correction was inferred from the X-ray data of Blessing and Coppens (1974) and the b axis thermal expansion measurements of Schafer et al (1975). The temperature dependence of the elastic constants follows directly from the temperature dependence of the sound velocity and the density.

The main features in the velocity results are the kink in the Young's modulus velocities near 52K, and the strong temperature dependence in the higher temperature region. Before discussing the anomaly near 52K, we first consider the large overall temperature dependence of the velocities. The velocity results imply that the elastic moduli decrease by $\sim 40\%$ between 0K and room temperature. Although this may seem like a large temperature dependence when compared with conventional metals where the elastic constants typically change by only a few percent over this range, a large temperature dependence would be expected from the relatively low solidification temperature for TTF-TCNQ of 498K (Weiler 1977). In fact, if one compares the temperature dependence

of the elastic moduli for a variety of solids from 0K up to just below their melting point a large reduction in modulus (~ 50%) is normally observed.

We now consider the bulk modulus since the temperature dependence of this modulus is the easiest to calculate. If we make the hexagonal approximation to the crystallographic symmetry of TTF-TCNQ, described in Chapter II, Section 2.1, then the experimental Young's moduli may be used to obtain a rough estimate of the bulk modulus. In the hexagonal approximation the bulk modulus is given by

$$B = \left(\frac{2(1-\nu)}{E_a} + \frac{1-4\nu'}{E_b} \right)^{-1}$$

where E_a and E_b are the a and b axis Young's moduli and ν and ν' are Poisson's ratios. If the Poisson's ratios are restricted to lie between 0 and $\frac{1}{2}$ (Landau and Lifshitz 1970) the bulk modulus must be between $\left(\frac{2}{E_a} + \frac{1}{E_b} \right)^{-1}$ and infinity. Obviously this is not a very precise estimate. Although ν and ν' have not been measured experimentally, nevertheless, if we arbitrarily set $\nu = \nu' = 0.2$ then the room temperature values for the elastic constants given in Table V of Chapter II combined with the temperature dependence presented earlier in this chapter suggest that $B \sim 2 \times 10^{11}$ dynes/cm² at 0K. This estimate for the zero temperature bulk modulus compares with a room temperature bulk modulus of 0.94×10^{11} dynes/cm² measured by Debray et al (1977). Even though it is not possible to arrive at a very accurate estimate for B from the experimental data on E_a and E_b , since all of the measured elastic moduli have similar overall temperature dependences it is reasonable to assume the bulk modulus follows

the other moduli as a function of temperature.

In general it is extremely difficult to calculate the bulk modulus of a solid, as it means deriving an expression for the pressure of a solid as a function of its volume, in other words an equation of state. In the conventional adiabatic approximation the equation of motion of the lattice, and hence the sound velocity, is determined by the dependence of the electronic energy eigenvalues on the position of the nuclei and by the direct electrostatic interaction between the nuclei. The direct interaction between different nuclei is probably small compared to the interaction between nuclei and core electrons and between core electrons on different nuclei. Accordingly if one knew how the electronic energy eigenvalues depended on the positions of the ions one could calculate all of the elastic constants. In one special case, namely the alkali metals, this can be done with a reasonable degree of accuracy. In this case the outer electrons can be closely approximated by free electrons and the nuclei and core electrons can be ignored because they are thoroughly screened between different sites. The free electron nature of the electron energy states does not change when the lattice is strained. The only effect of the strain is to cause a change in the Fermi level necessary to maintain local charge neutrality. Thus, the dependence of the electronic energy states on the position of the ions is known and the elastic moduli can be calculated (Kittel 1971). However, for almost any material other than the alkali metals more than one electron energy band needs to be considered and the bands change in complicated ways with strain. Although the contribution of

particular bands to the elastic moduli can still be calculated, it is no longer reasonable to try to calculate the moduli from first principles. Instead the normal procedure is to start with a parameterized intermolecular potential. We will follow this procedure here.

In general the isothermal bulk modulus for any system is given by (Landau and Lifshitz 1969)

$$B_T = V \left(\frac{\partial^2 F}{\partial V^2} \right)_T$$

where F is the free energy of the system, and V is its volume. Similarly the adiabatic bulk modulus is given by

$$B_S = V \left(\frac{\partial^2 U}{\partial V^2} \right)_S$$

where U is the internal energy, and the volume derivatives are taken at constant entropy S . In order to calculate the temperature dependence of B_T and B_S we need F and U as functions of temperature and volume.

The standard expressions are (Girifalco 1973)

$$[1a] \quad F = F_0 + \frac{V_0 B_0}{2} \left(\frac{V-V_0}{V_0} \right)^2 - \frac{V_0 A}{6} \left(\frac{V-V_0}{V_0} \right)^3 + kT \sum_q \ln \left(2 \sinh \frac{\hbar \omega_q}{2kT} \right)$$

$$[1b] \quad U = U_0 + \frac{V_0 B_0}{2} \left(\frac{V-V_0}{V_0} \right)^2 - \frac{V_0 A}{6} \left(\frac{V-V_0}{V_0} \right)^3 + \sum_q \frac{\hbar \omega_q}{2} \coth \left(\frac{\hbar \omega_q}{2kT} \right)$$

where the intermolecular potential has been expanded to third order in

the volume strain. The third order term is necessary because of thermal expansion, as will be clear later. The thermal phonon frequencies ω_q will depend on volume in some complicated way. We approximate their volume dependence by

$$\omega_q(V) = \omega_q(V_0) (V_0/V)^\gamma$$

where γ is a volume independent Grüneisen constant. In this approximation the volume expansion coefficient $\alpha(T)$ is given by (Callen 1960)

$$[2] \quad \alpha(T) = \frac{\gamma C_p(T)}{V(T) B_s(T)} = \frac{\gamma C_v(T)}{V(T) B_T(T)}$$

where C_p and C_v are the specific heats at constant pressure and volume respectively. By integrating [2] we find

$$[3] \quad V(T) \approx V_0 + \frac{\gamma U}{B_T(T)} \approx V_0 + \frac{\gamma U}{B_s(T)}$$

where U is the internal energy of the lattice.

$$U = \sum_q \frac{\hbar \omega_q}{2} \coth \left(\frac{\hbar \omega_q}{2kT} \right).$$

In eqn. [3] we have assumed that $C_p \approx C_v$ and that the temperature dependence of the volume and bulk modulus is small compared to the temperature dependence of the specific heat. These approximations improve at low temperatures.

Using the definition of the isothermal bulk modulus and the expression for the free energy [1a], one can now write down the isothermal bulk modulus as a function of temperature in terms of the parameters γ and A . Both of these parameters are manifestations of the anharmonic part of the intermolecular force constants. It is useful to express A in terms of the pressure derivative of the bulk modulus since this quantity can be measured directly. The pressure derivative of B_T is obtained from

$$[4] \quad -V_0^2 \frac{\partial^3 F}{\partial V^3} = A - \frac{\gamma}{V_0} \left[(\gamma+1)^2 U - 2\gamma(\gamma+1) \frac{dU}{dT} + \gamma^2 \frac{d^2 U}{dT^2} \right]$$

by dividing by B_T . The second term in [4] is expected to be at most comparable with the total temperature dependent part of B_T whereas A will be shown to be $\geq 10B$ for TTF-TCNQ. To a good approximation the second term in [4] can be neglected and $\partial B_T / \partial P = A / B_T$. In terms of $\partial B_T / \partial P$ the isothermal bulk modulus is

$$[5a] \quad B_T(T) = B_0 + \frac{\gamma}{V_0} \left[(\gamma+1) - \frac{\partial B_T}{\partial P} \right] U - \frac{\gamma^2 T}{V_0} C_V.$$

The first term in the square brackets in [5a] tends to make the lattice stiffer at high temperatures. This term arises from the phonon pressure. The negative $\partial B_T / \partial P$ term comes from the thermal expansion combined with the softening of the intermolecular potential with increasing volume.

Similarly, the adiabatic bulk modulus is found by taking partial derivatives of the internal energy with respect to volume, maintaining

the entropy constant. In the Grüneisen approximation, the entropy may be kept fixed by allowing the temperature to be a function of volume in such a way that ω_q/T is independent of volume. Since the entropy is a function of ω_q/T only, it will be constant if ω_q/T is constant. A procedure similar to that used in obtaining the isothermal modulus then leads to

$$[5b] \quad B_s(T) = B_0 + \frac{\gamma}{V_0} \left[\gamma + 1 - \frac{\partial B_s}{\partial P} \right] U.$$

Normally ultrasonic techniques measure adiabatic moduli. Whether it is the adiabatic or isothermal modulus which is appropriate depends on the relation between the period of the sound wave and the time for thermal relaxation between a rarefaction and compression in the wave. In the TTF-TCNQ experiment the adiabatic moduli determine the resonance frequency of all of the modes studied with the possible exception of the fundamental flexural mode and its first few harmonics, depending on the geometry of the sample. In a flexural mode the compressed and expanded parts of the sample are separated by a distance equal to the sample thickness only, even though the mode frequency may be relatively low. In this case the isothermal modulus applies when the resonant frequency is small compared to the thermal relaxation frequency f_0 discussed in Section 2.3 (ii) and the adiabatic modulus applies at higher frequencies.

Eqn.[2] combined with our estimate of $B_S(0)$ and the published thermal expansion and specific heat data, enable us to estimate γ . From the X-ray structure data (Blessing and Coppens 1974) we estimate $\alpha(T) = 1.6 \alpha_b(T)$ where $\alpha_b(T)$ is the b axis linear expansion coefficient measured by Schafer et al (1975). Using this estimate for $\alpha(T)$ we obtain $\gamma = 2.56$, which is not an unreasonable value. The Grüneisen constants for a variety of different materials are given in Table VIII.

TABLE VIII

Grüneisen Constants for Various Materials [†]

Material	Grüneisen γ	T(K)
Si	0.44	300
Au	3.0	0
NaCl	1.55	300
TTF-TCNQ	2.6	0
Na	1.14	90
Ar	2.7	82

[†] Daniels (1963), Gewurtz et al (1972)

Now that we have an estimate for γ [2] can be used to predict the heat capacity beyond the 12K range near 55K measured by Craven et al (1974). The heat capacity which results is typical of molecular solids (Lord 1941). Near room temperature the predicted heat capacity is 35R and increasing approximately linearly at 0.05 R/K. R is the gas constant per mole of TTF-TCNQ formula units. The large value of the heat

capacity clearly indicates the importance of intramolecular and librational degrees of freedom. These low frequency Einstein modes of the TTF and TCNQ molecules dominate C_p above 20K.

It is also possible to make a direct comparison between the temperature dependence of the bulk modulus and the thermal expansion coefficient. Differentiating [5b] with respect to volume and neglecting the temperature dependence of $\partial B_S/\partial P$ we get

$$[6] \quad \frac{1}{B_S} \frac{dB_S}{dT} \approx \left[\gamma + 1 - \frac{\partial B_S}{\partial P} \right] \alpha(T).$$

It may not be a very good approximation to neglect the temperature dependence of $\partial B_S/\partial P$ (Daniels 1963), however, there is neither experimental data nor a reasonable model available to describe its temperature dependence. If we make the previously stated assumption that the temperature dependence of the bulk modulus follows the temperature dependence of the measured elastic moduli, then in conjunction with the experimental velocity data, [6] may be used to estimate $\partial B_S/\partial P$. Using the b axis velocity data, together with $\alpha = 1.6 \alpha_b$ and $\gamma = 2.56$ we find $\partial B_S/\partial P \sim 15-17$. In light of the approximations we have made, this number compares well with $\partial B_T/\partial P \sim 12$ inferred from the pressure measurements of Debray et al (1977). The pressure derivative of the bulk modulus is given in Table IX for a number of materials.

Between 52 K and about 200K for the b axis extensional modes and over a wider temperature range for the other modes, the shape of the velocity

TABLE IX
Pressure Dependence of Bulk Modulus [†]

Material	$\frac{\partial B_T}{\partial P}$
Si	5.3
Au	6.1
NaCl	5.7
TTF-TCNQ	15-17
Na	3.3
Ar	8.5

[†] Daniels (1963), Paul and Warschauer (1963)

curves is consistent with [6]. (Recall that in our approximation $v^{-1} \partial v / \partial T = (2B)^{-1} \partial B / \partial T$, where v is a sound velocity.) We therefore suggest that if TTF-TCNQ remained metallic down to 0K, the temperature dependence of the velocities would be of the general form shown by the dashed line in Fig. 48. For this reason we interpret the anomaly near 52K in the extensional mode velocities as a stiffening in the modulus above a background which represents the contribution to the elastic constants from anharmonic effects. The other possible interpretation is to regard the anomaly as a broad softening between 40K and 120K. This interpretation is rejected because the resulting temperature dependence does not match the thermal expansion data quite as well, and secondly there is no other experimental evidence for such a broad transition temperature region (>80K).

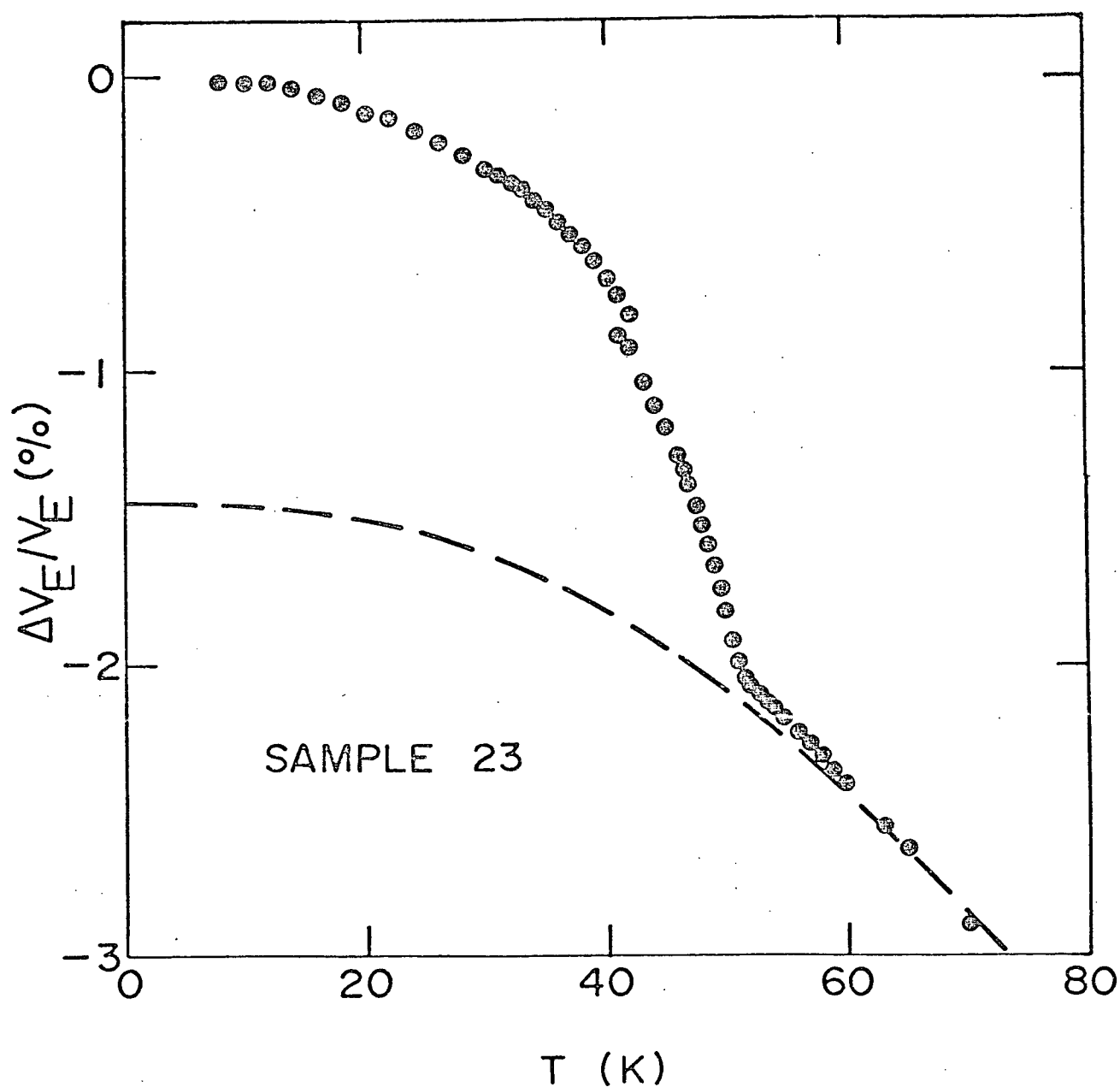


Fig. 49 - Enlargement of low temperature anomaly in the Young's modulus velocity. The dashed line is obtained from eqn.[6] in the text. The break in the curve near 42K results from a splitting of the first longitudinal mode caused by interference from another mode, probably a harmonic of the fundamental flexural or torsional modes.

Summarizing, we conclude from the large value for the heat capacity and from the interdependence of the heat capacity, thermal expansion and bulk modulus that the temperature dependence of all three quantities is dominated by librations and intramolecular modes above $\sim 20\text{K}$.

3.2 Low Temperature Anomaly

We now discuss the low temperature anomaly in the sound velocity, taking the point of view that it is a stiffening in the elastic modulus above the background temperature dependence. The velocity anomaly is shown in Fig. 49. The low temperature velocity data can be summarized as follows. Below the metal-insulator transition there is an anomalous increase in velocity for modes which involve a volume change. This increase reaches a maximum of about 1.5% above the extrapolated background at 0K. The fractional increase is about the same for the Young's modulus modes in the a and b directions and much smaller or even absent in the shear modes. In the remainder of this chapter we show how these experimental results may be interpreted in terms of the contribution of the conduction electrons to the sound velocity. This section is divided into two parts. In the first part we show that an electron-phonon interaction in the high frequency quantum limit leads to a softening of the sound velocity in the metallic phase. In the second part we consider the tight-binding band structure of TTF-TCNQ in detail and show that the electron-phonon coupling can also lead to a softening in the metallic phase at zero frequency.

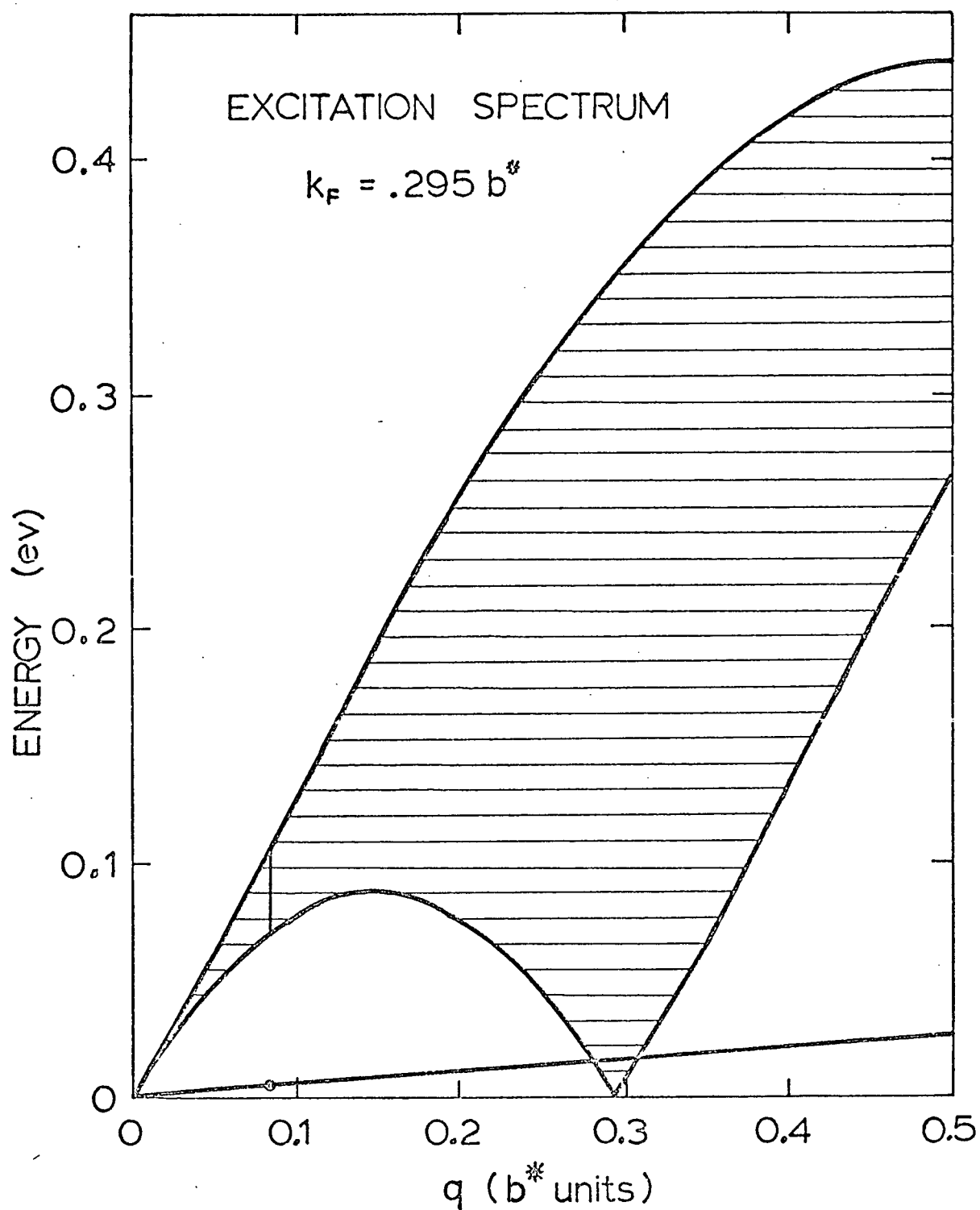


Fig. 50 - Excitation spectrum for a non-interacting tight-binding electron band (TCNQ band) and an uncoupled acoustic phonon branch.

(i) Quantum Limit

In the quantum limit (see Part A, Chapter 1, Section 1.3) the effect of the conduction electrons on the sound velocity may be calculated by treating the electron-phonon interaction as a perturbation on the uncoupled electron and phonon system. The unperturbed energy levels for the electrons are described by a single particle tight-binding band. Consistent with the tight-binding approximation (Barisic 1972), the unperturbed phonons exist in a lattice of neutral 'ions'. Thus there is a phonon mode (acoustic phonon) which propagates down to zero frequency with a linear dispersion in the unperturbed system. This behaviour contrasts with nearly free electron models where the unperturbed lattice consists of charged ions, and the corresponding unperturbed phonon frequency is an ionic plasma frequency.

The excitation spectrum for the non-interacting one dimensional electron-phonon system at zero temperature is shown in Fig.50. Only one low frequency phonon branch is shown for clarity, although in general for any direction of propagation there are two other branches. The sound velocity determines the slope of the phonon branch and the Fermi velocity determines the slope of the electron branch near $q = 0$. These slopes are drawn approximately to scale in Fig.50. The electron Fermi velocity shown is for the TCNQ band calculated by Berlinsky et al (1974). The shaded area is the locus of $\epsilon(k+q) - \epsilon(k)$ with k as a parameter and the additional requirement that the initial state k be full and the final state $k+q$ be empty. $\epsilon(k)$ is the energy of an electron

in the state k . The electron-phonon interaction H_{int} (see Part A, Chapter 1, Section 1.3) will couple a phonon with wavevector q to all the electronic excitations with the same wavevector. In terms of Fig. 50, the electronic excitations lying along a vertical line directly above the phonon of interest are coupled to the phonon.

To second order in perturbation theory this coupling reduces the phonon frequency to

$$[7] \quad \hbar\omega_q = \hbar\omega_q^0 - \frac{1}{n(q)} \sum_k \frac{|\langle k | H_{int} | k+q \rangle|^2}{\epsilon(k+q) - \epsilon(k) - \hbar\omega_q}.$$

The unperturbed phonon frequency is ω_q^0 and the occupancy $n(q)$ of the phonon mode q is assumed to satisfy $n(q) \gg 1$. We substitute the squared matrix elements of

$$H_{int} = g \sum_{k,q} \left(\frac{\hbar\omega_q}{2} \right)^{\frac{1}{2}} \begin{pmatrix} a_q^+ & -a_{-q} \end{pmatrix} \begin{matrix} c_{k-q\sigma}^+ \\ c_{k\sigma} \end{matrix}$$

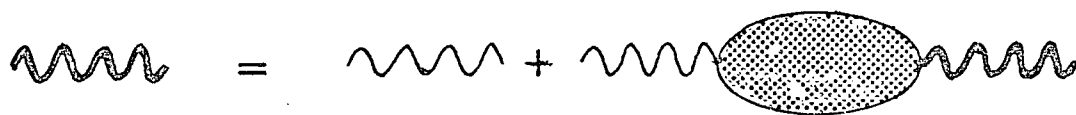
given in Part A, Section 1.3 where the electron-phonon coupling constant $g = C/\sqrt{B_S}$. B_S is the adiabatic bulk modulus and C is a deformation potential. With these substitutions [7] reduces to

$$[8] \quad \hbar\omega_q = \hbar\omega_q^0 - g^2 \frac{\hbar\omega_q^0}{2} \sum_k \frac{f(k) - f(k+q)}{\epsilon(k+q) - \epsilon(k)}$$

assuming that the sound velocity is much smaller than the electron Fermi velocity. Although second order perturbation theory is probably the simplest way of approximating the effect of the electron-phonon

interaction on the phonon frequencies, a more general technique is also available.

In the Green's function formalism, the phonon frequency ω_q is a pole of the perturbed phonon Green's function $D(q)$. An expression for $D(q)$ can be obtained with the help of Dyson's equation shown schematically in Fig.51.



$$D(q) = D^0(q) + D^0(q) \frac{g^2}{\hbar} \Pi(q) D(q)$$

Fig. 51 - Dyson's Equation

This equation may be rearranged to give

$$[9] \quad D(q)^{-1} = D^0(q)^{-1} - \frac{g^2}{\hbar} \Pi(q).$$

The last term includes the phonon self-energy $\Pi(q)$. We now substitute (Abrikosov et al 1963)

$$D^0(q) = \frac{-\hbar\omega_q^2}{\omega^2 + \omega_q^2}$$

for the finite temperature phonon Green's function and an identical expression for $D(q)$ except the superscript zero is removed. If we set $i\omega = \omega_q$ in [9] then

$$[10] \quad \omega_q^2 = \omega_q^{02} \left[1 + g^2 \Pi(q) \right] .$$

This expression for the perturbed phonon frequencies is valid to arbitrary order in perturbation theory. The first term in the diagrammatic expansion for $\Pi(q)$ is

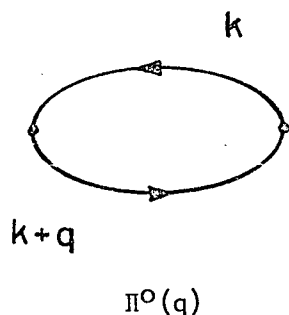


Fig. 52 - Electron Gas Polarization Diagram

This lowest order polarization insertion or "bubble diagram" is very well known. In the low frequency limit it can be shown that (Fetter and Walecka 1971, Doniach and Sondheimer 1974)

$$\Pi^0(q) = - \sum_k \frac{f(k) - f(k+q)}{\epsilon(k+q) - \epsilon(k)} .$$

The summation on the right is the Hartree polarizability $\chi^0(q)$ of the electron gas. If this expression is substituted into [10] we

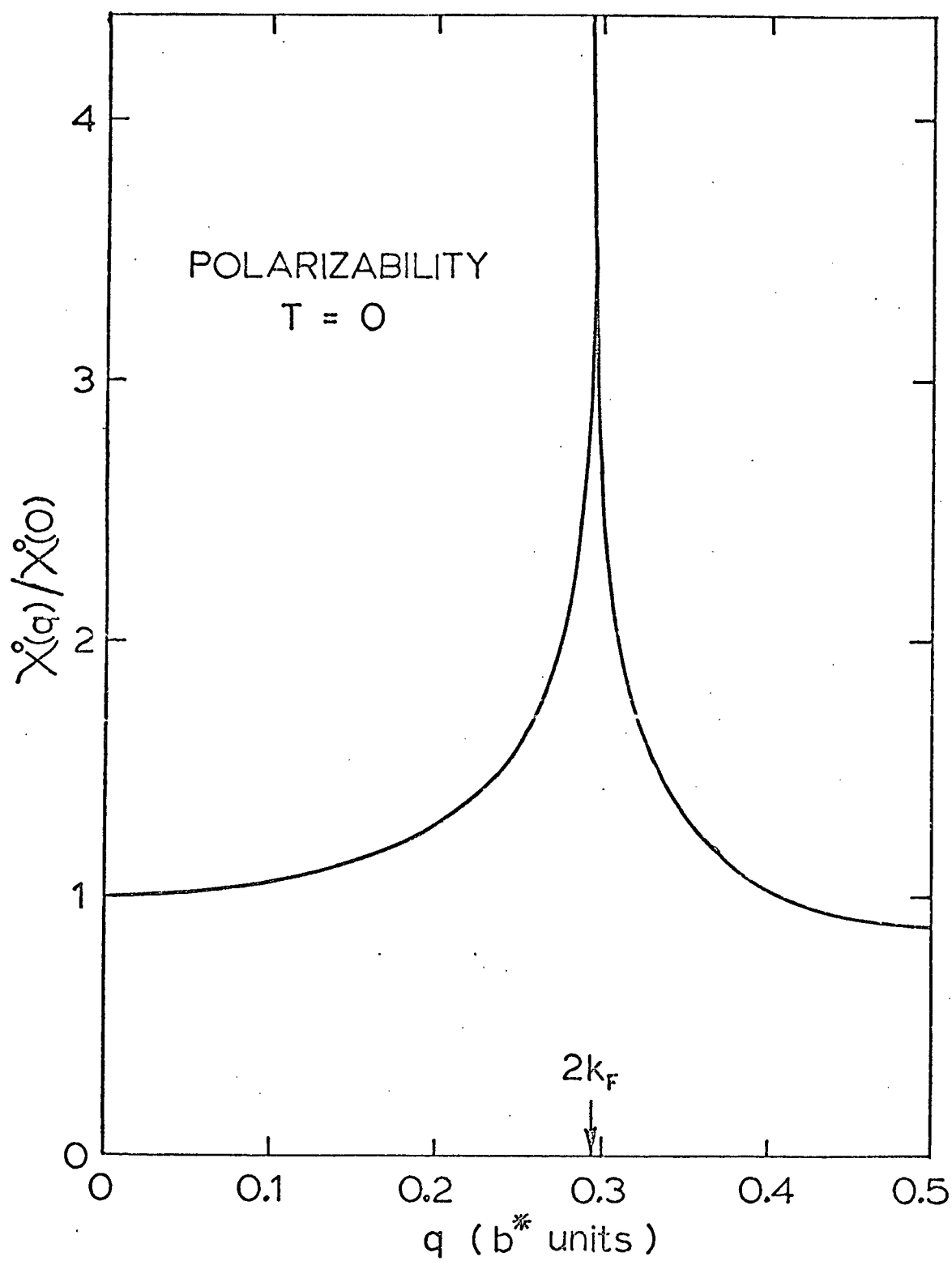


Fig. 53 - Hartree polarizability for the one dimensional TCNQ band discussed in the text

regain the second order perturbation theory result [8] for the perturbed phonon frequencies.

It is not difficult to evaluate the polarizability $\chi^0(q)$ for a one dimensional tight binding band of electrons. The static polarizability for a metallic band at temperatures low compared with the Fermi temperature is

$$[11] \quad \chi^0(q) = N(\epsilon_f) \frac{\sin k_f b}{2 \sin \frac{q}{2}} \ln \left| \frac{\tan \frac{1}{2} \left(k_f + \frac{q}{2} \right)}{\tan \frac{1}{2} \left(k_f - \frac{q}{2} \right)} \right|$$

where $N(\epsilon)$ is the electronic density of states, ϵ_f is the Fermi energy and k_f the Fermi wavevector. A graph of $\chi^0(q)$ as a function of q is shown in Fig.53 using the same tight binding band parameters used in the excitation spectrum shown in Fig.50. The logarithmic singularity in $\chi^0(q)$ at $q = 2k_f$ is responsible for the large Kohn anomaly in the phonon spectrum and the resulting charge density wave or Peierls transition in one dimensional conductors. The divergence in $\chi^0(q)$ is present at zero temperature in any material with parallel sections of Fermi surface. Note that $\chi^0(q)$ for a tight-binding band does not approach zero for large q unlike the nearly free electron case (André et al 1976).

Although the singularity in $\chi^0(q)$ is important in determining the phonon spectrum near $2k_f$, we are more interested in the long wavelength phonons with $q \rightarrow 0$. In the long wavelength limit, the change in the sound velocity implied by [8] is

$$[12] \quad \frac{\Delta v}{v} = - \frac{C^2}{2B_S} \int N(\epsilon) \left(- \frac{\partial f}{\partial \epsilon} \right) d\epsilon .$$

The integral in [12] approaches $N(\epsilon_f)$ in the metallic phase at low temperatures and goes exponentially to zero in the semiconducting phase at low temperatures. From [12] one would expect a fractional increase in the velocity of sound of $N(\epsilon_f) C^2/(2B_S)$ in cooling TTF-TCNQ through its metal-insulator transition. This is qualitatively the effect which is experimentally observed in the extensional modes. To see how the size of this effect compares with experiment we substitute an average density of states for the TTF-TCNQ bands (Berlinsky et al 1974) of 5.8 ev^{-1} and use $B_S = 2 \times 10^{11} \text{ dynes/cm}^2$ as discussed earlier. For a fit to the observed 1.5% velocity anomaly $C = 0.38 \text{ ev}$. This number is certainly reasonable since the average bandwidth from the molecular orbital calculations (Berlinsky et al 1974) is 0.32 ev , and tight-binding bands are expected to have deformation potentials of the order of the bandwidth (Mitra 1969).

The much smaller anomalies observed in the shear velocities are also explained by this model because the deformation potential for shear waves is expected to be small for metals in which all of the Fermi surface is in one Brillouin zone (Kittel 1963). There is no reason to expect any of the TTF-TCNQ Fermi surface to lie outside the first zone.

It is interesting to extrapolate the experimentally observed softening in the sound velocity up to $q \sim 2k_f$ with the help of the

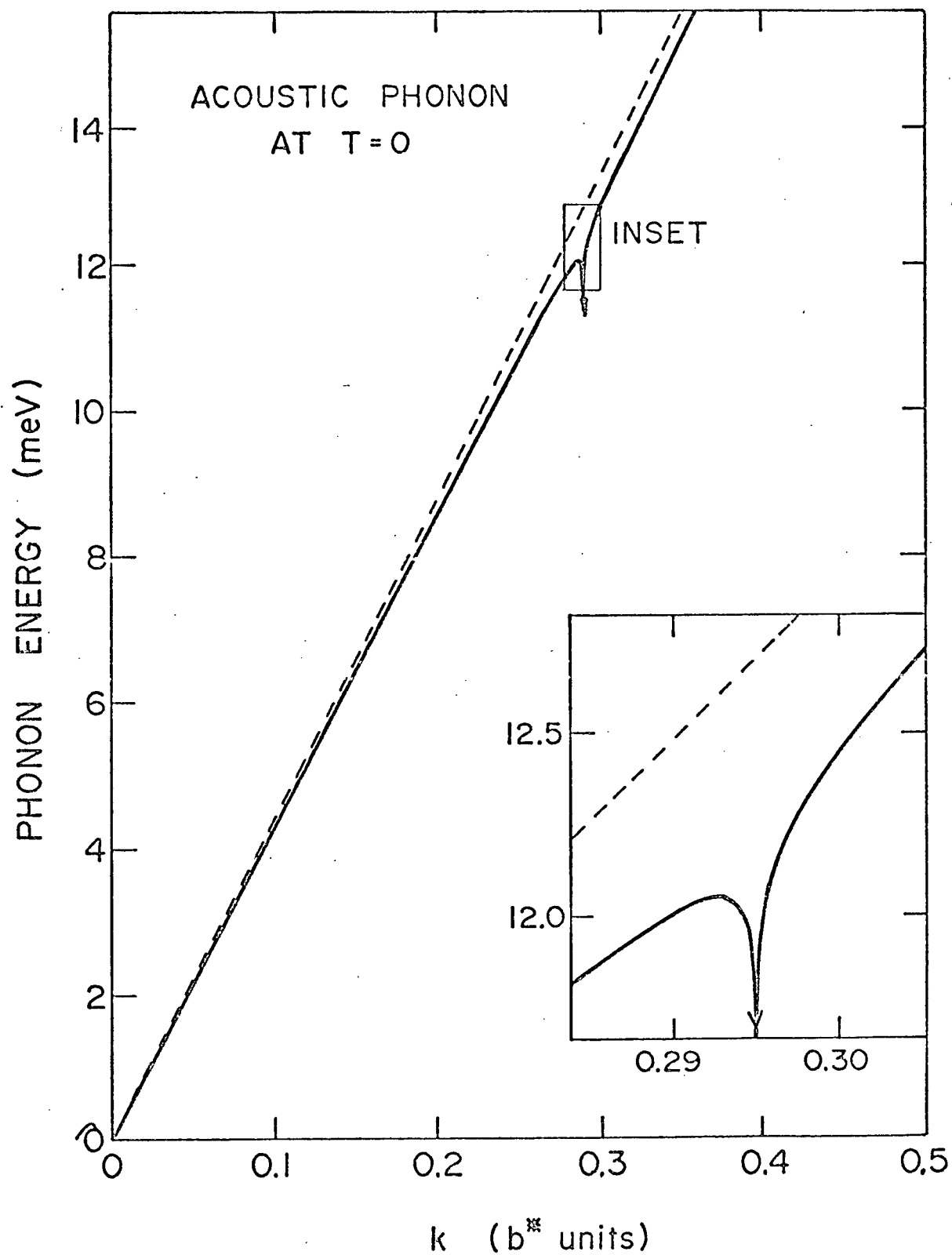


Fig. 54 - Zero temperature longitudinal acoustic phonon dispersion calculated from [8] using the experimental electron-phonon coupling constant

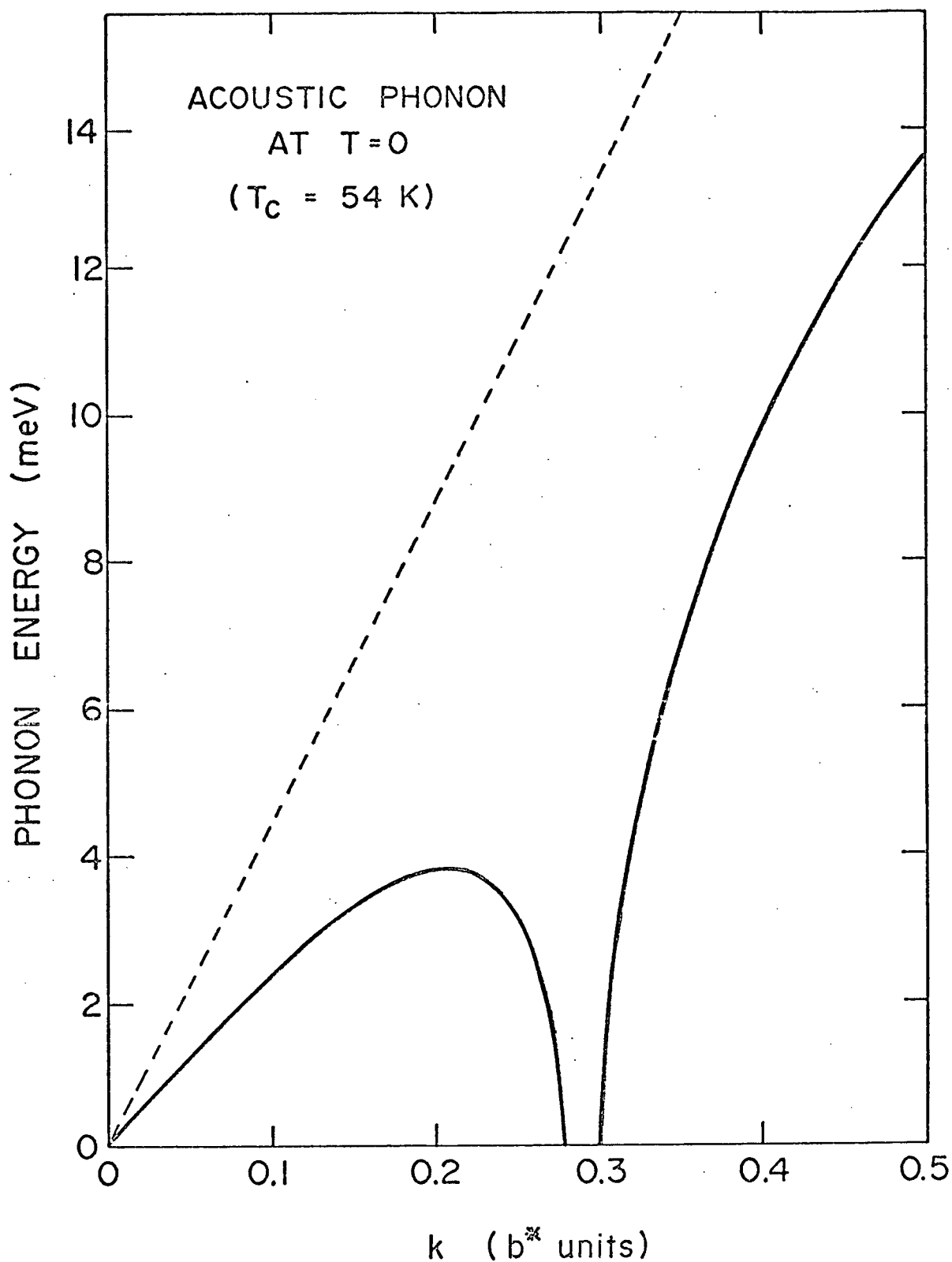


Fig. 55 - Zero temperature longitudinal acoustic phonon dispersion calculated from [8] for an electron-phonon coupling constant which yields a T_c of 54K

q dependent polarizability expression [11]. If one assumes a q independent coupling constant g , then the perturbed longitudinal acoustic phonon spectrum is given by the solid line in Fig.54, for (hypothetical) metallic TTF-TCNQ at zero temperature. The dashed line is the unperturbed phonon frequency. The small Kohn anomaly in Fig.54 is much too small to account, in the mean field theory (Rice and Strassler 1973) for the observed metal-insulator transition temperature. This discrepancy may not be unreasonable since the mean field model is not expected to be very accurate. Nevertheless, it is interesting to pursue some of the implications of the small Kohn anomaly in Fig.54, in the framework of the mean field theory.

The electron-phonon coupling constant g would have to be about a factor of five bigger, in order that the Kohn anomaly in the acoustic phonon be large enough to account for the observed metal-insulator transition temperature. If the larger value of g is substituted into [11] then the large zero temperature softening of the acoustic phonon mode shown in Fig.55 results. Such a drastic softening is not observed in the inelastic neutron scattering measurements of Shapiro et al (1977). In fact the Kohn anomaly observed by neutron scattering resembles the much smaller anomaly in Fig.54. These observations suggest that the metal-insulator transition in TTF-TCNQ is caused by a static distortion in a combination of intramolecular modes as proposed by Rice and Lipari (1977). If a metal-insulator transition can be produced by coupling of the conduction electrons to intramolecular modes in addition to the intermolecular acoustic modes, then it will be

more difficult to stabilize the low temperature metallic state of an organic solid, especially if the material is composed of extended molecules.

Even though the model described above seems to be in excellent agreement with the low frequency sound velocity measurements below the metal-insulator transition, the calculations were made in the quantum limit for well defined phonon and electron states. That is, the lifetime broadening of the electron and phonon states has been implicitly assumed to be negligible. In reality for the frequencies used in the experiments $q\ell \ll 1$ (recall ℓ is the electron mean free path), and therefore the lifetime broadening of the electronic excitations is enormous compared to $\hbar\omega$. This broadening has a drastic effect on the ultrasonic attenuation where transition rates for energy conserving transitions must be calculated. However, in the present case we are only interested in virtual transitions to a continuum of electron states. The fact that the electron states are much broader than the energy change involved in an electron-phonon scattering process is not important since energy does not need to be conserved in virtual transitions anyway. On the average we expect the virtual transitions to coincide with the well defined quantum transition, and the quantum result should still be valid at low frequencies.

Another equally non-rigorous argument can be made for the validity of the quantum result at low frequencies. In nearly free electron models the unperturbed phonon frequency is the lattice plasma frequency $\Omega_p = (4\pi n e^2 / M)^{1/2}$ where M is the ion mass. The effect of adding

electrons, which will interact with the ions in such a way so as to screen the ions, is to reduce the plasma frequency to $\Omega_p/\sqrt{\epsilon_q}$. The new phonon branch now has a linear dispersion down to zero frequency (Pines and Nozieres 1966). The dielectric constant ϵ_q can be calculated from the polarizability using the same quantum limit approach and the same approximation that we have used in calculating the change in phonon frequency. The dielectric constant approach leads to the correct low frequency sound velocity. By analogy, our calculation of the phonon frequencies should also lead to the correct low frequency velocity.

(ii) Thermodynamic Limit

These difficulties with the applicability of the quantum formalism in the low frequency limit all vanish if instead we approach the problem from the point of view of calculating a static elastic constant. The elastic constants for a material in thermodynamic equilibrium are determined by taking second order strain derivatives of an appropriate thermodynamic potential, as discussed in Section 3.1 above. For electrons the thermodynamic limit is valid provided that $q\ell \ll 1$ (see Part A, Chapter I) which is always well satisfied in the experiment described here. As pointed out in the previous section it is primarily the highest occupied electron energy bands which determine the elastic constants. In order to calculate the total contribution of the electrons to the elastic constants we need to know the dependence of the electron energy bands on strain, to second order in the strain. However, if we

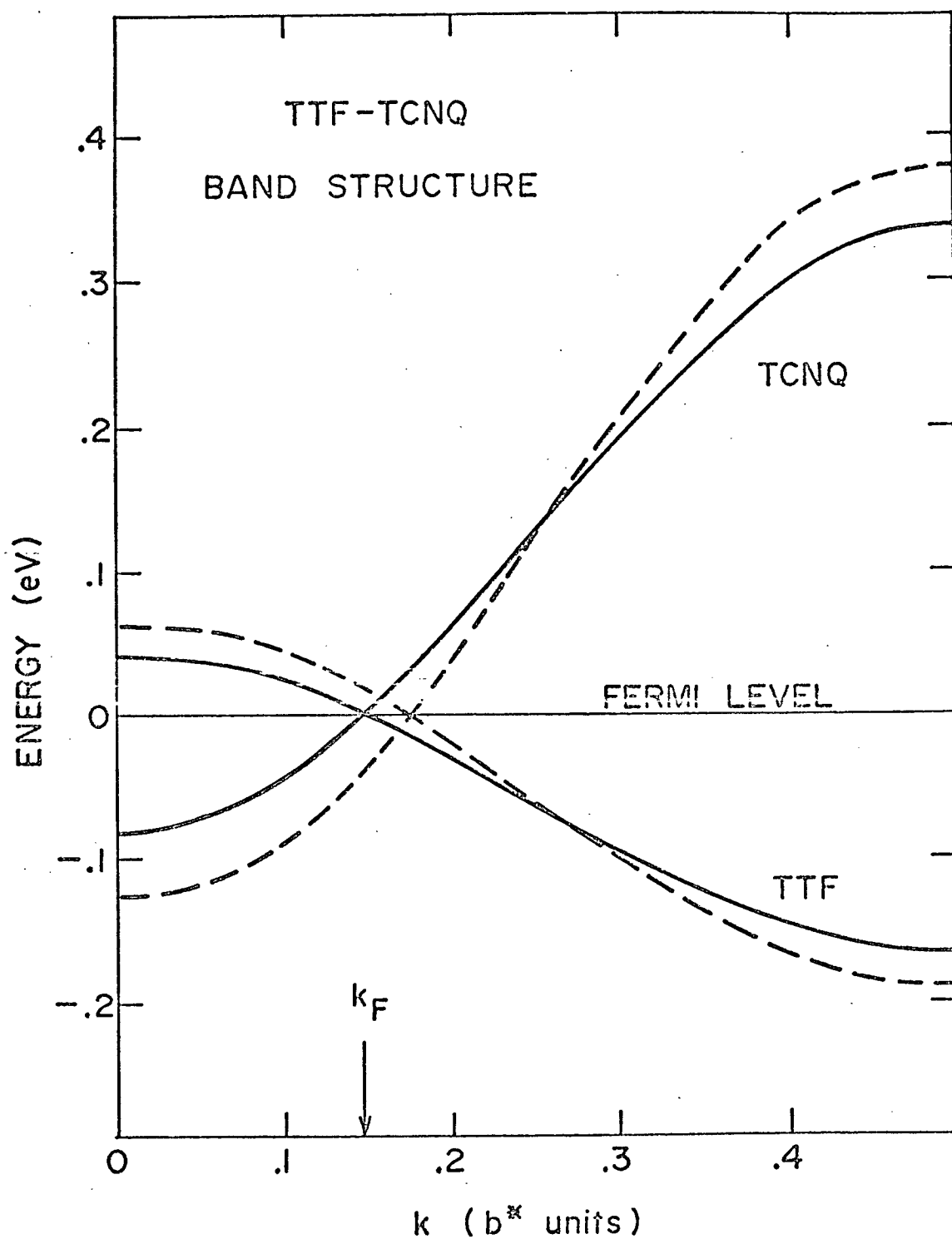


Fig. 56 - Band structure of TTF-TCNQ discussed in the text. The dashed line shows the effect of an exaggerated b axis compression

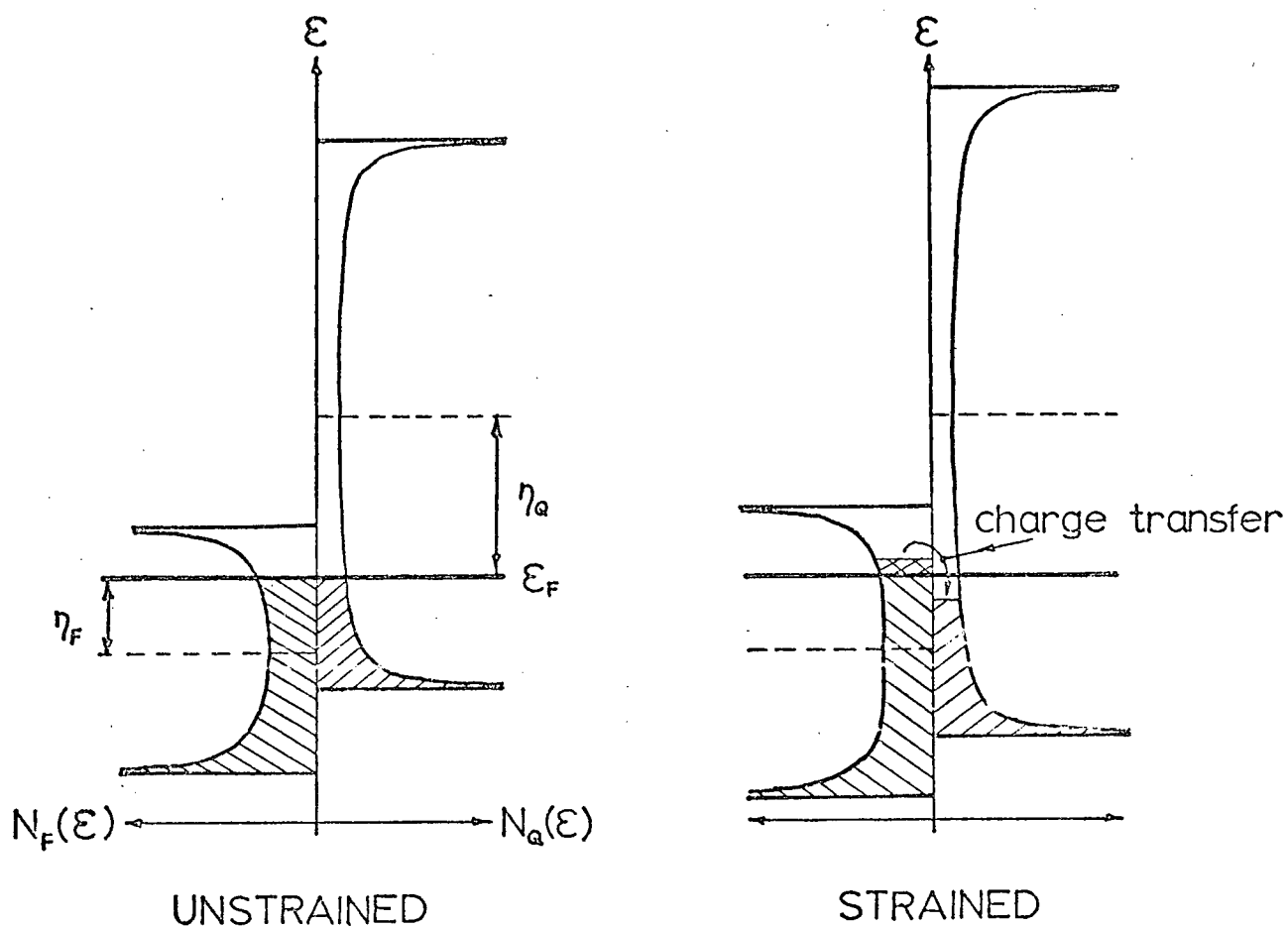


Fig. 57 - Effect of a b axis compression on the density of occupied states for the band structure shown in Fig. 56

can be satisfied with calculating the small change in elastic constants brought about by a metal-insulator transition, then the problem is easier. In this case it is not necessary to know the strain dependence of all of the band parameters to second order, provided the features which lead to a change in the elastic constant at the metal-insulator transition are correctly described.

We consider the following simple model for the strain dependence of the band structure. The energy bands for the TTF and TCNQ chains are taken to be one dimensional tight-binding bands with band parameters as calculated by Berlinsky et al (1974). In this band structure the TTF(TCNQ) band has a maximum (minimum) at $k = 0$ (see Fig. 56). The Fermi level for the two bands is determined by assuming a charge transfer p of .59. In the spirit of the tight-binding approximation we assume identical strain dependences for the two bandwidths and strain independent centres of gravity. That is, a one dimensional strain in the conducting direction is assumed to scale the width of both the TTF and the TCNQ bands and their energy gaps in the insulating state, by the same factor $\exp(-\beta\zeta)$, where ζ is the b axis strain and β is a dimensionless parameter. In this model a strain will have no effect on the Fermi energy but will change the Fermi wavevector k_f and hence the charge transfer. The effect of a b axis compression on the density of occupied states is illustrated in Fig.57 for the tight-binding band structure shown in Fig.56. Note the additional charge transfer from the TTF to the TCNQ band.

We now investigate the effect of this small strain dependent charge transfer on the elastic modulus c_{22} . As discussed in the previous chapter the experiment measures the adiabatic moduli, and the temperature of the sample will be strain dependent. However, the lattice specific heat is very much larger than the electronic specific heat. For this reason the temperature of the sample will be determined by the requirement that the lattice entropy be a constant and not the electronic entropy. Since the electrons are thermally coupled to the lattice, their temperature will be determined by the phonon heat bath. Accordingly the contribution of the conduction electrons will be somewhere between adiabatic and isothermal. Since the difference between the two moduli is not expected to be very significant we will take the easiest approach and calculate the isothermal modulus.

The isothermal contribution to the modulus c_{22} is determined from the b axis strain dependence of the free energy density

$$[13] \quad F = \frac{1}{2} c_{22}^0 \zeta^2 - kT \int \ln\left(1 + \exp\left(-\frac{\epsilon}{kT}\right)\right) [N_F(\epsilon, \zeta) + N_Q(\epsilon, \zeta)] d\epsilon$$

where all contributions to the elastic modulus not connected with electron transfer have been incorporated into the first term. We have taken the Fermi energy to be zero for convenience. The TTF and TCNQ bands have strain dependent density of states functions given by $N_F(\epsilon, \zeta)$ and $N_Q(\epsilon, \zeta)$ respectively. The Brillouin zone boundary follows the strain selfconsistently.

The elastic constant c_{22} is obtained by differentiating the free energy [13] twice with respect to ζ . The result is

$$[14] \quad c_{22} = c_{22}^0 - \beta^2 \int \left[(\epsilon + \eta_F)^2 N_F(\epsilon) + (\epsilon + \eta_Q)^2 N_Q(\epsilon) \right] \left(-\frac{\partial f}{\partial \epsilon} \right) d\epsilon \\ + \beta^2 \int \left[N_F(\epsilon) + N_Q(\epsilon) \right] \epsilon f(\epsilon) d\epsilon$$

where η_F and η_Q are the energies of the centre of the TTF and TCNQ bands respectively. Since the relative position of the two bands is determined by the charge transfer ρ , the positions of the band centres are given by $\eta_{F(Q)} = 2t_{F(Q)} \cos\left(\frac{\rho\pi}{2}\right)$ as shown in Fig.57 where $4|t_F|$ and $4|t_Q|$ are the appropriate bandwidths. We now examine the behaviour of the last two terms in [14] when an energy gap opens up in the density of states and the material becomes an insulator.

The last term decreases by an amount proportional to $\beta^2 \left[\Delta_F^2 N_F(o) + \Delta_Q^2 N_Q(o) \right]$ where Δ_F and Δ_Q are the energy gaps on the two chains.

Similarly the second last term decreases in magnitude from $\beta^2 \left[\eta_F^2 N_F(o) + \eta_Q^2 N_Q(o) \right]$ to zero at zero temperature. Clearly this change is much bigger than the change in the last term in [14] since $(\Delta_F/\eta_F)^2$, $(\Delta_Q/\eta_Q)^2 \ll 1$. If the last term in [14] is neglected the elastic modulus will increase by

$$\frac{\Delta c_{22}}{c_{22}} = 2 \frac{\Delta v_{22}}{v_{22}} = \frac{\beta^2}{c_{22}^0} \left[\eta_F^2 N_F(o) + \eta_Q^2 N_Q(o) \right]$$

in cooling from the metallic phase, through the metal-insulator transition towards zero temperature.

We now approximate the longitudinal bulk wave velocity in the b direction, v_{22} by the b axis elongational velocity at $T = 0$, and use $t_F = .05$ eV and $t_Q = -.11$ eV for the overlap parameters (Berlinsky et al 1974). In this case $\beta = 4.1$ gives agreement with the observed low temperature velocity anomaly. This value for β may be compared with $\beta \sim 6$ inferred from the molecular orbital calculation of the overlap parameters. The agreement between the observed and calculated β is considered to be excellent.

The much smaller anomaly in the modes involving only shear moduli can now be explained as follows. Since there is no volume change associated with shear modes, there is no first order change in the lattice constants due to strain and hence a correspondingly smaller strain dependence to the bandwidths. The charge transfer mechanism will then play only a minor role in determining the shear moduli.

There are at least two possible explanations for the low temperature anomaly in the temperature dependence of the a axis elongational mode. The first possibility is that the anomaly is due to coupling to the b axis molecular overlap. This coupling could result from a libration of the molecules about, for example, the a axis caused by a strain along the a direction. A second possibility is that a strain in the a direction also tends to favour a change in the charge transfer between chains, perhaps by altering the electrostatic Madelung energy (Torrance and Silverman 1977). This change in charge transfer could be modelled by postulating that an a axis strain produces a rigid shift of the TTF and TCNQ bands relative to one another. As in the

b axis case the strain dependent charge transfer would disappear in the insulating phase, leading to a stiffer lattice, and a low temperature velocity anomaly.

It is instructive to consider some of the implications of the above model of the low temperature elastic anomaly. The dominant term in the expression for the electronic softening of the elastic modulus in [14] is practically identical to the expression for the Pauli spin susceptibility except that μ_B is replaced by $\beta\eta_F$ and $\beta\eta_Q$. This similarity is more general than the particular model used here suggests, and is due to the dependence of both phenomena on the density of thermally accessible states near the Fermi level. The apparent lack of an anomaly in the sound velocity near the phase transition at 38K is consistent with the corresponding spin susceptibility data (Scott et al 1974). Also the small positive curvature in the temperature dependence of the b axis elongational velocity in the range of 200K-300K (see Fig.46) is consistent with the temperature dependence of the spin susceptibility over the same temperature range.

Another feature of the charge transfer model proposed here is that it predicts a pressure dependence of the charge transfer and of the associated Fermi wavevector. If we neglect the pressure dependence of the bulk modulus, use the experimentally determined value of β and consider only the b axis strain contribution to the charge transfer, then the pressure dependence of k_F is $3 \times 10^{-3} \frac{\pi}{b} / \text{Kbar}$ corresponding to an additional charge transfer of 1%/Kbar. In this model one would also expect a change in charge transfer to result

from thermal expansion. The expected change in k_F between 0K and 300K is consistent with the temperature dependence of the $4 k_F$ anomaly observed in X-ray measurements by Kagoshima et al (1976) and Pouget et al (1976).

In conclusion, the elastic measurements show a small stiffening at temperatures below 52K for modes of vibration which are associated with a volume change. The stiffening is interpreted as arising from a strain induced charge transfer between the TTF-TCNQ conduction bands. This charge transfer softens the lattice in the metallic phase above 52 K but is inhibited in the low temperature insulating phase by the appearance of an energy gap in the electron energy bands.

(iii) Comment on Acoustic Absorption

The charge transfer model suggests an additional acoustic loss mechanism for the longitudinal modes. The idea is that it takes time for the charge transfer between chains to occur and during this time the elastic modulus relaxes from c_{22}^0 before the charge transfer can take place, to c_{22} (see [14]) after equilibrium is reached. The contribution of this relaxation process to the damping is (Zener 1948)

$$[15] \quad Q^{-1} = \frac{c_{22}^0 - c_{22}}{c_{22}^0} \frac{\omega\tau}{1 + \omega^2\tau^2} .$$

This expression is analogous to [13] in Chapter II, the expression for thermoelastic damping. The relaxation time τ is the time re-

quired for the charge transfer between chains to take place.

Intuitively one would expect the charge transfer relaxation time to be comparable with the a axis dielectric relaxation time ($4\pi\epsilon_a / \sigma_a$) where $\epsilon_a \approx 4$ (Barry and Hardy 1977) is the a axis dielectric constant and σ_a is the a axis conductivity. From d.c. conductivity measurements (Tiedje 1975) $\sigma_a \approx 3.8 (\Omega\text{-cm})^{-1}$ at 60K. The corresponding dielectric relaxation time is 1.5×10^{-11} s. At 60K we estimate from Fig. 49 that $\Delta c_{22}/c_{22}^0$ is 3%. With these numbers, and the 261 khz longitudinal resonance frequency of Sample #23 we can use [15] to calculate the absorption. We find that $Q^{-1} = 0.8 \times 10^{-6}$ at 60K whereas the observed absorption is about 10^{-4} . We conclude from this result that the contribution of the charge transfer mechanism to the damping is probably not important in the temperature regime in which the sample is metallic.

At first glance one might expect this contribution to the absorption to be independent of temperature below the metal-insulator transition because $\Delta c_{22}/c_{22}^0$ decreases exponentially as the temperature is lowered and the dielectric relaxation time increases exponentially, while the damping depends on the product. However, as discussed in the preceeding section $\Delta c_{22}/c_{22}^0$ is expected to be proportional to the spin susceptibility whereas the dielectric relaxation time will depend on the conductivity. Since the activation energy for the susceptibility (Torrance et al 1977) is lower (90K) than the activation energy (180K) for the conductivity (Eldridge 1977) one would expect the temperature dependence of the relaxation time to

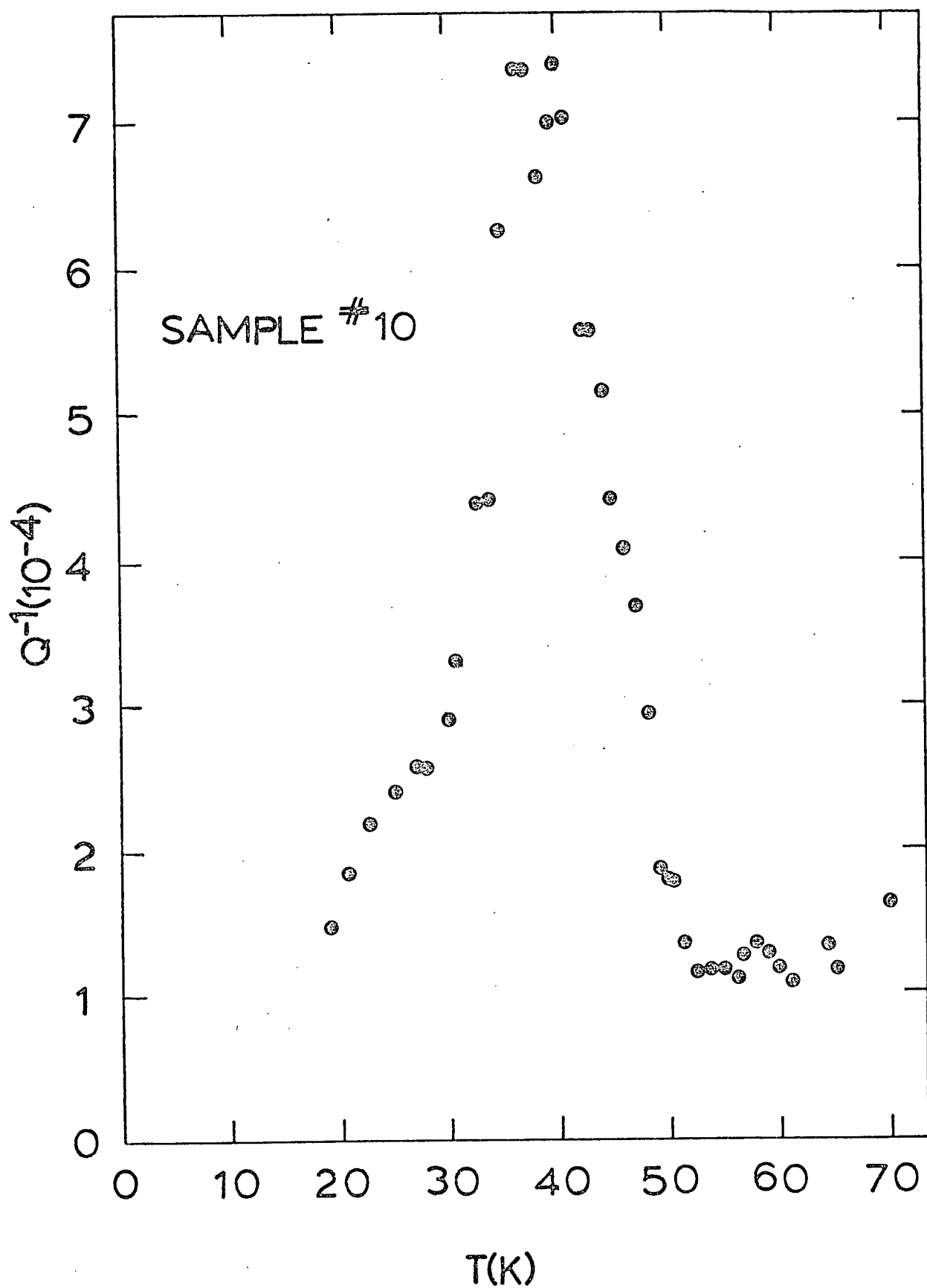


Fig. 58 - Low temperature loss peak for a longitudinal mode.

dominate and the damping to increase below the metal-insulator transition. Eventually at very low temperatures when $\omega\tau > 1$ or the temperature dependence of the conductivity becomes dominated by impurities the damping should either decrease or become temperature independent.

The temperature dependence of the damping in the insulating phase is shown in Fig. 58 for the fundamental longitudinal mode of Sample #10 at low temperatures. If we postulate that the excess low temperature absorption above the absorption minimum near 60K is due to the charge transfer contribution then we can estimate the relaxation time τ . For convenience consider a temperature of 35K where Sample #10 resonates at 384 khz. At this temperature we estimate from Fig. 49 that $\Delta c_{22}/c_{22}^0$ is 0.6% and from Fig. 58 that the additional absorption is 5×10^{-4} . With these numbers we can use [15] to calculate τ . We find $\tau = 3 \times 10^{-8}$ s. From d.c. conductivity measurements (Tiedje 1975) $\sigma_a \approx 0.03 (\Omega\text{-cm})^{-1}$ at 35K, and the corresponding dielectric relaxation time is 2×10^{-9} s. This relaxation time is an order of magnitude shorter than the time inferred from the absorption data.

However, one could argue that this dielectric relaxation time is an underestimate of the true relaxation time because the correct conductivity to use is smaller than the a axis conductivity. The reason is that the a axis conductivity arises from a series connection of an extended molecule which has little or no resistance and a high resistance (low conductivity) element which determines the charge transfer relaxation time.

Although the above argument is certainly not conclusive it cannot be ruled out as a possible explanation of the anomalous low temperature sound absorption in TTF-TCNQ.

SUMMARY

1. The Main Results of this Work

The electronic contribution to the attenuation of ultrasonic waves in one and two dimensional metals has been calculated for arbitrary $q\ell$ using a transport equation approach. The attenuation is found to be anomalously low and strongly temperature dependent in one dimensional metals. In the quantum limit, when the electron mean free path is long compared to an acoustic wavelength, the attenuation in one and two dimensional metals depends strongly on the direction of propagation of the acoustic wave. On the other hand the attenuation of sound in non-degenerate electron gases (semiconductors) is independent of the dimensionality of the electron gas. A much simpler method of solving the Boltzmann transport equation, to obtain the amplification of sound in the presence of a d.c. electric field, has been discovered.

A capacitive technique has been developed for making sound velocity and attenuation measurements on small samples. In this technique an rf carrier signal is used as a probe to detect small displacements of the sample. The rf carrier method is shown to be superior to the conventional vibration pickup which is based on applying a d.c. bias voltage to the pickup capacitor.

Three different elastic constants for TTF-TCNQ have been measured as a function of temperature. TTF-TCNQ is found to be slightly stiffer

perpendicular to the conducting direction than parallel to the conducting direction. Although the material is very anisotropic electrically, elastically it is not far from being isotropic. The strong temperature dependence of the elastic constants is attributed to the importance of molecular librations and intramolecular modes in the lattice entropy of TTF-TCNQ above 20K. The bulk modulus at zero temperature, the pressure dependence of the bulk modulus, the Grüneisen constant and the room temperature specific heat are estimated.

A small anomaly in the temperature dependence of the Young's moduli at low temperatures is interpreted as being due to the freezing out of the conduction electrons below the metal-insulator transition. The low temperature anomaly gives a direct measure of the $q \rightarrow 0$ electron-phonon coupling constant. The interpretation of the elastic anomaly suggests an explanation for the temperature dependence of the $4k_F$ spots observed by X-ray scattering. Within the resolution of the measurements, no small discontinuities in the temperature dependence of the velocities, of the type envisaged by Phillips (1977), were observed.

A method is proposed for determining the c axis thermal conductivity of TTF-TCNQ by measuring the frequency dependence of the damping of low frequency flexural vibrations.

For a summary of the experimental results on TTF-TCNQ see Table X below.

TABLE X

Summary of the Experimental Results

Modulus ¹	Room Temperature Elastic Moduli ² (10 ¹¹ dynes/cm ²)	Percent Increase From R.T. to 0K ³
E _a	3.1 ± 0.7	37
E _b	1.27 ± 0.09	58.0
c ₆₆	0.5 ± 0.1	37
Gruneisen constant ⁴		2.6
Room temperature heat capacity (C _p) ⁴		35R
Pressure derivative of bulk modulus (∂B/∂P) ⁵		16±2
Average deformation potential ⁶		0.38ev
Pressure dependence of k _F ⁷		0.5%/kbar

¹ For an explanation of these labels see Part B Section 2.2.

² These are adiabatic moduli. For the difference between the adiabatic and isothermal Young's moduli see p.148.

³ See Figs. 46 and 48.

⁴ See p.174.

⁵ See p.175

⁶ See p.186

⁷ See p.198

2. Suggestions for Further Work

In the calculation of the attenuation of sound in a one dimensional metal we have assumed a perfectly one dimensional metal, with non-zero conductivity in only one direction. However, in real materials there is always some conductivity in all directions. It would be worthwhile to check that the very small attenuation in the $q\ell \ll 1$ limit is not an artifact of the perfectly one dimensional limit that we have considered here. This calculation could be done by allowing the electronic band structure to have some three dimensional character, and then calculating the attenuation using the method of Rice and Sham (1970) for example.

Methods for measuring small displacements have received a considerable amount of attention recently in connection with the detection of gravitational radiation. From the discussion in Section 1.2 of Part B, it appears that a displacement sensitivity of $10^{-16} - 10^{-17} \sqrt{\Delta\nu}$ cm could be obtained, using the capacitive technique described in this thesis, simply by using a larger pickup capacitance and superconducting, LC resonant circuits. This sensitivity is comparable with the highest sensitivity obtained to date in current gravitational radiation detectors. More experiments are required to determine the real limits to the sensitivity of the capacitive vibration pickup.

In Section 3.2 of Part B, we have proposed two different interpretations of the low temperature anomaly in the Young's moduli. One is based on a quantum mechanical calculation of the velocity of sound in

the presence of an arbitrary deformation potential electron-phonon interaction. The other interpretation is based on an electron-phonon interaction which is peculiar to the band structure of TTF-TCNQ. If it is legitimate to extrapolate the quantum calculation to $q \rightarrow 0$, then one would expect a similar velocity anomaly more or less independent of the exact nature of the band structure, in other materials which undergo Peierls transitions. On the other hand if the second mechanism (charge transfer) really is necessary to explain the low temperature anomaly then one would only expect to see similar anomalies in materials in which there is a possibility of electron transfer from one part of the energy band to another. The ambiguity might be resolved by looking for velocity anomalies in other materials which undergo Peierls transitions, but have a different band structure, such as TaS_3 (Sambongi et al 1977). TSeF-TCNQ would also be an interesting material to look at.

More measurements should be made of the damping of longitudinal modes to determine the nature of the absorption anomalies near 52K and 150K. Also careful measurements of the damping of the low frequency flexural modes could be used to obtain the transverse thermal diffusivity.

At temperatures well below the metal insulator transition the microwave conductivity of TTF-TCNQ is known to be several orders of magnitude larger than the d.c. conductivity. A strong frequency dependence might be expected if the low temperature conductivity were dominated by localized carriers hopping between pinning sites.

A measurement of the frequency dependence of the conductivity in the range 0-1 Ghz could give some information about the hopping time. The measurement might be done with substantially the same apparatus as that used in the acoustic resonance experiments.

APPENDIX

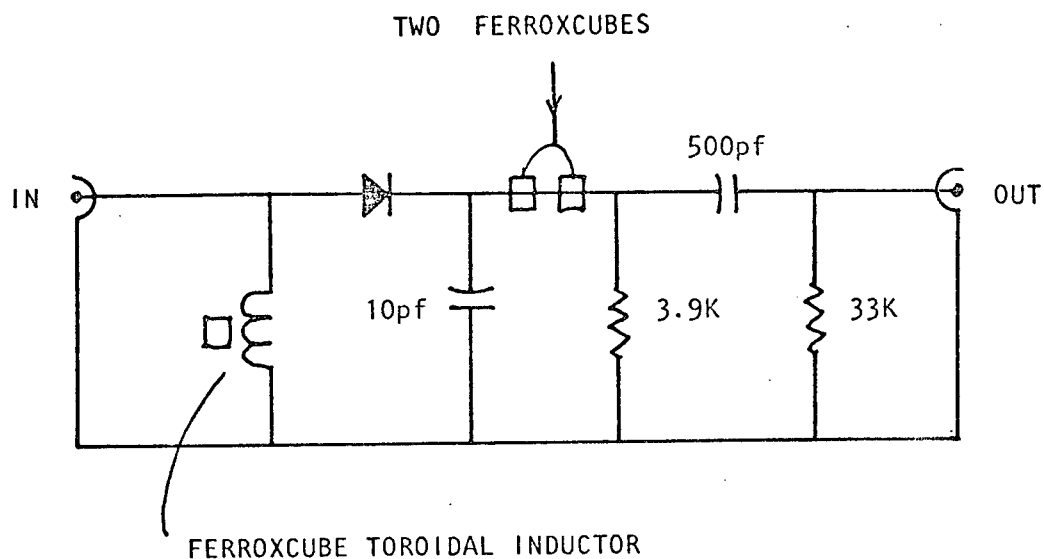
§ 1. Diode Temperature Sensor Calibration

Diode #D2755 Current 10 μ A

<u>T(K)</u>	<u>Voltage</u>	<u>T(K)</u>	<u>Voltage</u>
4.2	2.1956	60	1.0273
5	2.1581	65	1.0143
6	2.1123	70	1.0011
7	2.0688	75	.9877
8	2.0286	77	.9814
9	1.9917	80	.9742
10	1.9585	90	.9468
11	1.9290	100	.9192
12	1.9023	110	.8916
13	1.8772	120	.8639
14	1.8514	130	.8361
15	1.8226	140	.8083
16	1.7903	150	.7803
17	1.7543	160	.7522
18	1.7099	170	.7241
19	1.6516	180	.6959
20	1.5791	190	.6677
21	1.4951	200	.6393
22	1.4063	210	.6108
23	1.3228	220	.5824
24	1.2549	230	.5539
25	1.2076	240	.5259
26	1.1735	250	.4985
27	1.1496	260	.4710
28	1.1335	270	.4434
29	1.1223	280	.4155
30	1.1140	290	.3869
32	1.1022	300	.3578
34	1.0939		
36	1.0873		
38	1.0819		
40	1.0765		
45	1.0644		
50	1.0523		
55	1.0400		

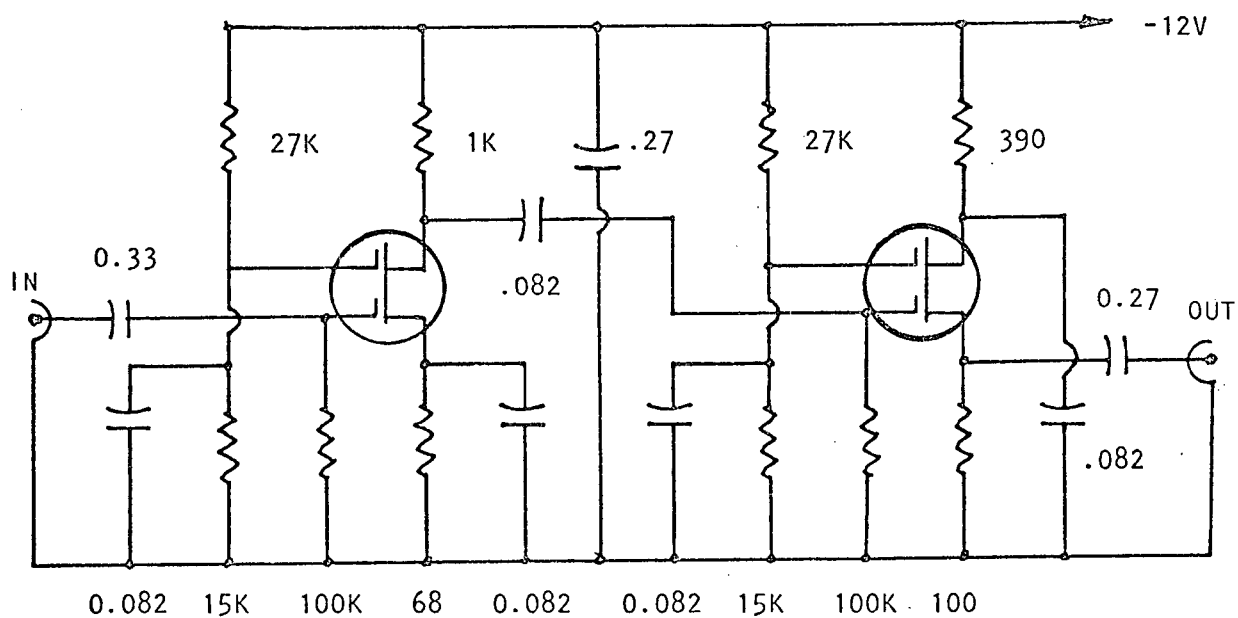
§ 2. Circuit Diagrams

(i) Diode Detector Circuit



DIODE: HP 5082-2800 Schottky Barrier Diode

(ii) MOSFET Preamplifier



(all capacitances in microfarads)

Preamplifier Specifications

MOSFET	TI 3N211
3db Bandwidth	.05-12 Mhz
Gain	20db
Output Impedance	50 Ω
Output Power	-8dbm

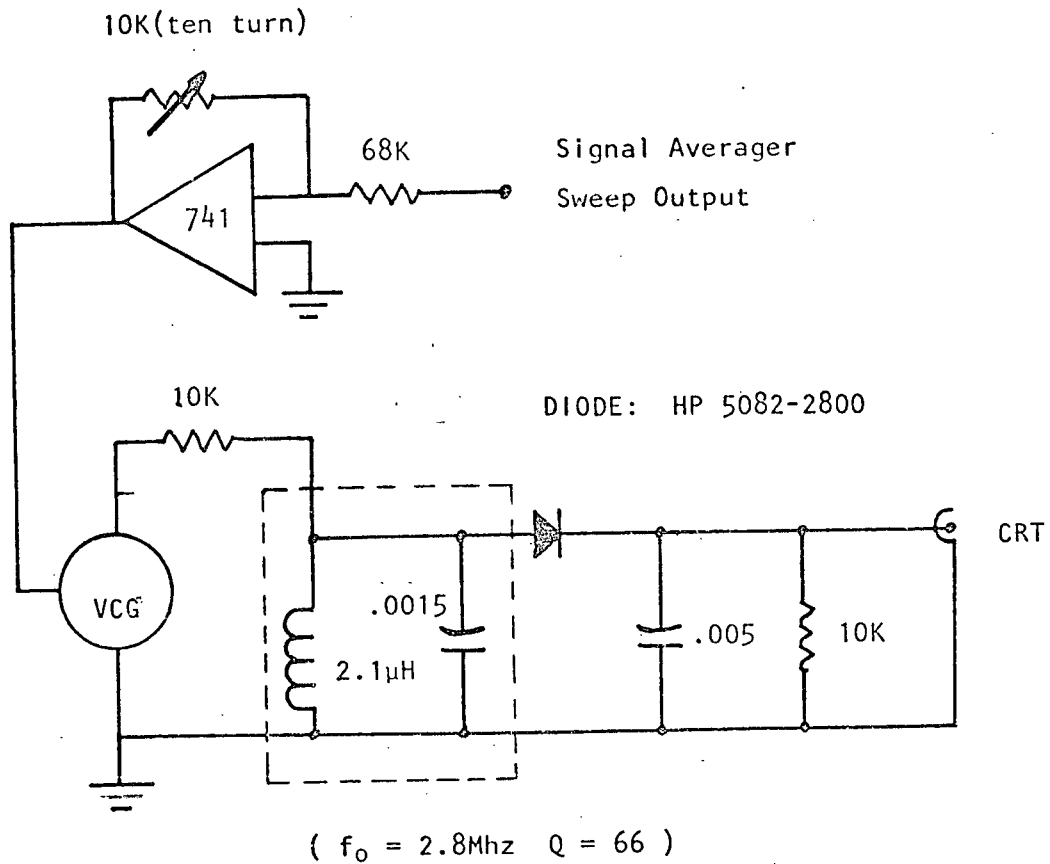
(iii) Phase Shifter (designed by S. Knotek)

Specifications

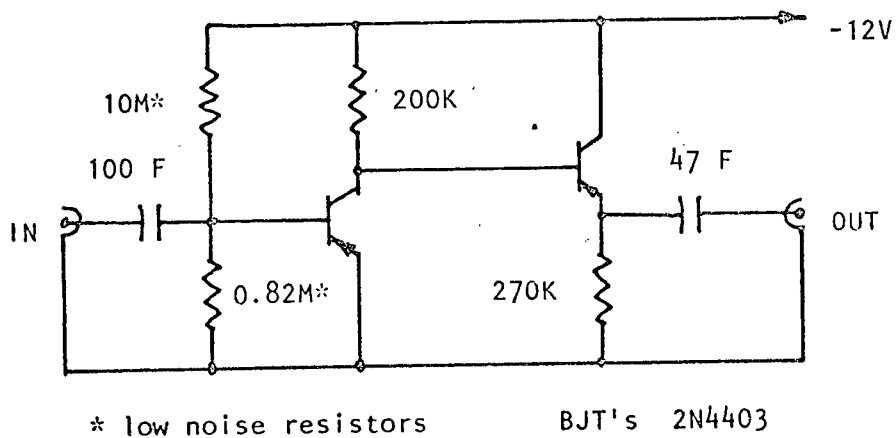
MOSFET Tetrodes	3N128
Bandwidth	.05-15 Mhz
Input	18-30dbm
Output Impedance	50 Ω
Output Power	7dbm

(Circuit diagram, next page)

(iv) Lorentzian Generator



(v) Signal Averager Input Amplifier



Gain 180

Bandwidth 0.03-50 000hz

§ 3. Thermal Expansion Correction
(Jericho et al 1977)

b axis

a and c axis expansion:

$$\alpha_a \approx \alpha_c \approx .3 \alpha_b$$

T	$\Delta l/l(\%)$
300	0
290	.10
280	.21
270	.31
260	.42
250	.52
240	.63
230	.73
220	.83
210	.93
200	1.03
190	1.13
180	1.22
170	1.32
160	1.41
150	1.51
140	1.60
130	1.70
120	1.78
110	1.87
100	1.95
90	2.02
80	2.09
70	2.16
60	2.21
50	2.25
40	2.29
30	2.31
20	2.33
10	2.34
0	2.34

BIBLIOGRAPHY

- Abraham, A. 1961. Principles of Nuclear Magnetism, Oxford University Press, London.
- Abrikosov, A.A., Gorkov, L.P. and Dzyaloshinski, I.E. 1963. Methods of Quantum Field Theory in Statistical Physics, Prentice Hall, Toronto.
- Akhiezer, A.I., Kaganov, M.I. and Liubarskii, G.Ia. 1975, Sov. Phys. JETP 5, 685.
- André, J.-J., Bieber, A. and Gautier, F. 1976. Ann. Phys. I, 145.
- Auld, B.A. 1973. Acoustic Fields and Waves in Solids, Vol. I and II, J. Wiley & Sons, Toronto.
- Barišić, S. 1972. Ann. Phys. 7, 23.
- Barmatz, M. and Chen, H.S. 1974. Phys. Rev. B9, 4073.
- Barmatz, M. Testardi, L.R., Garito, A.F. and Heeger, A.J. 1974. Solid State Commun. 15, 1299.
- Barmatz, M. Testardi, L.R. and DiSalvo, F.J. 1975. Phys. Rev. B12, 4367.
- Barry, C.P. and Hardy, W.N. 1977. Private communication.
- Behrens, E. 1968. Textile Res. J. 38, 1075.
- Berlinsky, A.J., Carolan, J.F. and Weiler, L. 1974. Solid State Commun. 14, 347.
- Bhatia, A.B. and Moore, R.A. 1960. Phys. Rev. 121, 1075.
- Bhatia, A.B. 1967. Ultrasonic Absorption, Oxford University Press, London.
- Blessing, R.H. and Coppens, P. 1974. Solid State Commun. 15, 215.
- Blount, E.I. 1959. Phys. Rev. 114, 418.
- Braginskii, V.B. and Manukin, A.B. 1977. Measurement of Weak Forces in Physics Experiments, University of Chicago Press, Chicago.

- Braginskii, V.G., Mitrofanov, Rudenko, V.N. and Khorev, A.A. 1971. Instruments and Experimental Techniques 14, 1239.
- Bulaevskii, L.N. 1975. Sov. Phys. Usp. 18, 131.
- Cantrell, J.H. and Breazeale, M.A. 1974. Proc. IEEE Ultrason. Symp. 537.
- Cantrell, J.A. and Breazeale, M.A. 1977. J. Acoust. Soc. Am. 61, 403.
- Cohen, Morrel H., Harrison, M.J. and Harrison, W.A. 1960. Phys. Rev. 117, 937.
- Cohen, M.J., Coleman, L.B., Garito, A.F. and Heeger, A.J. 1976. Phys. Rev. B13, 5111.
- Coleman, L.B., Cohen, M.J., Sandman, D.J., Yamagishi, F.G., Garito, A.F. and Heeger, A.J. 1973. Solid State Commun. 13, 943.
- Craven, R.A., Salomon, M.B., DePasquali, G. and Herman, R.M. 1974. Phys. Rev. Lett. 32, 769.
- Daniels, W.B. 1963. Lattice Dynamics, Proc. of Copenhagen Conference, ed. R.F. Wallis, Pergamon, New York.
- Debray, D., Millet, R., Jérôme, D., Barišić, S. Fabre, J.M. and Giral, L. 1977. J. Physique Lett. (to be published).
- Djurek, D., Frannlović, K., Prester, M. and Tonić, S. 1977. Phys. Rev. Lett. 38, 715.
- Doniach, S. and Sondheimer, E.H. 1974. Green's Functions for Solid State Physicists, W.A. Benjamin Inc., Reading, Mass.
- Eldridge, J.E. 1977. Solid State Commun. 21, 737.
- Fetter, A.L. and Walecka, J.D. 1971. Quantum Theory of Many Particle Systems, McGraw-Hill, New York.
- Gewurtz, S., Kiefte, H., Landheer, D., McLaren, R.A. and Stoicheff, B.P. 1972. Phys. Rev. Lett. 29, 1454.
- Girifalco, L.A. 1973. Statistical Physics of Materials, J. Wiley & Sons, Toronto.
- Gläser, W. 1974. Festkörperprobleme 14, 205.

- Goens, E. 1931. *Ann. Phys.* 11, 649.
- Hardy, W.N., Berlinsky, A.J. and Weiler, L. 1976. *Phys. Rev.* B14, 3356.
- Harrison, M.J. 1960. *Phys. Rev.* 119, 1260.
- Hartwig, W.H. 1973. *Proc. IEEE* 61, 58.
- Hearmon, R.F.S. 1961. An Introduction to Applied Anisotropic Elasticity, Oxford University Press, London.
- Henry, N.F.M. and Lonsdale, K. 1952. International Tables for X-ray Crystallography, Vol. I, Symmetry Groups, The Kynoch Press, Birmingham, England.
- Holstein, T. 1959. *Phys. Rev.* 113, 479.
- Hughes, R.C. 1975. Ph.D. Thesis, Simon Fraser University, Burnaby.
- Huntington, H.B. 1958. Solid State Physics 7, 213.
- Hutson, A.R., McFee, J.H. and White, D.L. 1961. *Phys. Rev. Lett.* 7, 237.
- Ishiguro, T., Kagoshima, S. and Anzai, H. 1977. *J. Phys. Soc. Japan* 42, 365.
- Jericho, M.H., Roger, W.A. and Simpson, A. 1977. Private communication.
- Kagoshima, S., Ishiguro, T. and Anzai, H. 1976. *J. Phys. Soc. Japan* 41, 2061.
- Keller, H.J. 1977. (ed.) Chemistry and Physics of One Dimensional Metals, NATO Advanced Study Institute Series, Vol. 25, Plenum, New York.
- Khanna, S.K., Pouget, J.P., Comès, R., Garito, A.F. and Heeger, A.J. 1977. To be published.
- Kittel, C. 1963. *Quantum Theory of Solids*, J. Wiley & Sons, Toronto.
- Kittel, C. 1971. Introduction to Solid State Physics, J. Wiley & Sons, Toronto.
- Landau, L.D. and Lifshitz, E.M. 1959. Fluid Mechanics, Addison-Wesley, Reading, Mass.

- Landau, L.D. and Lifshitz, E.M. 1969. Statistical Physics, Addison-Wesley, Reading, Mass.
- Landau, L.D. and Lifshitz, E.M. 1970. Theory of Elasticity, Addison-Wesley, Reading, Mass.
- Leissa, A.W. 1969. Vibration of Plates, National Aeronautics and Space Administration, Washington, D.C.
- Lekhnitskii, S.G. 1963. Theory of Elasticity of an Anisotropic Elastic Body, Holden-Day, San Francisco.
- Lindholm, U.S., Kana, D.D., Chu, W.-H. and Abramson, H.N. 1965. J. Ship Research 9, 11.
- Lord Jr, R.C. 1941. J. Chem. Phys. 9, 693.
- Love, A.E.H. 1944. A Treatise on the Mathematical Theory of Elasticity, 4th ed., Dover, New York.
- McGuigan, D.F., Lam, C.C., Gram, R.Q., Hoffman, A.W., Douglass, D.H. and Gutche, H. 1977. J. Low Temp. Phys. (to be published).
- Mikoshiba, N. 1959. J. Phys. Soc. Japan 14, 1091.
- Mitra, T.K. 1969. J. Phys. C, 2, 52.
- Motchenbacher, C.D. and Fitchen, F.C. 1973. Low Noise Electronic Design, J. Wiley & Sons, Toronto.
- Paul, W. and Warschauer, D.M. 1963. (ed.) Solids Under Pressure, McGraw-Hill, New York.
- Phillips, J.C. 1977. J. Phys. Soc. Japan 42, 1051.
- Pines, D. and Nozières, P. 1966. The Theory of Quantum Liquids, W.A. Benjamin Inc., Reading, Mass.
- Pippard, A.B. 1955. Phil. Mag. 46, 1104.
- Pippard, A.B. 1963. Phil. Mag. 8, 161.
- Pouget, J.P., Khanna, S.K., Denoyer, F., Comès, R., Garito, A.F. and Heeger, A.J. 1976. Phys. Rev. Lett. 37, 437.
- Rice, M.J. and Lipari, N.O. 1977. Phys. Rev. Lett. 38, 437.

- Rice, M.J. and Strässler, S. 1973. *Solid State Commun.* 13, 125.
- Rice, T.M. and Sham, L.J. 1970. *Phys. Rev.* B1, 4546.
- Salamon, M.B., Bray, J.W., DePasquali, G. Craven, R.A., Stucky, G. and Schultz, A. 1975. *Phys. Rev.* B11, 619.
- Sambongi, T., Tsutsumi, K., Shiozaki, Y., Yamamoto, M. Yamaya, K. and Abe, Y. 1977. *Solid State Commun.* 22, 729.
- Schafer, D.E., Thomas, G.A. and Wudl, F. 1975. *Phys. Rev.* B12, 5532.
- Scott, J.C. Garito, A.F. and Heeger, A.J. 1974. *Phys. Rev.* B10, 3131.
- Shapira, Y. and Lax, B. 1965. *Phys. Rev.* 138, A1191.
- Shapiro, S.M., Shirane, G., Garito, A.F. and Heeger, A.J. 1977. *Phys. Rev.* B15, 2413.
- Southwell, R.V. 1922. *Proc. Roy. Soc.* A101, 133.
- Spector, H.N. 1962. *Phys. Rev.* 127, 1084.
- Spector, H.N. 1966. *Solid State Physics* 19, 291.
- Spector, H.N. 1968. *Phys. Rev.* 165, 562.
- Tiedje, J.T. 1975. M.Sc. Thesis, University of British Columbia, Vancouver.
- Timoshenko, S. and Goodier, J.N. 1951. *Theory of Elasticity*, 2nd ed., McGraw-Hill, New York.
- Timoshenko, S., Young, D.H. and Weaver, W. 1974. *Vibration Problems in Engineering*, J. Wiley & Sons, Toronto.
- Torrance, J.B. and Silverman, B.D. 1977. *Phys. Rev.* B15, 788.
- Torrance, J.B., Tomkiewicz, Y. and Silverman, B.D. 1977. *Phys. Rev.* B15, 4738.
- Tucker, J.W. and Rampton, V.W. 1972. *Microwave Ultraonics in Solid State Physics*, Elsevier, New York.
- Vrba, J. and Haering, R.R. 1973. *Can. J. Phys.* 51, 1350.
- Waller, M.D. 1961. *Chladni Figures*, G. Bell and Sons, London.
- Weiler, L. 1977. Private communication.

- Weinreich, G. 1956. Phys. Rev. 104, 321.
- White, D.L. 1962. J. Appl. Phys. 33, 2547.
- Wilson, J.A., DiSalvo, F.J., Mahajan, S. 1975. Adv. Phys. 24, 117.
- Zener, C. 1948. Elasticity and Anelasticity of Metals, University of Chicago Press, Chicago.
- Ziman, J.M. 1972. Theory of Solids, 2nd. ed., Cambridge University Press, London.